UC Berkeley
UC Berkeley Electronic Theses and Dissertations

Title
Templated Dry Printing of Conductive Metal Nanoparticles

Permalink
https://escholarship.org/uc/item/9h91p2m1

Author
Rolfe, David Alexander

Publication Date
2015

Peer reviewed|Thesis/dissertation

eScholarship.org Powered by the California Digital Library
University of California

Templated Dry Printing of Conductive Metal Nanoparticles

by

David Alexander Rolfe

A dissertation submitted in partial satisfaction of the
requirements for the degree of
Doctor of Philosophy

in

Engineering - Mechanical Engineering

in the

Graduate Division

of the

University of California, Berkeley

Committee in charge:

Professor Albert P. Pisano, Chair
Professor Liwei Lin
Professor Amy Herr

Spring 2015

Templated Dry Printing of Conductive Metal Nanoparticles

Copyright 2015
by
David Alexander Rolfe

Abstract

Templated Dry Printing of Conductive Metal Nanoparticles

by

David Alexander Rolfe

Doctor of Philosophy in Engineering - Mechanical Engineering

University of California, Berkeley

Professor Albert P. Pisano, Chair

Printed electronics can lower the cost and increase the ubiquity of electrical components such as batteries, sensors, and telemetry systems. Unfortunately, the advance of printed electronics has been held back by the limited minimum resolution, aspect ratio, and feature fidelity of present printing techniques such as gravure, screen printing and inkjet printing. Templated dry printing offers a solution to these problems by patterning nanoparticle inks into templates before drying.

This dissertation shows advancements in two varieties of templated dry nanoprinting. The first, advective micromolding in vapor-permeable templates (AMPT) is a microfluidic approach that uses evaporation-driven mold filling to create submicron features with a 1:1 aspect ratio. We will discuss submicron surface acoustic wave (SAW) resonators made through this process, and the refinement process in the template manufacturing process necessary to make these devices. We also present modeling techniques that can be applied to future AMPT templates.

We conclude with a modified templated dry printing that improves throughput and isolated feature patterning by transferring dry-templated features with laser ablation. This method utilizes surface energy-defined templates to pattern features via doctor blade coating. Patterned and dried features can be transferred to a polymer substrate with an Nd:YAG MOPA fiber laser, and printed features can be smaller than the laser beam width.

To my family, and those who feel like family

Contents

Contents ii

List of Figures iv

List of Tables xii

1 Introduction 1
1.1 Motivation for Templated Patterning of Metal Nanoparticles 1
1.2 Prior Work 3
1.3 Previous Work on Advective Molding in Vapor-Permeable Templates (AMPT) 18
1.4 Summary of Existing Templated Patterning Methods 24
1.5 Thesis Outline and Description 26

2 AMPT Fabrication Techniques 28
2.1 Introduction to Template Fabrication 28
2.2 Master Fabrication Techniques 29
2.3 Template Fabrication Techniques 39
2.4 Ink Properties and Patterning Conditions 43

3 AMPT Flow and Modeling Techniques 48
3.1 Introduction 48
3.2 Evaporation as a Driving Force for Ink Advection 54
3.3 Modeling Approach 60
3.4 Conclusions 69

4 AMPT Devices and Experimental Work 71
4.1 Surface Acoustic Wave Resonators 71
4.2 Semiconductor Concepts 82

5 Laser-Induced Direct Ablative Rapid Transport 86
5.1 The Need for Faster Fabrication and Isolated Features 86
5.2 Selective Surface Energy Patterning Theory 87
5.3 Overview of LIDART Process 88

5.4 Template Fabrication 90
5.5 Propulsive Layer 93
5.6 Template Inking 96
5.7 Flexible Substrate Selection 98
5.8 Laser Parameters 99
5.9 Results 101

6 Conclusions and Future Work 106
6.1 Conclusions 106
6.2 Future Work 108
6.3 Multi-Layer Patterning 109

A A174 and Parylene Treatment 112

B PMP Synthesis 113

C Nitrocellulose 115

D Flow Factor Software 116
D.1 AMPT_Flow_Intro.m 116
D.2 vectors_to_matrix.m 117
D.3 color_map.m 120
D.4 compute_fill_factor.m 121
D.5 plot_fill_factor.m 129

Bibliography 130

List of Figures

1.1 Expected market for printed and flexible electronics [2]. 2
1.2 Process overview comparing the metal deposition process for lift-off, metal etching, and damascene processing, with AMPT for comparison. These printed metal processes require many more steps than AMPT and other printed processes. AMPT will be discussed in greater detail in Section 1.3. Minimum feature sizes range from 1μm for lift off, to tens of nanometers for Damascene processing. . . 4
1.3 Grain boundary showing the dimensions discussed in Equation 1.3 and the two mechanism of neck growth, j_s along the surface of the nanoparticles and $j_g b$ along the grain boundary. 7
1.4 The process of nanoparticle sintering from ink to conductive, sintered metal. First the solvent in an ink droplet is evaporated. The ligands are then vaporized, and the particles are sintered. The result is a conducting metal mesh. 9
1.5 Examples of problems with wet-printed droplets. The shape of the droplet is initially limited by the surface energy forces, then the droplet changes sizes due to the loss of solvent. Dried droplets can also experience the "coffee ring effect", when solute preferentially deposits around the edge of the droplet 11
1.6 A diagram of the gravure process. Ink wets the cylinder in the ink well. Excess ink is scraped off by a doctor blade, so that only the ink in the well can wet the substrate. The imprint cylinder keeps the substrate in contact with the ink at a high pressure (Image obtained under CC BY-SA3.0 [33]) 12
1.7 Schematic of the screen printing process. A squeegee is used to force a viscous material through holes in a screen. The squeegee brings the screen into contact with the substrate just at the point where ink is transferred through the pattern holes. 14
1.8 Schematic of the laser decal process. In the process, light comes from high-speed pulsed laser, and passes through an aperture where the image of the transferred shape is defined. It is then focused on a glass ribbon coated with nanoparticle paste. The laser sinters the particles and launches them onto a substrate. In the LIFT process, the nanoparticle past is replaced by a solid film that is liquefied by the laser. In the MAPLE-DW process, the laser ignites a small explosive film (such as triazene polymer) between the glass slide and a transfer material (such as a cell culture). 15

1.9 Schematic of different laser transfer methods. All of these methods are variations of the basic layout shown in Figure 1.8 18
1.10 A schematic of the AMPT process. A substrate (a) is flooded with solvent (b). A vapor-permeable template is placed over the solvent so that the solvent can advect through the template and bring the template into contact with the substrate. Nanoparticle ink is placed at filling ports located on the back side of the template, and evaporation drives ink into the template (c). The ink concentrates to the point at which all available template locations contain tightly packed nanoparticles (see Figure 1.10(a). At this point, the template is heated until all remaining solvent evaporates, and the template is removed, revealing dry, cohesive patterned nanoparticles (d). 20
1.11 The ink filling process of AMPT, as seen between (b) and (d) of Figure 1.10. In this plot, (a) The template is brought in contact with the substrate, which is covered in solvent (b) The template is brought into contact with the substrate, and solvent begins evaporating through the template, bringing the template in conformal contact with the substrate (c) ink is introduced to the edge of the filling channel (d) evaporating solvent brings the ink into the mold (e) the ink begins packing tightly at the end of the template (f) the ink is fully packed, and the remainder of the solvent is baked out (g) the template is removed (h) the nanoparticles are sintered 21
1.12 Schematic of the AMPT process for isolated features. In the process, (a) a template is lowered onto a substrate with clean solvent. Polymer solution is added (b), and concentrated through the AMPT process. When the template is removed (c), it leaves isolated features. A dilute nanoparticle ink is dropped over the features (d) and dried (e) so that a small film of nanoparticles is left. Tape (f) is placed on top of the polymer and is peeled off (f), pulling excess nanoparticles and polymer with it 24
1.13 A comparison of current templated patterning and laser direct-write methods discussed in this chapter. LIDART and improvements made to AMPT over the course of this dissertation work are not included. 25

2.1 Overview of the mold fabrication process, from a wafer to the PMP mold. . . . 29
2.2 Schematic of the mechanism of aspect ratio dependent etching. ARDE occurs when channels of different aspect ratios are etched by an insufficiently dense plasma. Unreacted species are rapidly depleted in long, narrow channels and cannot be replaced fast enough. The result is a set of features that etch at different heights. The effects in AMPT are catastrophic, because they prevent complete channels from forming in the template. 30
2.3 Multiple features on the same wafer, etched to different heights because of aspect ratio dependent etching. The features shown are (clockwise from the top left): 1μm interdigitated electrodes, 2μm holes in a contact pad, 5μm holes in a contact pad, and 10μm fill channel. 31

2.4 An example of a printed feature made from a template affected by ARDE. Part of the feature is not patterned because of a decreased surface area to volume ratio, while part of the pattern is filled with nanoparticles, but features that should be discrete are conjoined. 32
2.5 Examples of SiO_2 master freatures (top), showing roughness and trenching, both of which can cause a PMP template to become damaged upon removal (bottom). 33
2.6 Examples of parylene that have stuck to 1μm features during the delamination process. Parylene layers look darker than the surrounding PMP features. The contrast between IDT lines with and without paryelene is especially visible at the IDTs at bottom of the left image. Parylene adhesion to the substrate can be improved though A174 silinization and annealing 34
2.7 Examples of leakage underneath a PMP template that has been cast on a master coated in annealed parylene. The parylene roughens as it anneals, which causes solvent to leak into the template/substrate interface. Patterns were formed with dyed cellulose acetate, which is small enough to travel through asperities that are on the order of tens of nanometers in scale. Leaked dyed cellulose acetate appears a dark smudges above and to the right of the features in the left image, and along the edges of the channels in the right image. 35
2.8 The results a plasma-deposited fluoropolymer-coated master. Images (a) and (b) show high quality patterning of 1μm interdigitated fingers in the template. (c) shows a template after patterning, with nanoparticles still attached to the 1μm template features. The substrate with remaining features after the template is removed are shown in (d) and (e). 36
2.9 Process for creating two-layer masters. The process first starts with an SiO_2-coated silicon substrate. Photoresist is lithographically patterned on the substrate (a), which is then etched into the SiO_2 (b), with the silicon layer serving as an etch-stop. SU-8 is spun and lithographically aligned and patterned on top of the patterned SiO_2 features (c). Parylene or fluoropolymer may be optionally patterned on top (d). 37
2.10 Layout of a one-port resonator using a two-layer mask (left). Yellow shows features that are etched into SiO_2, while light green shows SU-8 fill channels. Dark yellow shows SiO_2 features, while light yellow shows the locations of dummy pegs. The right image shows a close-up optical photograph of the location outlined in red on the left. 38
2.11 Comparison of template material options in terms of their permeability to a range of gases and their stiffness 40
2.12 Plot showing the correlations of the logarithm of permeability to the critical volume of the solvent for different template materials. Both grades of Teflon AF decrease in permeability as the solvent critical volume increases[76]. The permeability increases solvent critical volume with PMP[77] and PDMS[78]. Data for TPX was not available. 41

2.13 The PMP casting setup, with an aluminum casting ring attached to the substrate with SU-8. A metal-reinforced PDMS layer is mounted on top of the ring and sealed with paraffin film 44
2.14 Examples of bad delamination on a PMP template showing distortion, flanging, and stiction due to swelling. 45
2.15 List of copper and silver nanoparticle inks procured for AMPT patterning. . . . 45
2.16 Comparison of ink solvents tested for the patterning of silver and copper nanoparticles. Plots show the vapor pressure with respect to temperature as described by the Antoine equation. Experimental results show that patterning occurs best in the "patterning zone," as indicated in the image. 46

3.1 Taylor-Aris diffusion, showing (a) a concentrated bolus of ink, (b) a parabolic distortion of the bolus due to the Poiseuille flow profile (c) radial diffusion due to the distortion of the ink bolus and (d) the resulting spread-out ink profile that resembles axial diffusion. 51
3.2 A comparison of the ratio of advective flux to diffusive flux for a 1% by volume ink with 40nm particles for a range of velocities. The particles are assumed to be going from fully dilute to close random packing (0.625 volume fraction [90]) in 1μm, which is the highest conceivable concentration gradient. Even in this extreme case, the rate of diffusion is no more than 0.16% the rate of advection . 52
3.3 A cross section of a channel showing (a) proper molding in which nanoparticles concentrate at the far end of a channel, and gradually pack toward the open end and (b) a blockage created by premature drying part-way through the template. Concentrated nanoparticles block the passage of any more nanoparticles, creating an incompletely patterned feature. This behavior is called "dry-out". 56
3.4 A schematic of a cross-section of a simplified PMP template with a channel in the center. Ethanol leaves the template (i) by adsorbing onto the PMP surface (ii) by diffusing through the PMP template and (iii) by desorbing from the PMP and diffusing into air 57
3.5 The measured and fit normalized mass fraction over time. Equation 3.23 is fit to the measurements to estimate the value of the diffusion constant $\mathcal{D}$ 59
3.6 A flowchart for evaluating the pattering quality of a vapor-permeable template. The chart simplifies flow modeling by first creating correlations between the template geometry and flux through the wall. Post-processing is then applied to determine the likelihood of premature drying. 61
3.7 The boundary conditions for the finite element model used in the parametric pitch studies in Figure 3.8 and Figure 3.9. The height of the template is kept constant at 200 μm, which is a common thickness for PMP templates. Since $h_m >> h_c$, the ethanol velocity in the channel scales linearly with template height. 63
3.8 Normalized flow versus channel feature density for channels with a 1:1 aspect ratio. The velocity of ethanol through the channel decreases with the increasing density of the walls 64

3.9 Average velocity through channel wall (absorption rate) plotted against the fraction of the channel wall that is a top surface 65
3.10 Zones of uniform flow rate determined by the correlations from Figure 3.8 and Figure 3.9. In this case, since the pitch of all the features is uniformly 1:1, correlations are determined by the varying aspect ratios of the template. 65
3.11 COMSOL model output showing the creeping flow velocity magnitude through the mid-plane of the model. The constant flow rates through the walls are shown in Figure (3.10 66
3.12 Control volume example shown in Equation 3.29 66
3.13 Color map of the fill factor for the sample shape shown in Figure 3.11 and Figure 3.10. The fill factor is used to determine the quality of filling. In this image, fill factors in the bottom ten percent are highlighted red. The remaining are highlighted blue. These red locations show areas of key concern, where prematurely dried nanoparticles are most likely to block flow. Four call-outs (1-4) of areas of incomplete patterning due to premature drying are compared to images of shapes printed with the AMPT process in images Figure 3.14 67
3.14 Features created using the AMPT process demonstrate problems with premature drying in the same places predicted by the fill factor template parameter. Images include (a) SEM micrograph of silver ink on silicon, optical micrograph of copper ink on lithium niobate and (c) optical micrograph of silver ink on silicon. 68
3.15 Comparison for a simplified contact pad with interdigitated fingers. Pad (a) contains square pegs that hold up the contact pad, with a large area of poor filling downstream (to the left) of the pegs. Pad (b) shows a proposed improvement to this design, evaluated using the fill factor model. The model shows better patterning on the downstream side. 69

4.1 Layout of an one-port SAW resonator. An RF signal is fed into an input set of electrodes (shown in red) that are interdigitated with a grounded electrode. The electric field in the vicinity of these electrodes causes the piezoelectric substrate below to expand and contract, creating a moving surface wave. The wave is constrained by an array of reflection gratings (shown in black) along either side of the resonator. The wavelength (λ) is proportional to the pitch (d) of the IDTs. 73
4.2 One-port SAW resonator design. This design is similar to that of the Phase 2 resonators. The resonator (light blue) uses a single GSG pad (dark blue) and requires three fill ports (green). Two of these fill ports fill the grounded reflection gratings on either side of the IDT that constraint the SAW gratings. 75
4.3 Two-port delay line design. The ladder filter uses two GSG pads, one for the input signal and one for the output signal. The design requires and requires five fill ports. The space between the IDTs determines the measured phase shift between the input and the output. 76

4.4 Three-port ladder filter. The filter contains three IDTs and requires six fill channels. Drying was particularly common in the line that connected the three IDTs. It was the most complex of the three Phase 1 designs. The electrical diagram for this filter is shown in Figure 4.5. The input voltage is read between the top left source and the common ground. The output voltage is read between the bottom left source and the common ground. 77
4.5 Schematic diagram for the circuit of the three-port SAW ladder filter. This diagram corresponds to the layout shown in Figure 4.4 77
4.6 Layout for the Phase 2 mask. Green shows SU-8 features, yellow shows resonators filled by fill channels, orange shows top-loaded resonators, aqua shows test channels with a 1:1 channel-to-gap width ratio, blue shows test channels with a 1:2 channel-to-gap width ratio, and red shows SiO_2 alignment and test features. . . 78
4.7 Images of AMPT-printed resonators ranging from 1μm 500nm. The results of these resonators are shown in Figure 4.8 and 4.9 80
4.8 Frequency response for four silver resonators printed simultaneously from a single AMPT template on a lithium niobate substrate. 81
4.9 Plot of theoretical resonance frequency (blue) and experimental frequency (green) across the range of resonator features sizes. The size of the points show the relative quality factors of each printed resonator from Figure 4.8. 82
4.10 Laser-confocal image of AMPT-patterned P3HT. The distortion from the rigid sidewalls usually seen in AMPT is a result of the toluene of the P3HT solution swelling the PDMS. 83
4.11 Current-voltage characteristics for a drop-cast diamond transistor 85

5.1 Diagram of the contact angle as a ratio as a balance of surface energies. 87
5.2 Diagram of the relative free energies for three different wetting domains. In the Cassie air trapping domain, a droplet is suspended over the surface of the template, making it impossible to pattern a feature. This can occur if the CYTOP is too hydrophobic or the feature is too small. From the Wenzel state, the Cassie impregnating state can be reached by stretching a drop with a doctor blade to break the meniscus. As shown in the energy plots, both the Cassie air trapping and the Wenzel state are metastable[135], though it is difficult to transition from Wenzel wetting to Cassie air trapping without electro-wetting or increasing atmospheric pressure. For this reason, templates must be designed to avoid the Cassie air trapping domain. 89

5.3 The LIDART patterning process. (a) A template of patterned, transparent, hydrophobic CYTOP fluoropolymer on a hydrophilic glass substrate is fabricated or cleaned. (b) Nitrocellulose solution is loaded into the template using a doctor blade. (c) The nitrocellulose solution is slowly dried, leaving a solid layer of nitrocellulose. (d) Nanoparticle ink is loaded into the template using a doctor blade. (e) The nanoparticle solution is dried, and brought into contact with a flexible substrate. (f) A low-power, continuous-wave laser is used to sinter the nanoparticle solution through the nitrocellulose without igniting the nitrocellulose. (g) A pulsed laser is used to heat the sintered metal until it ignites the nitrocellulose. (h) The template is removed, leaving sintered metal patterns on the substrate. . 90
5.4 Overview of the hot-emboss process (left) and the lift-off process (right) for CYTOP patterning. The major steps of embossing are (1a) a wafer coated with CYTOP, (1b) embossing the CYTOP under heat and pressure, (1c) removing the wafer from the press and (1d) a finished wafer with the residual CYTOP layer removed by RIE. The major lift-off steps are (2a) a wafer with a layer of SPR 220-7 photoresist spun on and (2b) developed. CYTOP is then spun on (2c) and all remaining photoresist is developed (2d). In the image, glass is shown in blue, CYTOP is shown in gray, and SPR 220-7 is shown in red. 93
5.5 Popular nitrogen-rich polymers considered for LIDART, including (clockwise from top-left) azobisisobutyronitrile (AIBN), poly[bis(azidomethyl)]oxetane (poly-BAMO), nitrocellulose, and glycidyl azide polymer (GAP). 95
5.6 The doctor blade setup. A motor is linked by a chain to drive a threaded rod. The turning rod moves a plate, which pushes a doctor blade at a steady rate. The blade sits on top of the substrate on two skids. This keeps the blade at a constant height even if the substrate is uneven. 98
5.7 Examples of LIDART templates filled with copper (bottom-left) and silver (all other images) nanoparticles. The CYTOP on these samples were hot-embossed. 99
5.8 Examples of copper nanoparticles transferred onto a glass substrate. The particles are transferred at a high speed, then smoothed with a continuous wave, pulse width modulated laser. These features were not conductive, likely because of oxidation of the particles during the heated transfer step. 101
5.9 Examples of copper nanoparticles transferred without sintering onto metal (top, viewed with a confocal microscope) and glass (bottom). If the metal particles are not sintered, they spread before hitting the substrate. 102
5.10 When the patterns become too small, features may not transfer due to (a) a nitrocellulose layer that is too small compared to the nanoparticle layer to cause delamination (b) an unevenly coated nitrocellulose or nanoparticle layer that stops the metal from delaminating on once side or (c) a nitrocellulose layer that is too large compared to the metal nanoparticle layer and rips the metal. 103
5.11 SEM images of transferred silver features on COC showing distortion due to different thermal loads. Thermal distortion can result in wrinkling (left) or tearing (right) of the metal features. 104

5.12 An SEM image of a transferred silver pattern onto COC. The edge of the pattern is thicker than the rest of the feature because of the coffee ring effect (see Figure 1.5 for more details. 105

6.1 A comparison of fabrication methods for metal features. These techniques include the previous work discussed in Chapter 1, and the addition of LIDART and AMPT as discussed in this dissertation [150][151]. 107

6.2 A comparison of the aspect ratio and layout limitations of the patterning methods from this dissertation (AMPT and LIDART) and commonly used printing techniques [46][48][152][153][154]. 108

List of Tables

1.1 Table of materials, substrates, ink solvents and pre-fill solvents used in the AMPT process. Components shown in red were used in this dissertation, all previous work comes from Demko [64] 21

3.1 A list of parameters for calculating the fluid viscosity based on temperature as determined by the Vogel equation [98] for solvents commonly used in the AMPT process 54
3.2 Comparison of ethanol (C_2H_6O) permeability with data from Pinnau[77] 60

4.1 Table of features in the Phase 2 die shown in Figure 4.6 79

5.1 Comparison of useful properties for a LIDART template materials. Lithography is the easiest and highest resolution patterning method. Plasma etching and hot embossing are two of the most complex patterning methods. 91
5.2 Comparison of commercially available nanoparticle inks for use in the LIDART process [145]. These affect the capillary number in Equation 5.9 97
5.3 A comparison of substrates tested for LIDART. The ”marking test” is a measure of the discoloration of a material after being exposed to a 60W fiber laser. The adhesion measurement is a measure of the likelihood of silver adhering to the substrate rather than the template 100
5.4 Laser parameters for sinter and transfer modes based on datasheets provided by SPI 100

Acknowledgments

A doctoral dissertation is a real community effort. There have been so many people who have offered help and inspiration to this work that it seems absurd that only my name is on the cover.

The Pisano lab has been real joy to work in. I owe my advisor, Dean Albert P. Pisano, a debt of gratitude for accepting me into the lab and making it the great place that it is. Dr. Jim Cheng served as a mentor, co-conspirator, and sounding board over three years. This dissertation would not have been possible without him or Dr. Kristen Dorsey, whose expertise, guidance, proofreading, commiseration and logistical expertise got me through the last two years. Gordon Hoople and Lila Smith were the best co-workers I could ever have. Jie Zou, Chih-Ming Lin, and Anju Toor provided critical help along the way, filling the gaps in my knowledge and qualifications. Paul Lum in the Biomolecular Nanotechnology Center, kept me entertained and well-equipped in my home away from home.

Thanks also to the wonderful friends and family that got my through the past four years. My most profound thanks goes to my parents, who raised me from an early age to value education and believe in myself. Thanks also go to my brothers. Evan kept me company over instant messenger, and Jason, having failed to convince me not to go to grad school, offered his sympathetic ear. My roommates, Evan, Tselil and Tynan, put up with my grumbling, crazy hours, and questionable cleaning contribution. The SSE provided an open platform for engineering troubleshooting. My California-based pretend-family of Mudders and others have made this place feel like home. And finally thanks to Cooper, who met me three months before quals, and has somehow stuck through to be the most incredible partner-in-crime ever since.

A special shout-out goes to the San Francisco Bay Area for being a place of endless inspiration, sun, and distractions. Also thanks to Franz Kafka for his logistic advice.

Chapter 1

Introduction

This dissertation discusses improvements to templated patterning of metal nanoparticles. Templated patterning is any method in which the shape and layout of nanoparticle features are defined by a pre-fabricated template material. The following contributions were made over the course of this research.

- Improvements were made to the evaporation-driven microfludic process that is referred to in this dissertation as AMPT
  - The process for fabricating AMPT templates was improved to create templates with uniform heights
  - A modeling approach was developed for AMPT to predict the likelihood of premature drying based on template geometry
  - A surface acoustic wave resonator was designed, fabricated, and tested using the AMPT process
- A novel method of laser-transferring surface energy patterned nanoparticle layouts, called LIDART, was developed in order to improve the throughput and lessen patterning restrictions of AMPT.

This chapter discusses the motivation for this work and existing body of research on templated metal patterning, and AMPT in particular, and concludes by describing the scope and methods of the research in this dissertation

1.1 Motivation for Templated Patterning of Metal Nanoparticles

Electronics manufacturing has gone through unfathomable transformations since the introduction of the integrated circuit in 1958[1]. Advances in lithographic processing has brought

the pitch size for processors and memory shrunk from 10 μm in 1971 to 14nm today. As effective as lithography is, it is best suited for high resolution patterning on rigid substrates.

The need for electronics outside of the sphere of traditional computing has been increasing. Traditional lithographic processing is too expensive and cannot be used to fabricate electronics on flexible substrates. New, ubiquitous sensors and transmitters require inexpensive fabrication more than small feature size.

Estimates show a rapid increase in the market for flexible electronics, reaching $1 billion by 2020, as shown in Figure 1.1[2]. Notably, this projected growth comes not only from increasing demand, but by cost reductions and performance improvements for printed electronics. As the capabilities of printed electronics increase, so will the market in applications such as flexible displays, conformable lighting, flexible photovoltaics, smart sensors and systems on foil.

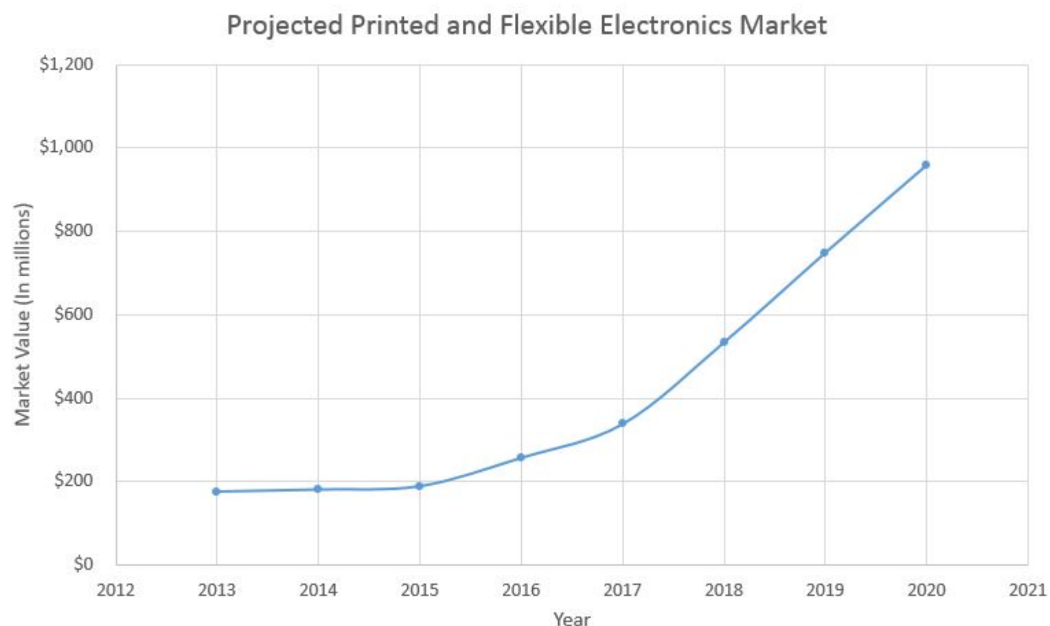

Figure 1.1: Expected market for printed and flexible electronics [2].

The current flexible and printed electronic market is especially limited by the resolution and fidelity of printed components. Depending on the process, the minimum feature size for a printed component can range from about 10 μm to over 100 μm[3]. When compared to the 15 nm pitch of modern lithographically-processed semiconductors, the present limitations of modern printed electronics become clear.

This section describes the current landscape for printed electronics, primarily focused on printed metal nanoparticles. In addition to a discussion of modern printed electronics methods, it describes previous work on the advective molding through vapor-permeable templates (AMPT) process. AMPT, and the concept of dry-templating nanoparticle patterns, is the

basis for the remainder of the work in this dissertation. This chapter concludes with an outline of the dissertation.

1.2 Prior Work

This dissertation discusses new techniques for dry-templated conductive metal nanoparticle structures. To provide more context for the need for nanoparticle printing, this section discusses the current state-of-the art of metal patterning. The techniques presented here have been chosen due to their prevalence in the industry, their applicability to the novel methods discussed in later chapters, or both.

Metal Etching, Lift-off and Damascene Processing

The majority of metal patterns fabricated for modern electronics are not printed from nanoparticles. Instead, they are deposited by either sputtering or evaporation. These processes leave a mostly conformal metal film on a surface. Patterning these films requires additional steps to define the desired metal pattern, and remove the unwanted parts. Three processes will be discussed in this section: lift-off, metal etching and damascene processing.

Lift-off and metal etching are especially relevant as the current methods for making surface acoustic wave (SAW) resonators as is discussed in Section 4.1.

Photolithography

Photolithography is the basis for all traditional microfabrication, including metal etching, lift-off, and damascene processing. In these three metal deposition processes, the desired pattern must be photolithographically defined on each substrate.

In photolithography, ultraviolet light is used to develop a photopolymer. The photopolymer is a light-sensitive polymer that is spin-coated on a substrate. In the case of a positive photoresist, exposure to ultraviolet light degrades the polymer, making it possible to wash away the exposed resist with a solvent, known as a developer. In the case of a negative resist, light cross-links the photopolymer, making it insoluble in developer.

In photolithography, UV light is blocked in select places by means of a mask, usually a chrome pattern on a glass or quartz plate (shown in black in 1.2). The mask is either held in contact with the photoresist surface, or slightly above it. For an optical lithography system, the resolution of the pattern, R, can be calculated as[4]

$$R = k_1 \frac{\lambda}{NA} = k_1 \frac{\lambda}{n \sin \alpha} \tag{1.1}$$

where λ is the wavelength of the light source and NA is the numerical aperture, which is a measure of the concentration of the light. In contact lithography, where the photomask is placed directly over the photopolymer, the numerical aperture is 1, n is the refractive index of the medium, and α is the angle that the light takes from the concentrating lens to the

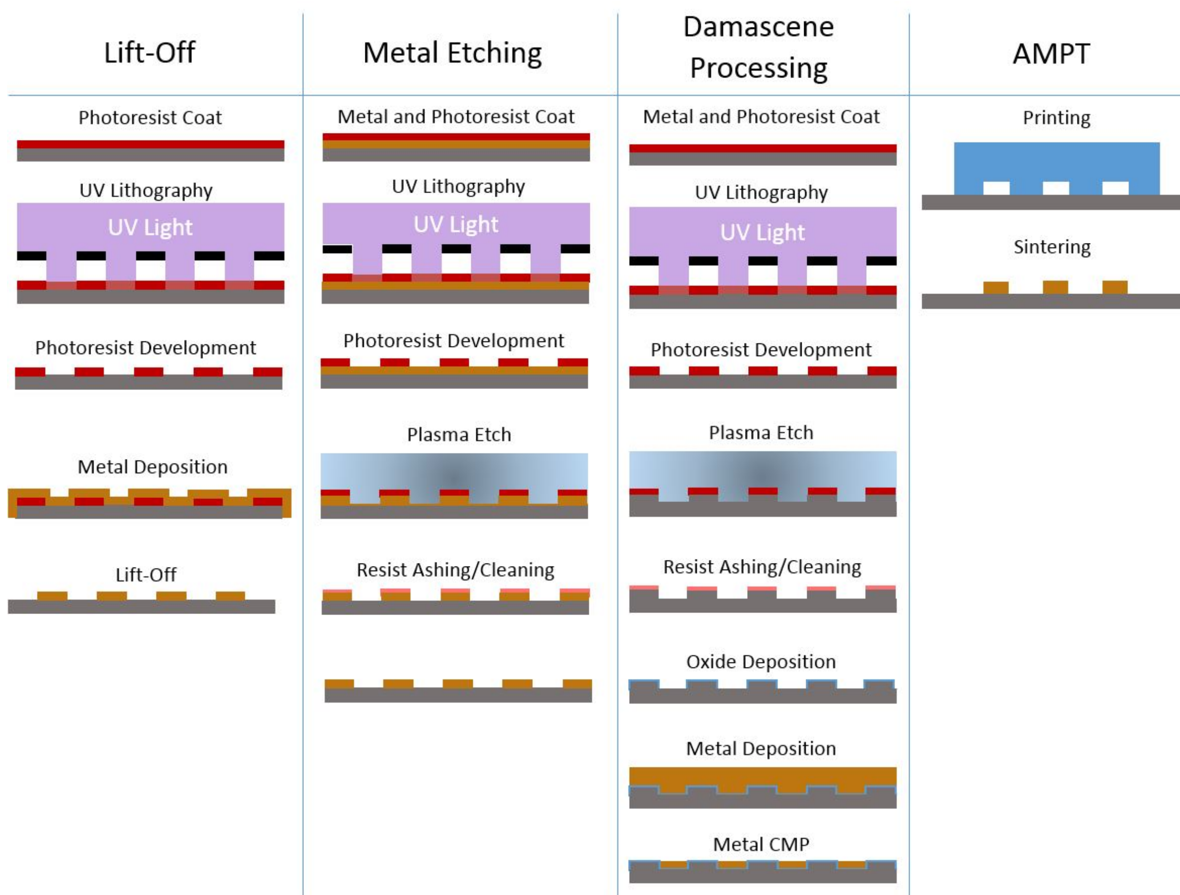

Figure 1.2: Process overview comparing the metal deposition process for lift-off, metal etching, and damascene processing, with AMPT for comparison. These printed metal processes require many more steps than AMPT and other printed processes. AMPT will be discussed in greater detail in Section 1.3. Minimum feature sizes range from 1μm for lift off, to tens of nanometers for Damascene processing.

wafer. The constant, k_1 is usually 0.61, but can depend on the ability of the resist chemistry, topology and reflectivity of the wafer below the resist.

While photolithography is especially important for metal etching, lift off and damascene processing, it is relevant to many components of this dissertation. It is the primary method for producing the templates for both the AMPT and LIDART processes. Central to both of these processes is that while a template must be defined by lithography, the template may be used to make new patterns many times.

The ability to use a template many times also means that template may be created by more time-intensive but higher-resolution means such as electron-beam lithography and/or nanoimprint lithography.

Metal Etching

Metal etching was the standard procedure for creating patterned horizontal metal interconnects in early computer fabrication. Metal etching is an appropriate approach for any situation in which the metal can be etched without the concern of damage to the layer below and without chemically damaging the metal itself with the enchant.

Wet etching technology is especially well suited to aluminum. Wet etched aluminum features can be as small as 3 μm in size and 8 μm pitch [5]. Beyond this point, process control becomes extremely difficult. Wet etch processes are often limited by their inherent isotropy, and etch bias can often play a role in lowering the fidelity of the patterned metal shape. Plasma etching allows for much better resolution, but can damage surface chemistry [4]. Aluminum can be etched in a fluorine plasma, but Cl_2 etches aluminum isotropically. Inhibitor gases such as $CHCl_3$, $CFCl_3$ and CCl_4 can be used to increase anisotropy.

Copper is much more difficult to etch than aluminum. It is less reactive in wet etches and it does not create volatile byproducts when plasma etched. As the industry migrated from aluminum interconnects to copper, it abandoned chemical metal etching, and switched to damascene processing.

It is difficult to discuss an overall minimum feature size for metal etching. In reactive ion etching with an inductively coupled plasma, it is possible to create features with critical dimensions on the order of tens of nanometers [6], but this varies by metal and the permissive level of contamination[4].

Lift-off

Lift-off is a simple alternative to metal etching that can create reproducible, high-fidelity structures without the risk of etch bias or chemical contamination [5]. A lift-off processed metal pattern is created by patterning one or more layers of photoresist in the negative image of the desired metal features. After the photoresist has been deposited and lithographically patterned, metal is deposited by evaporation. The photoresist is then swollen or dissolved, removing any metal deposited on the photoresist. The directionality of the evaporation keeps the metal deposited on the substrate from making contact with the metal on the resist. The high quality and repeatability of lift-off has made it a desirable process for creating reproducible SAW resonators [7].

As the resolution of lift-off shrinks, several problems arise. The largest is retention, which is when unwanted metal is not completely removed. This occurs when the resist is not fully dissolved, or when too much metal bridges between the features and sacrificial area. Another problem is "ears", which are made of excess metal sidewall sticking above the feature. The practical limit for lift-off resolution is 1 μm, below which, it becomes increasingly expensive to pattern high-aspect ratio photoresist [8]. This limit is the basis of the investigation into printed SAW resonators in 4.1.

Damascene Processing

The semiconductor industry shifted from aluminum to copper, primarily for the higher inherent conductivity of copper. However, because copper is difficult to etch, a new process had to be developed to pattern it [9]. In Damascene processing (named after a similar technique for making gold-inlayed jewelry), a trench is first etched into a substrate. Then, a thin, conformal layer of SiO_2 is deposited to protect silicon from copper diffusion. A thick layer of copper or other metal is deposited over this surface, filling in trenches completely and coating the top of the wafer. Excess copper is then removed by means of chemical-mechanical polishing (CMP), so that what remains are copper traces, encased in SiO_2, sunken into trenches in the substrate. The process is extremely high resolution, because it takes advantage of anisotropic etching of ceramics. However, the process is more complex than lift-off and metal etching.

Metal Feature Construction Through Nanoparticle Deposition and Sintering

The previously discussed methods of metal deposition by means of vacuum processes like evaporation and sputtering which generate uniform thin films by depositing metal atoms at a substrate surface [4].

Evaporation and sputtering have exemplary film uniformity, but they are expensive processes, requiring time and expensive vacuum equipment. Furthermore, they waste metal by coating the entire wafer and parts of the chamber in metal. In comparison, printed metal nanoparticles can be deposited on only the areas of interest in an ambient atmosphere.

The major difficulty of metal printing is the transition from a liquid phase (for printing) to a conductive solid sintered phase. Metal printing research in the 1980s and 1990s initially focused on the printing of molten metals, but success was limited by the accelerated oxidation of metal at high temperatures [10], and the difficulty of adhering molten metal structures on substrates [11]. The difficulty of handling molten metal also increased the difficulty of patterning. Other work in the field included printing metallo-organic inks that could be decomposed into conductive metals [12] and solid metal powders that could later be sintered [13]. These printing methods were eventually superseded by nanoparticle ink printing [14].

Nanoparticles are particles with a critical dimension in the nanometer range (definitions vary between 100 nm and 1 μm). Nanoparticles have many useful properties for printed electronics. They are small enough to be passed trough microfludic channels and nozzles, and can be formed into high-resolution micro- or nano-scale features. Many types of nanoparticles are also relatively inexpensive to produce and suspend in solvents.

At the nano-scale, a large portion of the atoms in the particle are located on the surface. The energy associated with these surface-facing atoms is higher than the energy of an atom embedded within the bulk lattice of a material. Nanoparticles have a tendency to melt or sinter at lower temperatures than their respective bulk materials because the bulk state is energetically favorable. The melting tendency of nanoparticles can be described by the Gibbs-Thomson equation, and is given as

$$T_m = T_{m,\infty}\left[1 - \frac{2(\gamma_s - \gamma_l)}{\rho r_p \Delta H_{m,\infty}}\right] \tag{1.2}$$

where T_m is the melting temperature of the nanoparticles, $T_{m,\infty}$ is the melting temperature of the bulk material, γ_s and γ_l are the surface energies of the solid and liquid phases of the metal, respectively, ρ is the metal density, r_p is the particle radius, and $\Delta H_{m,\infty}$ is the enthalpy of bulk phase transition [15]. From a practical perspective, the melting point depression from the Gibbs-Thomson equation becomes relatively insignificant for particles larger than 10 nm. However, the increased surface energy-to-volume ratio of nanoparticles can still be used to create conductive traces through the process of sintering.

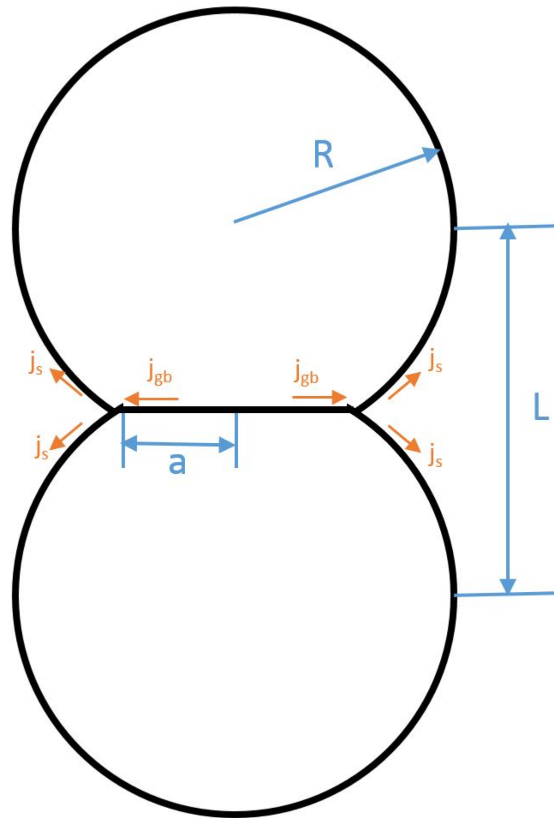

Figure 1.3: Grain boundary showing the dimensions discussed in Equation 1.3 and the two mechanism of neck growth, j_s along the surface of the nanoparticles and j_gb along the grain boundary.

Sintering is a process by which a solid object is made from small particles held at elevated temperatures or pressures. The particles become interconnected, creating a porous, but interconnected structure. Because of their structure, and impurities inadvertantly introduced during the sintering process, sintered components generally have lower strength, conductivity and density than their bulk counterparts.

Sintering is a gradual process that occurs below the melting point. Both gold and silver can be readily sintered below 300°C [16]. Sintering is a process of material migration, as the divide between two metal spheres is bridged by diffusing metal. The sintering of two particles is shown in Figure 1.3. The flux during diffusion can be represented by the equation

$$j = \frac{2D}{\ell\Omega} sinh\bigg(- \frac{\ell}{2kT}\nabla\mu \bigg) \tag{1.3}$$

where D is the diffusion coefficient, ℓ and Ω are the atomic spacing and volume, respectively, k is the Boltzmann constant, and T is the temperature in Kelvin. The chemical potentials, μ are different for the two different grain boundaries [17]. The chemical potential for the grain boundary j_{gb} is

$$\mu_{gb} = -\Omega\sigma \tag{1.4}$$

where σ is the stress normal to the grain boundary. The surface chemical potential is

$$\mu_s = -\Omega\gamma_s\kappa \tag{1.5}$$

where γ_s is the specific surface energy, and κ is the free surface (particle). After some simplification, the driving force of diffusion at the edge of the grain boundary is:

$$F = \nabla\mu \approx 2\gamma_s(4 - a/R)\frac{\Omega}{(a/R)^3}\frac{1}{R^2} \tag{1.6}$$

Where a/R is the normalized half neck size. It is notable from Equation 1.6 that the driving force F increases by the square of the decreasing particle radius. This is what leads to the huge driving force for sintering nanoparticles.

In the context of nanoparticles, “sintering” referrs to both the sintering of the metal particles and the prerequisite removal of any ligand layer that surrounds the nanoparticles. In the case of easily-oxidised metals, such as copper, the ligand layer protects the nanoparticle from oxidation. Depending on the method of nanoparticle synthesis, the ligand can serve as the “cap” that cuts off nanoparticle growth. Ligands also protect the nanoparticles from getting close enough to agglomerate.

While ligands are important for a nanoparticle suspension, they prohibit nanoparticles from sintering. Thus, the sintering process for a nanoparticle ink consists of three separate steps: solvent evaporation, ligand vaporization, and particle sintering. The process is shown in Figure 1.4. In the case of silver nanoparticles, both ligand removal and nanoparticle sintering have logarithmic correlation between the inverse sintering temperature and sintering time [18].

Since most ligands are organic, they insulate the nanoparticles electrically. Dried nanoparticle inks with thick ligand layers are insulating, while nanoparticles with smaller ligand layers can be weakly conductive.

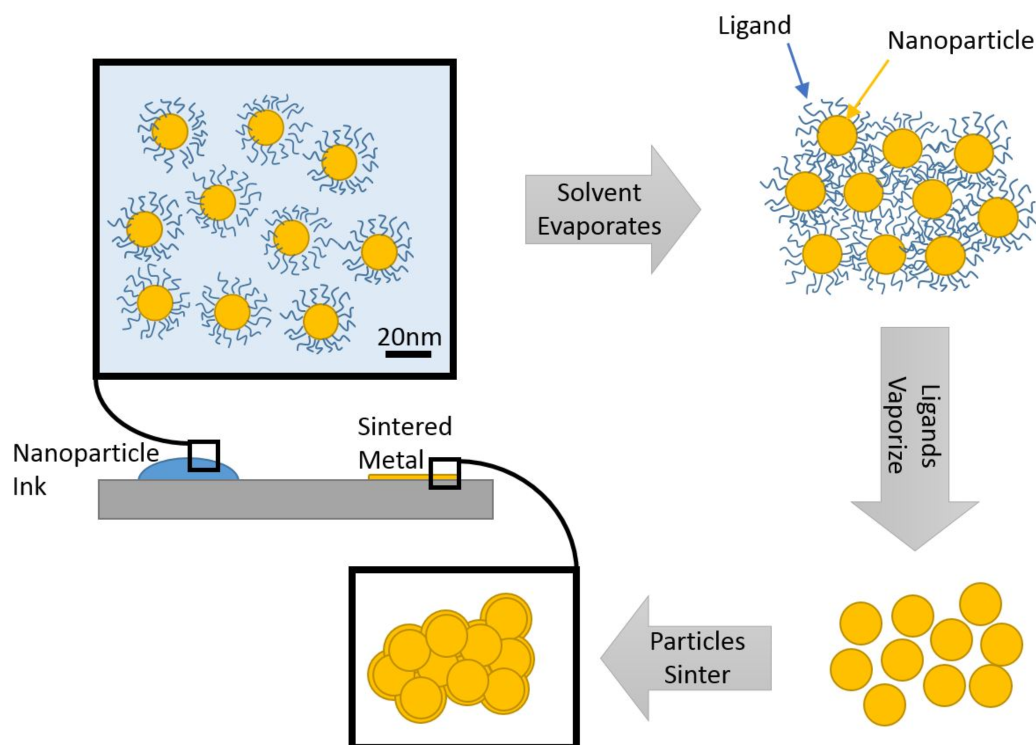

Figure 1.4: The process of nanoparticle sintering from ink to conductive, sintered metal. First the solvent in an ink droplet is evaporated. The ligands are then vaporized, and the particles are sintered. The result is a conducting metal mesh.

Silver Nanoparticle Printing

Silver is much less expensive than gold, and it has an oxidation rate much lower than that of aluminum, iron or copper[19][20]. These qualities make it a good choice for nanoparticle patterning. Silver was one of the first nanoparticles to be printed [14], and is now used to print flexible devices such as RFID tags on an industrial scale [21].

Silver can be sintered at temperature between 200°C and 300°C, with sintering times lasting from several hours to tens of minutes, respectively [18]. The speed of sintering increases as nanoparticle size decreases. However, successful sintering has been demonstrated through a variety of other approaches including electrical sintering, microwave sintering, plasma sintering, and photonic sintering through flash bulbs [22] and lasers [23].

Silver nanoparticle ink is widely available commercially. Because the oxidation risk is low, silver can be produced with a variety of ligands. Citrate ligands are most common, but thiol and acids such as humic acid [24] and myrystic acid are sometimes used [18]. All experimental work in this dissertation was conducted using DGP AP ink from Advanced Nano Products Co. LTD, (Buyong-myeon, South Korea). This ink contains nanoparticles averaging 20 nm at about 40 wt% in ethanol. The ligand for these nanoparticles is proprietary, but small

enough that bulk conductivity of unsintered particles is about an order of magnitude below that of sintered particles.

Copper Nanoparticle Printing

Silver is versatile and resists oxidation, but the lower cost of copper makes it an exciting option for large-scale metal construction. Evaporated copper interconnects were first introduced by Skyworks in 2009 [25]. Copper costs less than 1% as much as silver, but is 95% as conductive. If electronics are to be printed on a large scale, they will need to be made with copper rather than silver. Still, copper oxidises at a much faster rate than silver, too fast for unprotected nanoparticles to be exposed to atmospheric levels of oxygen.

Copper nanoparticles are relatively easy to produce via a variety of methods, including sonochemical reduction, microemulsion techniques, thermal reduction, radiation methods, polyol process, reducing flame synthesis, metal vapor synthesis, vacuum vapor deposition, and chemical reduction in solution [26].

The oxidation of copper has been a major hindrance to the development of copper nanoparticle inks. In recent years, oxidation-resistant inks have been brought to market. Copper can resist oxidation if the nanoparticle surfaces are protected from contact with oxygen by a barrier. There are two different types of barriers: conductive protective shells that become alloyed or suspended in the nanoparticles after sintering, and insulating shells that must be vaporized before the copper can become conductive.

Noble metal shells are designed to protect the copper from oxidation while remaining conductive themselves. Since they are mostly made out of copper, these nanoparticles can theoretically cost less than comparable particles made out of exclusively precious metals. Bimetalic shells produced by the successive reduction of one metal over another are common, and include Au-Pd, Au-Pt, Ag-Pd, Ag-Pt, Ag-Cu and Ag-Au [27]. Silver-shell copper-core nanoparticles, a more recent innovation, are now gaining popularity for their low cost and limited oxide growth [28]. Conductive shells have also been made of non-metals, such as graphene and silica [26].

Insulating shells are usually produced from polymer ligands or surfactants. Common small-molecule surfactants, such thiols and lauric and oleic acids improve oxidation resistance somewhat[26]. However, polymer capping agents have been more successful. Most notable of these is poly(N-vinylpyrrolidone) (PVP). Copper sintered from these particles is less conductive than pure copper, owing to the growth of a small CuO layer on the surface [29], though it is possible to reduce this oxide buildup in hydrogen [30].

The work in this dissertation used copper nanoparticles with insulating shells purchased from Intrinsiq Materials (Hampshire, UK). These particles have a proprietary coating designed for up to 6 months of shelf life, and an average resistivity of 2-3x bulk copper. Though the exact coating is not known, it is volatile enough that can be vaporized with a laser, as will be discussed in Chapter 5.

Ink-Based and Wet Printing Methods

Most modern printing methods are wet printing methods. In these methods, ink is deposited onto a substrate while it still contains liquid solvent. Liquid inks can be easily forced into a template shape with shear force and brought into conformal contact with the substrate. This generates the van der Walls force (a bond based on surface energy) and/or mechanical adhesion (the filling of voids and pores across an interface) that keeps an ink onto the substrate.

Wet printing can either be direct-write or templated. In a direct-write process, such as inkjet or fused deposition, ink is positioned by a print head [31]. These processes are good for low-throughput applications, since they do not require any initial tooling costs to make new patterns. In a direct-write process, ink in the form of a filament or droplet, is deposited onto desired locations on the substrate.

Templated printing processes rely on a template rather than a print head to position the ink on a substrate. This section will discuss two leading templated printing methods. The first is gravure, in which ink is first loaded into wells, then transferred to a substrate. The second process is screen printing, in which ink is forced through a patterned screen, directly on a substrate. Together, these processes comprise most of the modern templated printing market [3].

Each wet printing process has its own advantages and disadvantages, but there are several common problems among all types of wet printing. Issues related to volume changes are most significant. As an ink droplet evaporates, it loses its solvent volume. This makes it difficult to create features of a precise height. Drying also hurts the uniformity printed structure profiles through the "coffee ring effect" [32], in which the evaporating along the edge of a droplet pulls nanoparticles and solutes to the droplet's edge. This phenomenon can be observed by drying a drop of coffee on a table. The coffee solids gather in a ring around the edge of the drop, rather than in a solid disc.

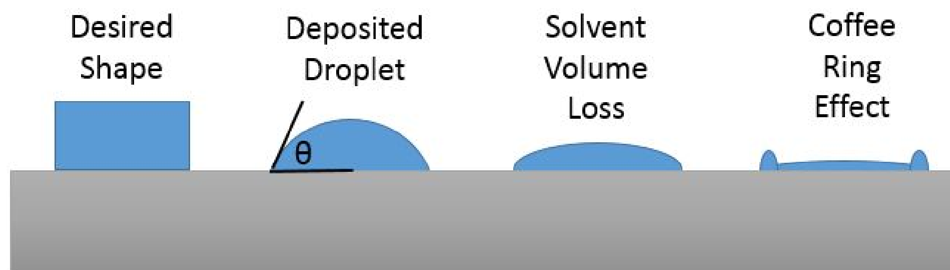

Figure 1.5: Examples of problems with wet-printed droplets. The shape of the droplet is initially limited by the surface energy forces, then the droplet changes sizes due to the loss of solvent. Dried droplets can also experience the "coffee ring effect", when solute preferentially deposits around the edge of the droplet

Ink droplets are also subject to interfacial forces. The shape of a drop (at sufficiently low

viscosity) is determined by the balance of forces along the interface of the drop. This is what leads to a droplet's hemispheric profile. Interfacial forces also cause droplets to wet different surfaces to different extents, so each ink in a wet process must be carefully formulated to match its substrate. The contact angle of a drop on a flat surface (Figure 1.5, second from the left) is shown in Equation 1.7

$$cos\theta = \frac{\gamma_{SA} - \gamma_{SL}}{\gamma_{LA}} \tag{1.7}$$

where γ_{SA}, γ_{SL}, and γ_{LA} are the surface tensions of the solid/air, solid/liquid and liquid/air interfaces, respectively.

Gravure

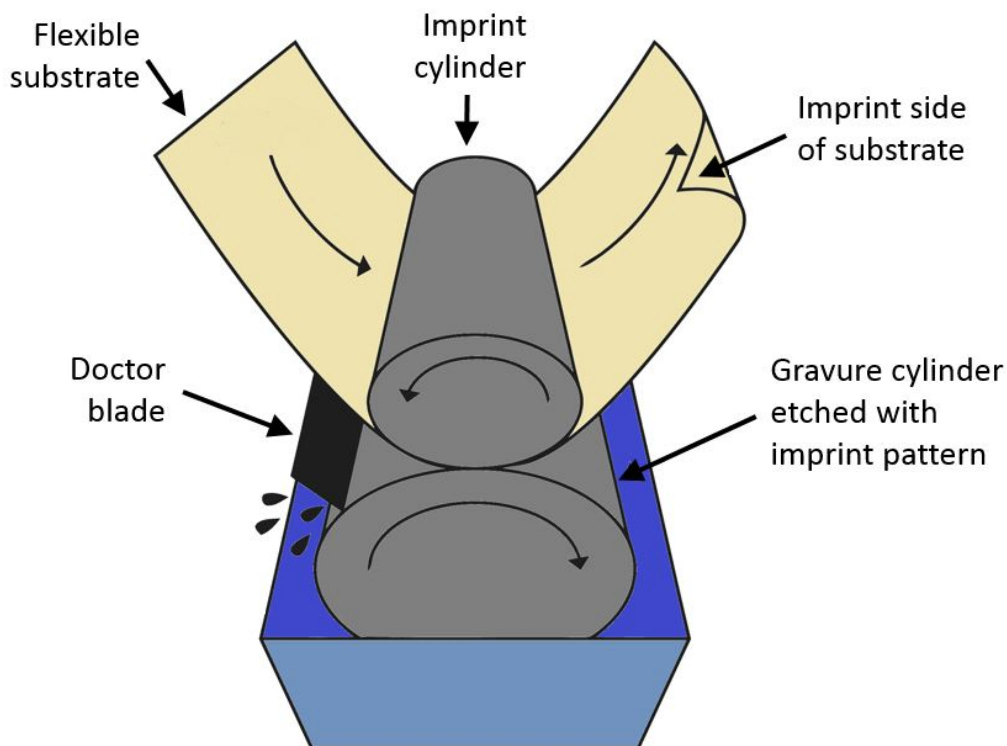

Figure 1.6: A diagram of the gravure process. Ink wets the cylinder in the ink well. Excess ink is scraped off by a doctor blade, so that only the ink in the well can wet the substrate. The imprint cylinder keeps the substrate in contact with the ink at a high pressure (Image obtained under CC BY-SA3.0 [33])

Gravure is a process that has long been used for the printing of text for newspaper . It has since been transferred to electronic printing applications including organic semiconductors

[34] and nanoparticles[35]. In the gravure process, ink flows into wells etched into a large cylinder. Gravure drums traditionally contain a set of discrete wells of uniform dimensions separated from each other by a small distance. This lets a gravure process print features of varying sizes. A similar process, called "intaglio" uses a drum with continuous trenches of varying sizes[36]. Once the ink is loaded into wells, excess ink is scraped off the surface by a doctor blade. The ink is then transferred to the substrate at high pressure, where it preferentially wets and re-flows onto the substrate. Some gravure processes, contain an intermediate offset roller, where the ink is first deposited before it is transferred onto the substrate. Once transferred, the ink reflows from isolated features defined by the gravure well to a continuous shape. The solvent in the ink then evaporates, leaving a dry pattern on the substrate. This process is shown in Figure 1.6.

The strong-point of gravure printing is its speed. Initially designed for high-throughput printing, gravure can make functional parts such as electrical leads at speeds up to 1000 m^2/min [37]. This has made gravure extremely attractive for low cost, high volume electronic manufacturing.

There are a number of limitations associated with gravure. The first is the initial tooling cost. Gravure systems require an assembly of highly complex parts that operate at high speeds and pressures. The drum in particular, where the pattern is etched, must be extremely smooth and round. Etching features into a cylinder is significantly more complex, since lithography may only be done on flat surfaces. For this reason, gravure is only appropriate for high-throughput processes. A larger limitation of gravure is related to the ink dynamics. In order for a gravure process to be successful, the ink must have all of the following properties [38]:

1. The ink must fill completely into every well or trench with an equal amount of ink. Variability in inking creates a variability in feature size.

2. Excess ink must be completely removed from the surface of the drum. Any remaining ink will cause unwanted features.

3. The ink must de-wet the drum and wet the substrate completely.

4. The ink must reflow sufficiently to create continuous features from the isolated gravure wells.

Screen Printing

Screen printing is a process by which viscous ink is templated directly on the substrate. It can be used for rigid or flexible substrates. The technique of screen printing is used in graphic arts and fabric printing applications, usually for small batches.

The screen in screen printing is a mesh with holes larger than the ink particle size with areas on the screen selectively rendered impermeable. The screen is suspended above the substrate, and a squeegee is used to force the ink over the screen, and through the mesh

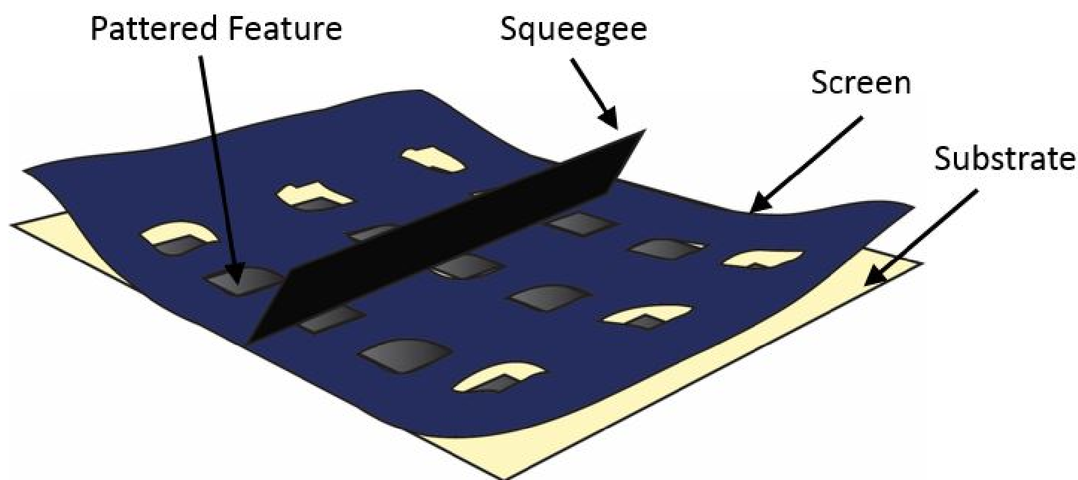

Figure 1.7: Schematic of the screen printing process. A squeegee is used to force a viscous material through holes in a screen. The squeegee brings the screen into contact with the substrate just at the point where ink is transferred through the pattern holes.

features. The downward force exerted by the squeegee presses the screen in contact with the substrate only at the point of patterning. This prevents damage to the pattern by the squirm of the screen at any other point.

This process of bringing the screen in contact only below the squeegee makes alignment of the screen pattern to other layers extremely difficult, though the process is improving and now multi-layer printing is possible. Multi-layer screen printing is now used in solar cells [39].

Screen printing ink is generally significantly thicker than inkjet or other inviscid nanoparticle inks. A nanoparticle screen printing paste is roughly 70% nanoparticles by volume. The viscosity of a nanoparticle ink must be so viscous so that it can keep its shape after the screen is lifted from a given location. Since the nanoparticle ink is not constrained by the screen template after the screen is lifted from a given location, reflow can be severely limiting to the resolution of the pattern [40].

In a lab setting it is possible to make 10 μm lines spaced 10 μm apart. However, on an industrial scale, the resolution is limited to about 50 μm [37]. When an ink is forced through a screen, it remains the same thickness as the screen mask. This limit to the aspect ratio makes it exclusively a thick-film process [41].

Laser-Transfer Methods

Laser-transfer patterning can be either a direct-write or templated method of transferring solidified or highly-viscous material from a ribbon to a substrate. Current processes do not pre-pattern the material in a template. A novel process of laser transferring template-patterned nanoparticles, called LIDART, is discussed in Chapter 5.

Laser-transfer methods go by many names, each with slight variations in laser, patterning medium, or transport mechanisms. In most laser transfer processes (shown in Figure 1.8), a very short-pulse laser is fired through an aperture, and focused by an objective lens on a glass ribbon coated with a solid film or nanoparticle coating. The coating is heated by the laser, and launches off the ribbon onto a substrate, where it adheres and cools. There are many variations to this process.

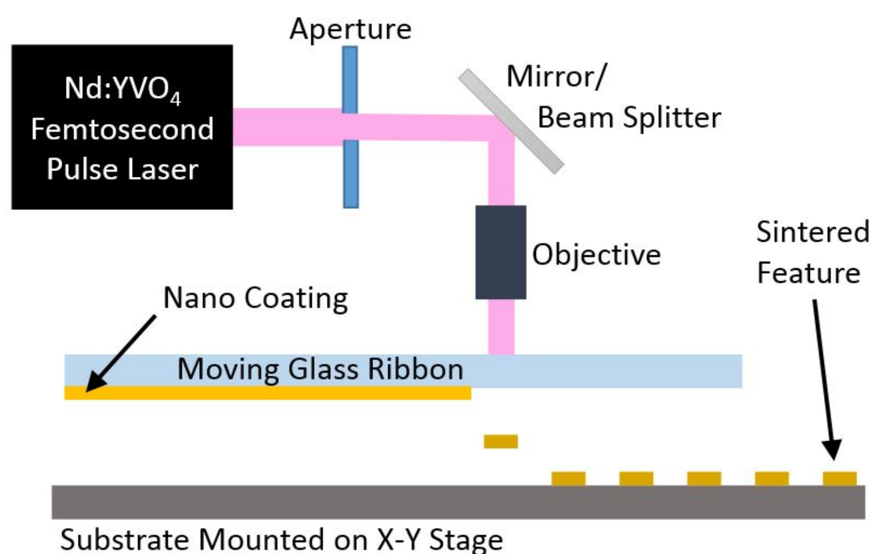

Figure 1.8: Schematic of the laser decal process. In the process, light comes from high-speed pulsed laser, and passes through an aperture where the image of the transferred shape is defined. It is then focused on a glass ribbon coated with nanoparticle paste. The laser sinters the particles and launches them onto a substrate. In the LIFT process, the nanoparticle past is replaced by a solid film that is liquefied by the laser. In the MAPLE-DW process, the laser ignites a small explosive film (such as triazene polymer) between the glass slide and a transfer material (such as a cell culture).

- **Laser Induced Forward Transport (LIFT)** The LIFT process uses a femtosecond laser to liquefy a metal film and launch it onto a substrate. Metal films including Cu, Ag, Al, W, Cr [42], Au, and Zn [43]; oxides such as Al_2O_3 and In_2O_3 [42]; and indium tin oxide [44] have been patterned.

In the process, a laser pulse first heats the metal film at the interface between the glass ribbon and metal film. The melt front (the part of the metal in its liquid phase) propagates to the free surface of the film. By time the free surface melts, the film at the ribbon interface has begun to vaporize. This launches a now-molten segment to the substrate, where it cools and solidifies [42]. The exact size of a feature depends on the material properties and thickness of the film, as well as the shape of the feature. Dots the size of 2.5 μm have been deposited, along with lines with widths of 15-30 μm [45]. The profile and aspect ratio of LIFT features are dictated by the fluidic properties of the molten metal. Aspect ratios are generally about 1:4, and the profile is rounded.

- **Laser Decal Transfer (LDT)** The LDT process is perhaps the most widely studied in research, because it has the capacity to create high-aspect ratio devices with well defined boundaries. The process is very similar to that of LIFT, but rather than using a metal thin film, LDT uses a high-viscosity, shear thickening nanoparticle ink ($\approx$100,000cP) [46]. Whereas the liquid material from the LIFT process bubbles and forms a droplet that eventually splatters on the substrate, in the LDT process, the ink separates from the surrounding nano-paste in a brittle fracture mode, and transfers to the substrate at about 1m/s, or an order of magnitude slower than LIFT[47]. After the materials are transferred, they must be sintered with a continuous-wave laser or heat in order to become conductive[46].

  The most significant advantage of LDT is that, because the nanoparticle paste remains relatively solid throughout the process, it can be used for a wide variety of applications including micro-cantilevers and micro-bridges [48] that are useful in the repair of electronics, or as interconnects to a chip or other surface[49]. Individual building block features transferred by LDT, called "voxels" can be assembled into three-dimensional shapes such as pyramids and pillars [50].

  Generally, the shape of an LDT feature is defined by the aperture used to constrain the laser profile before it is focused on the nano-paste. However, recent work has shown the viability of using digital micro-mirror devices and spatial light modulators to dynamically change the shape of an LDT feature with a resolution under 20 μm [51]. The primary limitation for LDT dimensions is that the diameter of the transferred feature must be at least 10 times the paste thickness[47]. Features as small as 2 μm have been reported [52].

- **Matrix Assisted Pulsed Laser Evaporation Direct Write (MAPLE-DW) and Dynamic Release Layers (DRL)** The MAPLE-DW process adds an additional sacrificial matrix designed to absorb energy from the laser. It is related to the use of a dynamic release layer (DRL), with the difference being that the DRL does not necessarily absorb the light, but does ablate more readily than the printed material [42]. The DRL might also absorb the laser radiation, so the two terms are used somewhat interchangeably. The laser absorption material may be located just at the interface

with the slide[53], or interspersed throughout the material[54] and can contain diverse components such as gold, titanium, TiO_2 [53], graphite, silver [54], or $BaTiO_3$ [55].

Applications of MAPLE-DW have mainly focused on organic materials and polymers. These materials are generally more transparent to light, making them less amenable to traditional LDT. Of particular interest in this process is the patterning of chemoselective or chemoresistive polymers [56][54], polymer based surface elements [55][54], and biological materials [53].

The use of a dynamic release layer is discussed in the context of LIDART in Chapter 5.

- **Nanomaterial Enabled Laser Transfer (NELT)**

  In its most simple form, NELT is a modification of the MAPLE-DW process that uses nanoparticles to lower the laser fluence threshold required to launch the material. The typical fluence required for the NELT process using silver nanoparticles of 30-40 nm is only 0.05-0.12 J/cm^2, compared to 0.25-5 J/cm^2 for metal thin films [57]. The increased absorption of visible light by noble metal nanoparticles is likely due to increased vibratory modes of surface plasmons [58]. Nanoparticles also have lower thermal diffusion than films, so heat dissipation to areas outside of the laser focal zone do not need to be compensated for. This makes NELT good for transferring sensitive materials such as the OLED semiconductors, which are heat sensitive, and absorb light in both the UV and IR spectrum [59]. The nanoparticles are separated from the ribbon by an alkanethiol self-assembled monolayer (SAM), that eases the removal of the nanoparticle and feature layer. A benefit of this process is that NELT may be used to deposit large patterns using a laser in a raster scanning zone [57].

  A modification of the NELT process of particular relevance to dry-templating is the use of a pre-templated ablative layer to launch mostly-transparent materials. In this process, the slide is pre-patterned with a thin film of gold, and the gold is coated with an alkanethiol SAM. Tris(8-hydroxyquinoline)-aluminum (Alq_3), a green fluorescent monomer was coated on this patterned surface. When a laser passes over the gold-SAM ablation layer, it launches the Alq_3 onto a substrate, but when it passes over Alq_3 without a gold-SAM layer, the Alq_3 remains untouched [60].

- **Laser Induced Thermal Imaging(LITI)** The LITI process along with similar laser thermal imaging processes, such as Radiation-Induced Sublimation Transfer (RIST) and Laser Ablative Transfer (LAT), have gained traction for the printing of OLED panels[61]. In these processes, a laser excites a light-to-heat conversion layer (LTHC) mounted between the ribbon and the transferred material. IN LITI, the LTHC layer liquefies, while in RIST, it vaporizes [62]. The change in volume presses the warm OLED material layer into the substrate, where it is patterned [63].

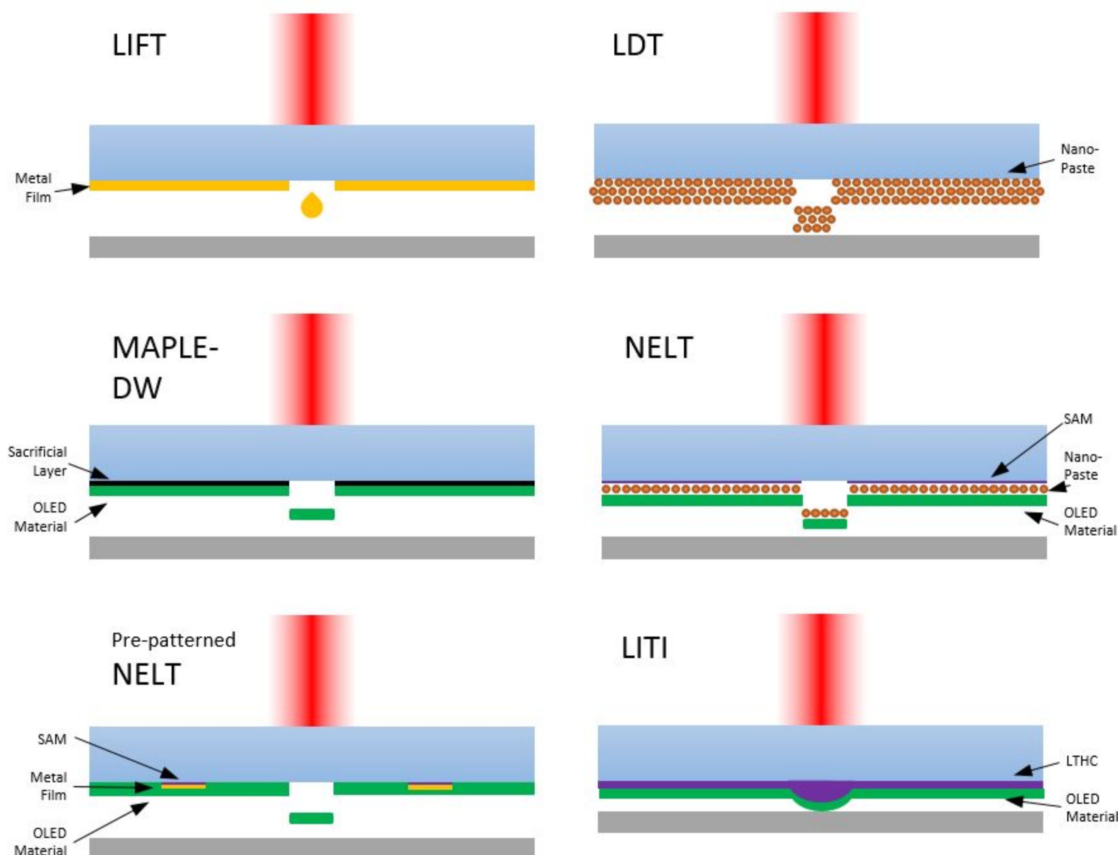

Figure 1.9: Schematic of different laser transfer methods. All of these methods are variations of the basic layout shown in Figure 1.8

1.3 Previous Work on Advective Molding in Vapor-Permeable Templates (AMPT)

The AMPT process was initially conceived by Michael Demko, and his thesis remains an important source for information in the details of the AMPT process [64]. This process has been described by various names, most notably, ”High Resolution Additive Patterning of Nanoparticles and Polymers by Vapor Permeable Polymer Templates,” but will be described as AMPT in this dissertation for clarity.

AMPT is a microfludidic process that can create high-resolution patterns through the advection-driven self-concentration of nanoparticle inks in microfulidic channels. Unlike the other methods discussed so far in this thesis, nanoparticles are fully patterned and dried in the template, before the template is removed. Because the ink is dilute during patterning, the process lends itself well to submicron resolutions, with lines demonstrated as small as

350nm.

AMPT Process Outline

In AMPT, a template consisting of polymer channels in the form of a desired pattern formed in a vapor-permeable polymer is fabricated. Nanoparticle inks are introduced to the open ends of the fill channels at the edges of the templates. As the ink evaporates, it concentrates the nanoparticles to form the inverse shape of the template.

An AMPT template is created out of a polymer material that is permeable, but non-porous, such as poly-(4-methyl-2-pentyne) (PMP) or poly-dimethylsiloxane (PDMS). The bottom of the template contains a negative image, composed of interconnected features connected to fill ports on the outside of the template. The template is cast from a master containing the same layout as the desired final pattern (e.g., Si, SiO_2 and/or SU-8). More details about template fabrication are discussed in Chapter 2.

A major advantage of the AMPT process is that the template is relatively resolution-agnostic. Pattern resolution is defined by the resolution of the master on which the template is cast, and a single master can be used to make templates multiple times. This means that masters can be fabricated through expensive, low throughput methods such as electron-beam lithography while adding minimal additional cost to the ultimate AMPT-patterned feature.

In the patterning process, shown in Figure 1.10, a clean substrate is covered with a layer of clean solvent. A template is then placed with the feature side facing down onto the wet substrate, so that the clean solvent can fill all of the channels. After any remaining bubbles evaporate, and the squeeze-film left between the templated and the substrate evaporates, nanoparticle ink is placed on the outside of the template, where it comes into contact with fill-ports that lead from the template edge to the features. As the clean solvent evaporates through the feature walls, it creates a microfluidic flow, beginning at the flow channels at the edge of the mold, and ending at closed channels on the interior of the template. This fluid flow of the clean solvent pulls the nanoparticle ink into the template channels. The nanopaticle ink self-concentrates by the same means of evaporation, so that the nanoparticles pack starting at the ends of the channels, and towards the flow channels. When the template is completely packed with nanoparticles, the temperature is raised, allowing the tightly-packed nanoparticles to completely dry out. When the nanoparticles are dry, the template can be removed, and the nanoparticle features can be sintered. A diagram of packing and sintering is shown in Figure 1.11.

AMPT Inks, Templates and Solvents

The AMPT process is especially notable for its versatility of materials and substrates. The process can be used to pattern nanoparticles and polymers on a wide variety of substrates. Table 1.1 shows a range of materials, substrates, ink solvents, and pre-fill solvents (solvent that is flooded over the substrate before the template is introduced) that have been demon-

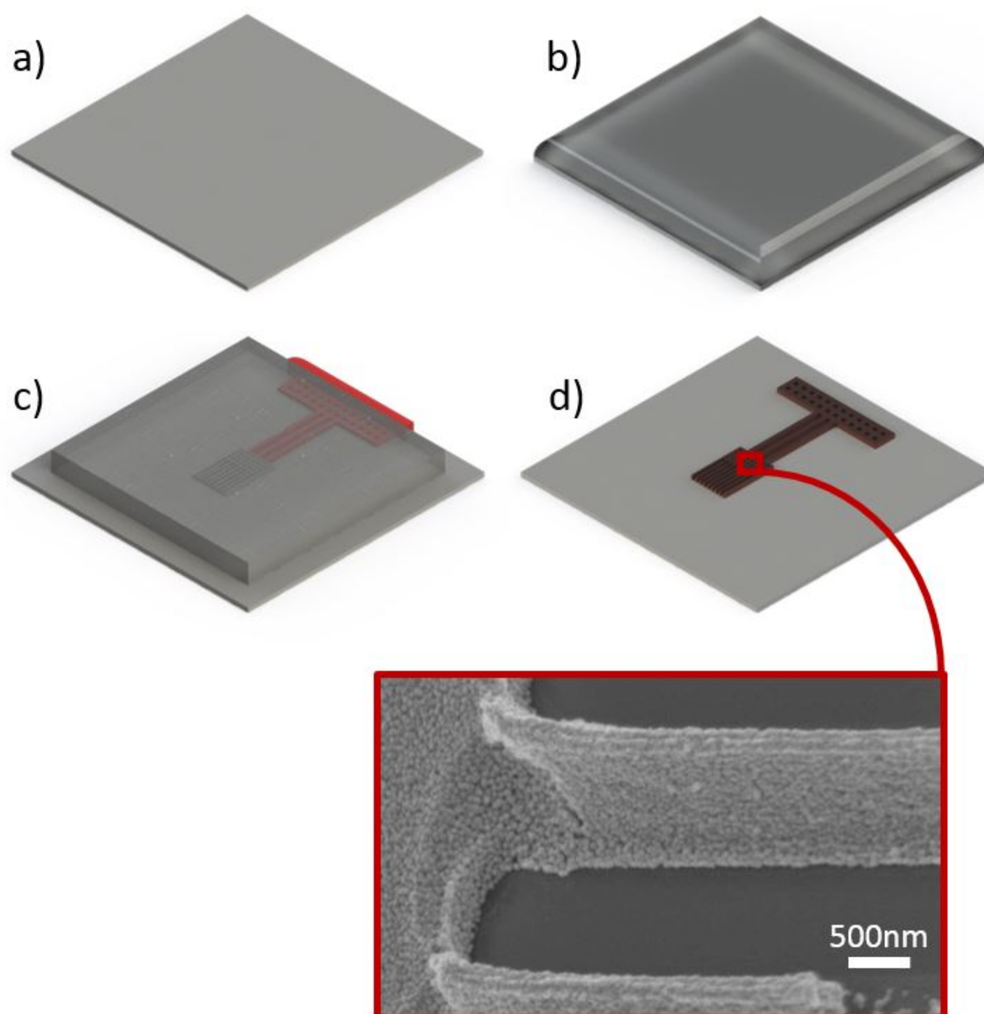

Figure 1.10: A schematic of the AMPT process. A substrate (a) is flooded with solvent (b). A vapor-permeable template is placed over the solvent so that the solvent can advect through the template and bring the template into contact with the substrate. Nanoparticle ink is placed at filling ports located on the back side of the template, and evaporation drives ink into the template (c). The ink concentrates to the point at which all available template locations contain tightly packed nanoparticles (see Figure 1.10(a). At this point, the template is heated until all remaining solvent evaporates, and the template is removed, revealing dry, cohesive patterned nanoparticles (d).

strated with AMPT. Materials used over the course of this dissertation work are shown in red. They will be discussed in later sections.

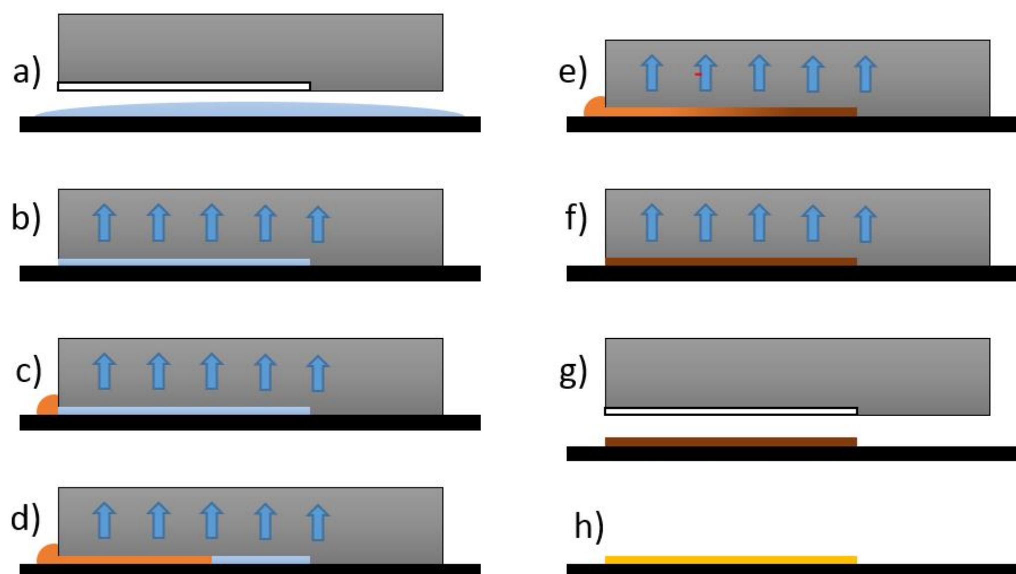

Figure 1.11: The ink filling process of AMPT, as seen between (b) and (d) of Figure 1.10. In this plot, (a) The template is brought in contact with the substrate, which is covered in solvent (b) The template is brought into contact with the substrate, and solvent begins evaporating through the template, bringing the template in conformal contact with the substrate (c) ink is introduced to the edge of the filling channel (d) evaporating solvent brings the ink into the mold (e) the ink begins packing tightly at the end of the template (f) the ink is fully packed, and the remainder of the solvent is baked out (g) the template is removed (h) the nanoparticles are sintered

Table 1.1: Table of materials, substrates, ink solvents and pre-fill solvents used in the AMPT process. Components shown in red were used in this dissertation, all previous work comes from Demko [64]

Material	**Substrates**	**Ink Solvents**	**Pre-Fill Solvents**
Silver Nanoparticles	Alumina Glass Polyimide Silicon Lithium Niobate	Hexadecane Toluene Ethanol	Toluene Ethanol

Copper Nanoparticles	Glass Silicon Lithium Niobate	Ethylene Glycol Diacetone Alcohol 1-Butanol Terpineol Ethyl Acetate	Ethylene Glycol Diacetone Alcohol 1-Butanol Acetone Terpineol
Molybdenum Disulfide Nanoflakes	Silicon	Water	Isopropanol
Tungsten(IV) Sulfide Nanoflakes	Silicon	Water	Isopropanol
Boron Nitride Nanoflakes	Silicon	Water	Isopropanol
P3HT	Silicon Polyimide	Toluene Choloroform	Toluene Acetone Chloroform
PCL	Glass	Chloroform	Chloroform
Nitrocellulose	Glass	Acetone MIBK	Acetone MIBK
Cellulose Acetate	COC Glass Polyimide Silicon PTFE	Acetone NMP	Acetone NMP
Gold Nanoparticles	Glass Polyimide Silicon	Terpineol Toluene	NMP Terpineol Toluene
Iron Oxide Nanoparticles	Silicon	Water	None
Zinc Oxide Nanoparticles	COC Silicon	Ethanol	None
PMMA	Glass Silicon	NMP	Acetone NMP
ABS	Glass	Acetone	Acetone
PVDF	Glass	DMF	DMF
Chitosan	Glass	Acetic Acid	Acetone
Cell Culture Medium	Glass	Water	Acetone

Previous Modeling of AMPT

Previous modeling of the AMPT process considered analytic models of nanoparticle concentrations within a long, thin channel of either a circular or square cross section[64]. This model assumes that there is a constant mass flux through the walls of the channel, q''. Since the velocity of the fluid at the end of the channel must be zero, the velocity along the length of the channel is given by

$$v(x) = \frac{q'' P_p}{A}(L_0 - x) \tag{1.8}$$

where P_p is the part of the perimeter consisting of the permeable polymer, A is the cross-sectional area of the channel, and x is the distance along the total length, L_0, or the channel. By introducing a characteristic time scale, t_s, the velocity can be normalized to give

$$v(x) = \frac{L_0}{t_s}(1 - \bar{x}) \tag{1.9}$$

where $\bar{x}$ is the normalized distance. If the diffusion of the nanoparticles within the ink is negligible with respect to velocity, the concentration along the channel at a normalized distance and time is

$$\bar{\phi}(\bar{x}, \bar{t}) = \frac{1}{1 - \bar{x}} u(1 - exp(-\bar{t}) - \bar{x}) \tag{1.10}$$

where $u(\zeta)$ is the step function. During the drying phase, the effective length of the channel changes, since the closely packed nanoparticles block any further flow. At this point, the effective length of the channel, $L(\bar{t})$ may be modeled as

$$\frac{L(\bar{t})}{L_0} = exp\left(- \frac{\phi_0}{\phi_f}\bar{t}\right) \tag{1.11}$$

where ϕ_0 is the initial concentration of the ink, and ϕ_f is the concentration of the closely packed channel.

While this work is useful for determining the concentration of a single simple channel, it is not effective for modeling more complex shapes. This is discussed in greater detail in Chapter 3.

Previous Work on Isolated Features

A major disadvantage of the AMPT process is that it is not well developed for isolated features. Some work had been previously done on isolated nanoparticle features, and though the process is complex and can only be used to create features with a low aspect ratio, the method was successfully used to create infrared light sensors[65].

In this process, shown in Figure 1.12, a 5 μm layer of cellulose acetate (or other polymer) is patterned by the AMPT process. The polymer must have low adhesion to the substrate.

A dilute nanoparticle ink is then dropped on the substrate and dried. Tape is then used to pull the cellulose acetate off the surface of the substrate, leaving only nanoparticles behind. The remaining patterned nanoparticles can then be sintered. Though the exact thickness of the nanoparticles deposited in this process was not reported, it is assumed to be under 1 μm.

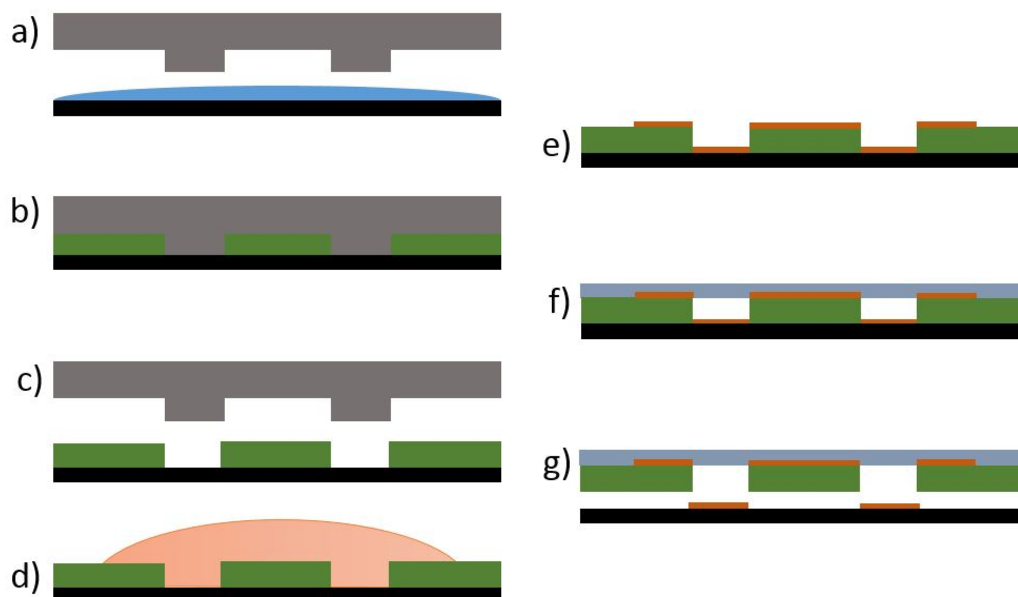

Figure 1.12: Schematic of the AMPT process for isolated features. In the process, (a) a template is lowered onto a substrate with clean solvent. Polymer solution is added (b), and concentrated through the AMPT process. When the template is removed (c), it leaves isolated features. A dilute nanoparticle ink is dropped over the features (d) and dried (e) so that a small film of nanoparticles is left. Tape (f) is placed on top of the polymer and is peeled off (f), pulling excess nanoparticles and polymer with it

The inability of this process to create high quality isolated features has been a major drawback to previous AMPT work. LIDART is a solution to the problem of isolated layers, as discussed in Chapter 6.

1.4 Summary of Existing Templated Patterning Methods

A table summarizing the existing methods for patterning metal features discussed in this chapter is included in Figure 1.13

Mechanism	Microfluidic	Lithographic Processing			Templated Patterning		Laser Transfer	
Method	AMPT	Lift-Off	Metal Etching	Damascene Processing	Gravure	Screen Printing	LIFT	LDT / DRL / MAPLE-DW
Summary	Evaporation-driven patterning of nanoparticles in permeable template	Metal deposition on a dissolvable photoresist	Plasma etching of lithography-patterned featured	Lithography-patterned trenches with metal deposited and polished	Inviscid ink loaded into the wells of a roller and pressed on a substrate	Viscous ink forced through a selectively-permeable screen	Direct laser-transfer of molten drops from metal film	Direct laser-transfer of solid nanoparticle voxels from slides
Materials	Nanoparticles or polymer on any substrate	Evaporated metal on rigid substrate	Evaporated or sputtered metal on etch-resistant substrate	Evaporated or sputtered metal in oxide channels on silicon	Nanoparticles or polymer on any pressure-resistant substrate	Nanoparticles or polymer on any substrate	Metal on heat resistant substrate	Nanoparticles, polymers or cellular material on any substrate
Resolution	1µm	1µm	>100nm	>100nm	10µm	100µm	10µm	10µm
Advantages	No residual film, low heat and pressure	Inexpensive for lithographic processing	Reliable and versatile	High resolution, no metal diffusion	High throughput, low heat	Inexpensive, low heat and pressure	High speed, inexpensive patterning	High speed, 2.5 dimensional pattern of many materials
Dis-advantages	Slow, few complex features fabricated	Low resolution, poor uniformity	Etching can damage metal or substrate	Expensive, complex and time consuming	Expensive initial cost, difficult coregistration	Low resolution, difficult coregistration	Limited shape control, expensive laser	Shape controlled by optics, expensive laser

Figure 1.13: A comparison of current templated patterning and laser direct-write methods discussed in this chapter. LIDART and improvements made to AMPT over the course of this dissertation work are not included.

1.5 Thesis Outline and Description

The main goal of this thesis is to develop templated patterning techniques to pattern conductive metal from nanoparticles. A large portion of this work is adapting the AMPT process to be used to create complex, functional structures using commercially-available metal nanoparticles. The culmination of this work is the fabrication of a surface acoustic wave (SAW) resonator fabricated from silver and copper nanoparticles using the AMPT process. Creating complex shapes using the AMPT process required developing modifications to traditional etching technology. More complex fluidic structures also require the creation of numerical modeling techniques to develop template designs that were not prone to premature drying. An additional component to this work is to speed up the AMPT process and allow for isolated features using a new laser-driven technique called laser-induced direct ablative rapid transport or LIDART.

Limitations With the State of the Art

Current methods of printing nanoparticles suffer from poor quality compared to traditional lithographic methods for metal patterning. The size, aspect ratio and fidelity of these printed features have still not reached the point in which they are a good substitute to expensive processes such as metal etching, lift-off and damascene etching. The AMPT process shows promise in creating features with a 1:1 aspect ratio, high fidelity, and sub-micron resolution, but very little work has been done to demonstrate the viability of creating complex shapes using this process. In previous works, all features patterned were long, thin channels. To make the AMPT process appealing, it must be tested and demonstrated for use in more complex features.

Capacity of the Techniques Presented in this Work

In this work, the AMPT process is used to create a surface acoustic wave resonator with resolution as small as 500nm. At this scale, SAW resonators can be considered a competitive option for cell phone applications. A new method of modeling the AMPT that can be used to improve complex mold designs to eliminate premature drying is also demonstrated. Finally, LIDART is shown to fabricate conductive silver features as small as 10 μm on flexible substrates at a fraction of the speed of the AMPT process.

Outline of the Thesis

This thesis contains a four chapters of experimental and modeling results. In Chapter 2, improvements to the AMPT template design are discussed, including master fabrication, template fabrication and inking. In Chapter 3, numerical modeling techniques are introduced that can be used to make molds that are less prone to premature drying. A discussion of the mechanisms of transport through PMP and its impact on ink selection is also included.

In Chapter 4, the application of these improvements to the AMPT process are shown on the creation of a SAW resonator fabricated exclusively through the AMPT process. The chapter also includes discussion of other devices and applications of the AMPT process, that may be of interest for future work. Finally, Chapter 5 discusses the novel LIDART approach, in which a laser is used to sinter nanoparticle features and transfer them from a surface energy-patterned template onto a flexible substrate. A summary of results and an outlook for future work is included in Chapter 6.

Chapter 2

AMPT Fabrication Techniques

AMPT is a considered a templating method rather than a direct write method because it forms nanoparticles into the shape of a mold master. This approach has two key advantages. Firstly, the master can be constructed from a wide range of materials better suited to nanofabrication than nanoparticles, including silicon, SiO_2, poly(methyl methacrylate) (PMMA) and SU-8. Masters can also be processed through means that are too expensive for large-scale fabrication, including LIGA, electron-beam lithography, deep-UV lithography, x-ray lithography and nano-imprint lithography. Since many of these lithographic methods can achieve a smaller maximum resolution than traditional lithography, AMPT can be used to produce devices at higher resolution and lower costs than traditional methods.

2.1 Introduction to Template Fabrication

The resolution of the AMPT process is limited to four factors: the resolution of the master fabrication method, the quality of the master reproduction in the template, and the template deformation and adhesion while patterning, and the completion of filling. This chapter will discuss the first three components of this process, and evaluate the advantages and disadvantages of different fabrication techniques in order to establish guidelines for future AMPT research. Template filling will be covered in Chapter 3. Materials and processing techniques were chosen so that, as much as possible all master and template fabrication approaches can be used interchangeably. Most templates can be used interchangeably for any ink.

The template fabrication process is shown in Figure 2.1. The template is the negative of a master. The master is fabricated from a silicon wafer (2.1a) the wafer has features patterned in to it (2.1b) by some combination of etching and lithography. Features have been constructed from silicon, SiO_2, and SU-8. An aluminum casting ring is attached to a finished master with SU-8 (2.1c). PMP solution in cyclohexane is then poured into the template and covered with a vapor-permeable metal-reinforced PDMS layer (2.1d). The PDMS slows the evaporation process and raises the partial pressure of cyclohexane above

casting the PMP solution. The PMP is set to cast on a level surface at 40°C. The increased temperature raises the evaporation rate to speed up the process, and increases the solubility of PMP in cyclohexane. Once the cyclohexane has completely evaporated (2.1e). Solid PMP templates are then removed from the master (2.1f). Usually, the PMP film is gently pulled from the surface of the master with tweezers while it is being sonicated in isopropanol.

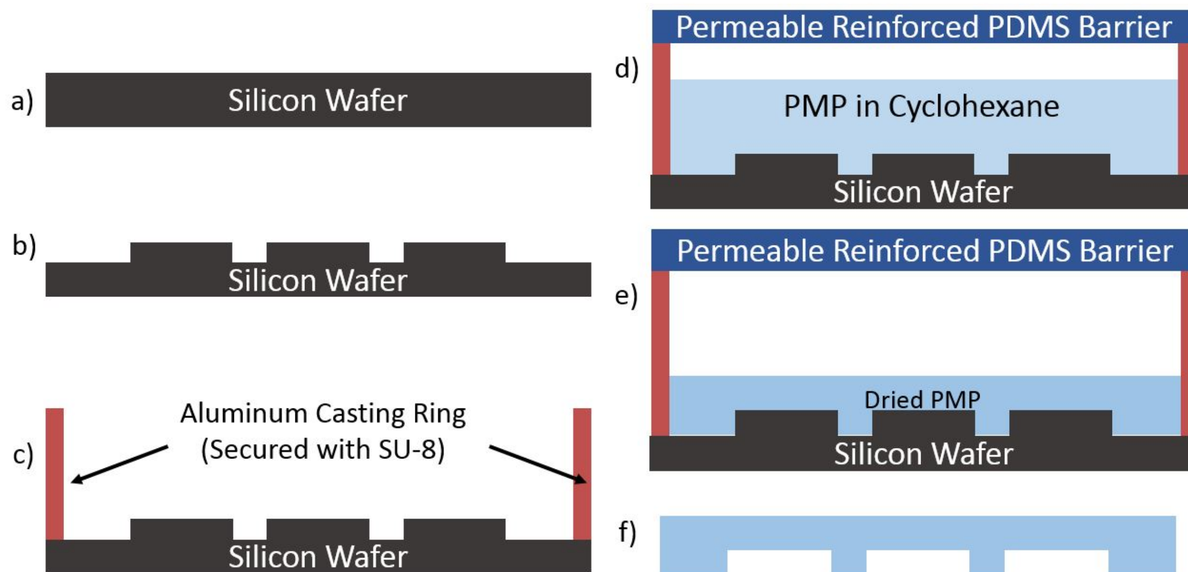

Figure 2.1: Overview of the mold fabrication process, from a wafer to the PMP mold.

This chapter begins with several approaches to master fabrication and method for mitigating template fabrication issues related to the lithography and roughness. It then compares possible template materials that have been used or proposed for AMPT, and concludes with a discussion on inks and processing parameters. In addition, this chapter serves as necessary background for a discussion of AMPT fluid modeling in Chapter 3, and AMPT device design in Chapter 4

2.2 Master Fabrication Techniques

In this dissertation, most AMPT masters were fabricated using lithographic techniques such as SU-8 photolithography and patterned with reactive ion etching. Such techniques have been developed for semiconductor processing for decades, but special considerations must be made to adapt lithographic processes for AMPT to optimize factors such as trench depth, adhesion, and roughness.

SU-8 Lithography and Imprint

SU-8 is a negative epoxy photo-polymer. It is available in a variety of different viscosities, and may be spin coated, brushed on, or imprinted. Because SU-8 is highly-crosslinked, it withstands long-term exposure to cyclohexane. SU-8 also has low surface energy, so devices may be easily de-molded from it.

SU-8 may be lithographically defined using a i-line UV light source with an alignment system for patterning or flood exposure for attaching aluminum casting rings [66].

SU-8 may also be embossed using a vapor-permeable material such as PDMS during the pre-exposure bake step. Though this cuts down on necessary lithography, the embossing resolution in atmospheric pressure is limited to about 8μm [67].

DRIE-Etched Silicon and Micro-loading

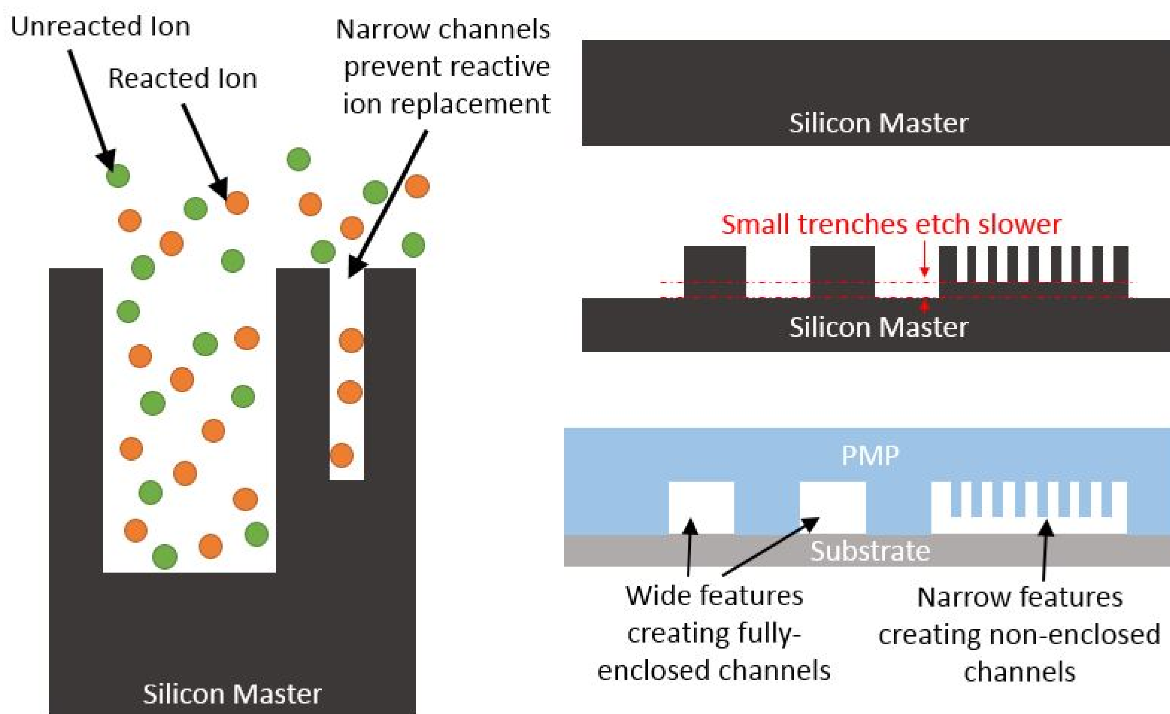

Figure 2.2: Schematic of the mechanism of aspect ratio dependent etching. ARDE occurs when channels of different aspect ratios are etched by an insufficiently dense plasma. Unreacted species are rapidly depleted in long, narrow channels and cannot be replaced fast enough. The result is a set of features that etch at different heights. The effects in AMPT are catastrophic, because they prevent complete channels from forming in the template.

In order to achieve a better resolution than 8μm, a method other that SU-8 lithography is required. Projection lithography uses a lens system to achieve an image several times smaller than the mask. The exact resolution is limited by the optical properties and wavelength of the system. For the work in this dissertation, patterns were created using an ASML DUV stepper model 5500/300 with a minimum resolution of 250nm and a Nikkon NSR-2205i11D i-line stepper with a 350nm resolution.

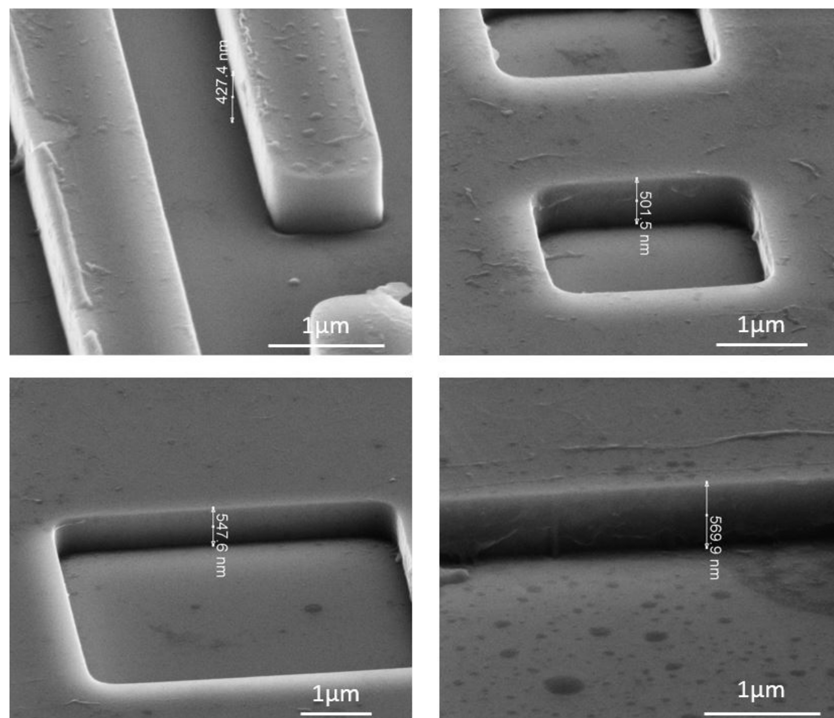

Figure 2.3: Multiple features on the same wafer, etched to different heights because of aspect ratio dependent etching. The features shown are (clockwise from the top left): 1μm interdigitated electrodes, 2μm holes in a contact pad, 5μm holes in a contact pad, and 10μm fill channel.

These lithography systems use photoresists that are easily dissolved with organic solvents, but which are robust to plasma etching. For this reason, master features must be etched out of ceramics such as silicon or SiO_2. Of these, silicon is the smoothest and most mechanically robust.

Aspect ratios on the order of 1:1 are best achieved with deep reactive ion etching, or DRIE. In DRIE, a gas such as CF_4 is energized until reactive ions are formed. These species are launched toward the substrate by an inductively generated field and into the substrate, where they react with surface atoms. These non-reactive products desorb from the surface and diffuse into the bulk gas.

The DRIE process is effective at producing features with high aspect ratios, but the exact

etch rate for a trench is determined by its aspect ratio. In narrow trenches, the diffusion rate of ions into the trench becomes the limiting step in the etching process. This is known as aspect ratio dependent etching or ARDE. The mechanism for ARDE is shown on the left side of Figure 2.2.

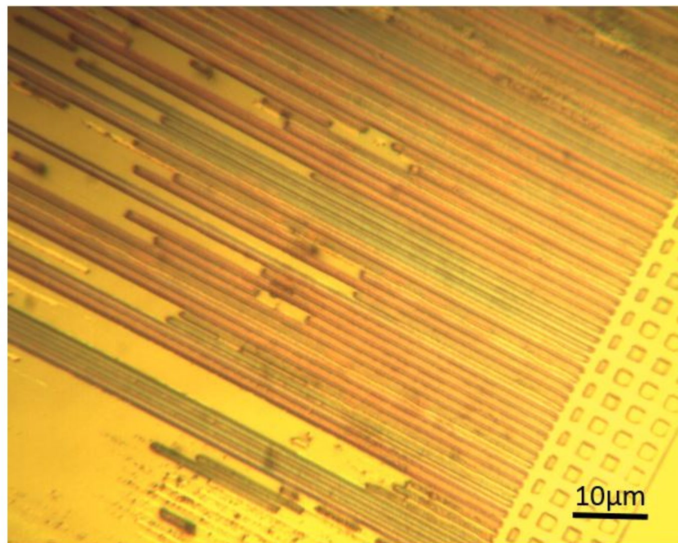

Figure 2.4: An example of a printed feature made from a template affected by ARDE. Part of the feature is not patterned because of a decreased surface area to volume ratio, while part of the pattern is filled with nanoparticles, but features that should be discrete are conjoined.

ARDE is less of an issue in traditional semiconductor and MEMS processing. The precise depth of semiconductor trenches is not a major concern. However, for the AMPT process, it is critical for all features to be etched to the exact same depth. If features are not etched deeply enough, they can cause AMPT channels to not close off properly, as can be seen on the right side of Figure 2.2. Figure 2.3 shows the results of etching on the first generation AMPT masters using DRIE. The masters show that etching depth decreases 25% between trenches that are 10μm wide and channels that are 1μm wide.

In practice, AMPT templates affected by ARDE fill incompletely because higher features stop templates from reaching the substrate in some parts. An example of this can be seen in Figure 2.4

Oxide-on-Silicon

A potential solution to ARDE is to use an "etch-stop", in which an easily-removed layer can be etched to completion over a substrate that etches at a much slower rate. With minimal refinement of parameters, this allows all features to be etched to the same depth regardless of their aspect ratio.

A second generation of AMPT templates were fabricated based on this concept, using a layer of thermally-grown SiO_2 over silicon. Etching was performed using a Surface Technology Systems (STS) Advanced Planar Source (APS) system: an inductively coupled plasma (ICP) deep reactive ion etcher (DRIE) system. The STS oxide etcher can etch SiO_2 13 times faster than silicon using a combination of C_4H_8 and H_2 gas [68].

SiO_2 patterning with an etch stop does a good job of creating uniform trenches, but it poses two other problems. Etched SiO_2 sidewalls are rougher than silicon sidewalls, and the difference in conductivity between the silicon and SiO_2 surfaces can cause charge imbalances that create trenches at the silicon/SiO_2 interface. Rough features and trenching cause the PMP to mechanically adhere to the SiO_2 features. Removing the PMP can rip off narrow features with high aspect ratios. If the PMP is successfully removed, the same thing can happen to patterned nanoparticle features. Figure 2.5 shows the both rough SiO_2 surfaces and the effect of SiO_2 roughness PMP templates and patterned features.

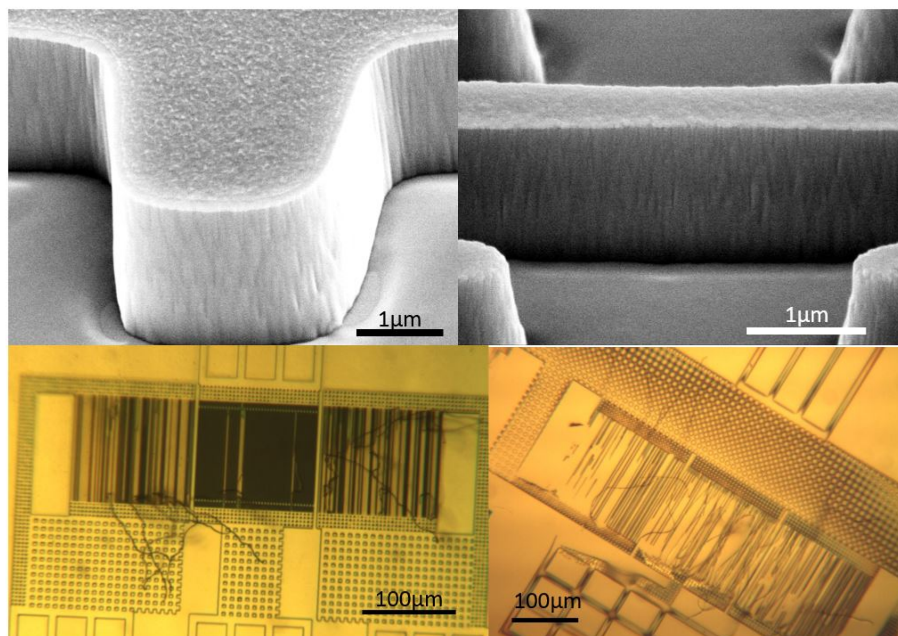

Figure 2.5: Examples of SiO_2 master freatures (top), showing roughness and trenching, both of which can cause a PMP template to become damaged upon removal (bottom).

SiO_2 roughness may be overcome by coating the template in conformal layers of nonstick polymers. A conformal polymer can smooth out rough surfaces if the polymer thickness is greater than half of the distance between asperities. The rest of this section discusses different nonstick polymer coatings for SiO_2 features.

Parylene Coating, Adhesion and Annealing

Parylene, a trade name for poly(p-xylylene), is a vapor-deposited, conformal polymer. It has low adhesion (water contact angle of 87°)[69] and extremely high chemical resistance. It comes in a several varieties. The most common of is parylene C, which has a high deposition rate and high chemical resistance. Since it is vapor deposited, parylene deposition is completely conformal, even on vertical sidewalls.

Parylene does not inherently adhere well to silicon or SiO_2. Without any additional treatment, parylene deposited on Si/SiO_2 will preferentially adhere to a solvent-cast layer of PMP. An adhesion layer is necessary to promote chemical adhesion to the substrate. The leading promoter agent is 3-(trimethoxysilyl)propyl methacrylate, also known as A174 [70].

The process for adhered parylene coating in Appendix A.

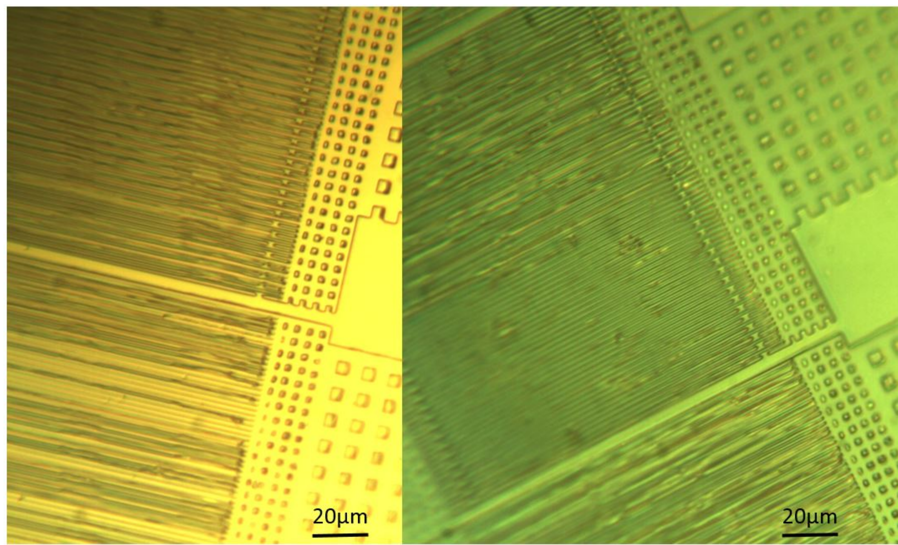

Figure 2.6: Examples of parylene that have stuck to 1μm features during the delamination process. Parylene layers look darker than the surrounding PMP features. The contrast between IDT lines with and without paryelene is especially visible at the IDTs at bottom of the left image. Parylene adhesion to the substrate can be improved though A174 silinization and annealing

Parylene C is chemically robust, but it is susceptible to UV light. It is necessary to cover parylene with an opaque material (aluminum foil, for instance) when performing UV flood exposure needed to attach an aluminum casting ring. Though parylene is not dissolved by cyclohexane, it can be weakened through long-term cyclohexane exposure, and even after adhesion treatment, it is not uncommon for parylene to stick to the PMP template during the demolding of smaller features. The strength and chemical robustness of parylene can be improved further through an annealing step[71]. Annealing crystallizes weaker amor-

phous parylene layers[72] after deposition. Though the resulting crystallized parylene layer is stronger, it is noticeably rougher[73] and more opaque.

Combining A174 silane treatment with three hours of thermal annealing makes a parylene layer that can withstand PMP solvent casting without delamination. However, the annealing step roughens the PMP too much to properly pattern. The roughness is so small (on the order of tens of nanometers) that silver nanoparticles stay within the channel, but leaking solvent diminishes the driving force of flow within the channel. Figure 2.7 shows examples of leaking dyed cellulose acetate.

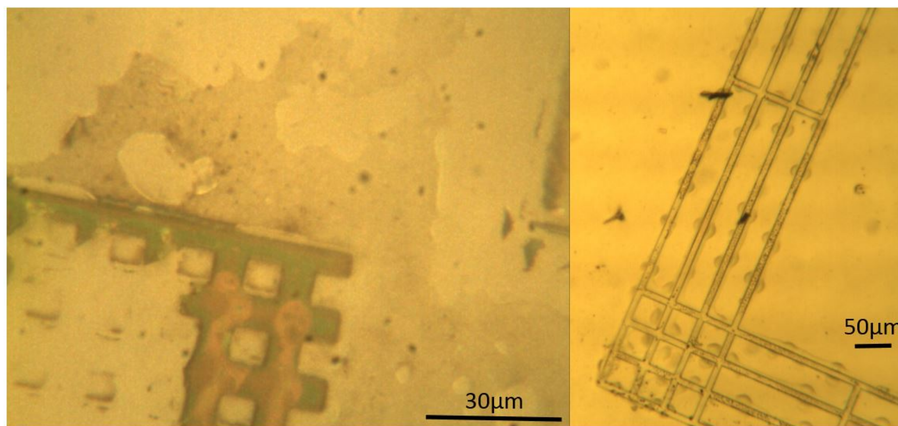

Figure 2.7: Examples of leakage underneath a PMP template that has been cast on a master coated in annealed parylene. The parylene roughens as it anneals, which causes solvent to leak into the template/substrate interface. Patterns were formed with dyed cellulose acetate, which is small enough to travel through asperities that are on the order of tens of nanometers in scale. Leaked dyed cellulose acetate appears a dark smudges above and to the right of the features in the left image, and along the edges of the channels in the right image.

Though no patterns were successfully created with parylene treatment it might be made viable through careful refinement of the anneal time, temperature and adhesion treatment. Parylene coating may be of interest for coating polymer features that are not chemically compatible with cyclohexane. The parylene layer can form a largely impermeable barrier to protect such features during solvent casting.

Fluoropolymer Deposition

Plasma-deposited fluoropolymers are a critical component of most DRIE plasma systems. Conformal fluoropolymer layers are deposited in alternating cycles with etching plasma in order to protect the sidewalls of high aspect ratio features from etching. If no etching plasma is used, the process may also be used to deposit fluoropolymer layers. The fluoropolymer layers are pinhole-free[74], and low surface energy (contact angles of about 110°)[75]. Most fluoropolymers also withstand organic solvents without damage.

Plasma deposition on AMPT templates was done in a Plasma-Therm PK-12 parallel plate reactive ion etch system. A deposition rate of approximately 20nm/min was accomplished with a C_4F_8 flow rate of 50sccm (about 85mtorr of pressure) and 100W of power.

A 40nm fluoropolymer layer improves the template demolding from the master significantly, but it does not seem to improve the roughness of the template. Ink adheres to templates coated with fluoropolymer even more than those cast from untreated SiO_2. This indicates rough template sidewalls. Despite its roughness, the template can be removed from the master because of the low adhesion of fluoropolymer. Since there is no fluoropolymer layer, nanoparticles cling to rough template features during the demolding process. Images of both templates and printed features can be seen in Figure 2.8.

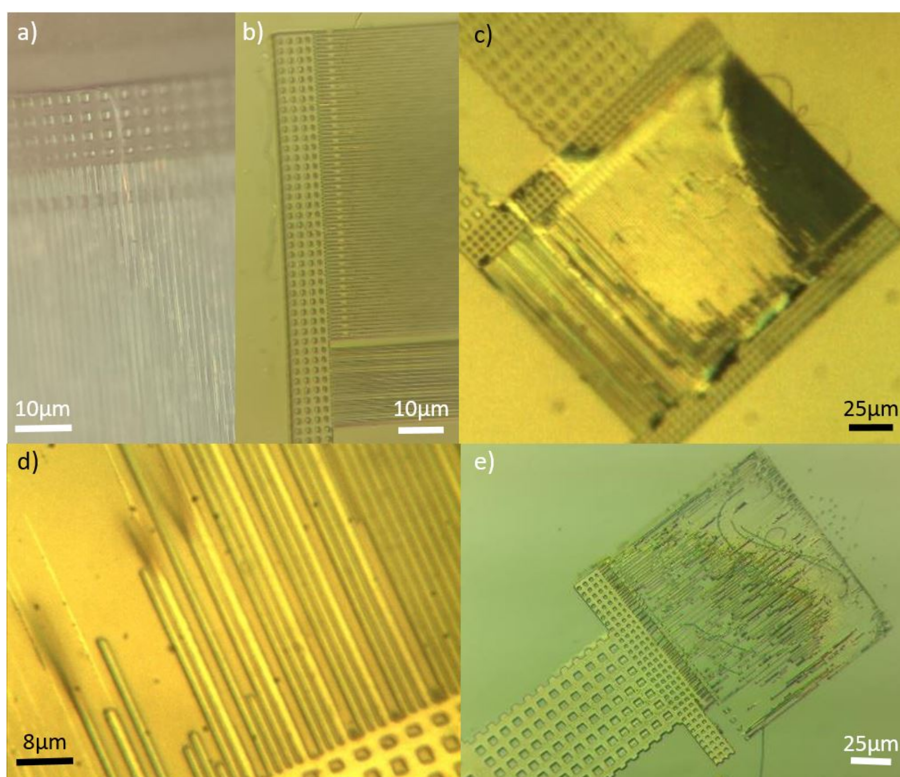

Figure 2.8: The results a plasma-deposited fluoropolymer-coated master. Images (a) and (b) show high quality patterning of 1μm interdigitated fingers in the template. (c) shows a template after patterning, with nanoparticles still attached to the 1μm template features. The substrate with remaining features after the template is removed are shown in (d) and (e).

Two-Layer Masters

AMPT features must be kept a safe distance (several millimeters) from the edge of the template so that a constant pressure is maintained around the features. All features are connected through the edges of the templates by means of fill channels. In theory, the fill channels can be indefinitely long, but their volume must be scaled with their length, so that ink does not dry out before it reaches features.

The upper limit for the aspect ratio of AMPT features is 1:1. Above this limit, removing the template from the patterned nanoparticles without damage becomes too difficult. That means that as AMPT features decrease in size, so too does the height of the fill channels. If fill channels become too wide relative to their length, the tops of the channels begin to collapse and block flow. The solution to this problem is to create a master that has features of two different heights: short, high resolution features and taller fill channels.

As previously mentioned, it is of utmost importance that masters be fabricated with a base of uniform height. In a two-layer master, this is achieved through two different materials. The high-resolution layer may be made of silicon or an SiO_2 layer on silicon. This layer is patterned through lithography and DRIE. Fill channels made of SU-8 may then be added to the patterned feature. These features can both be covered with parylene or fluoropolymer if the need arises. The process for creating a two-layer pattern is shown in Figure 2.9.

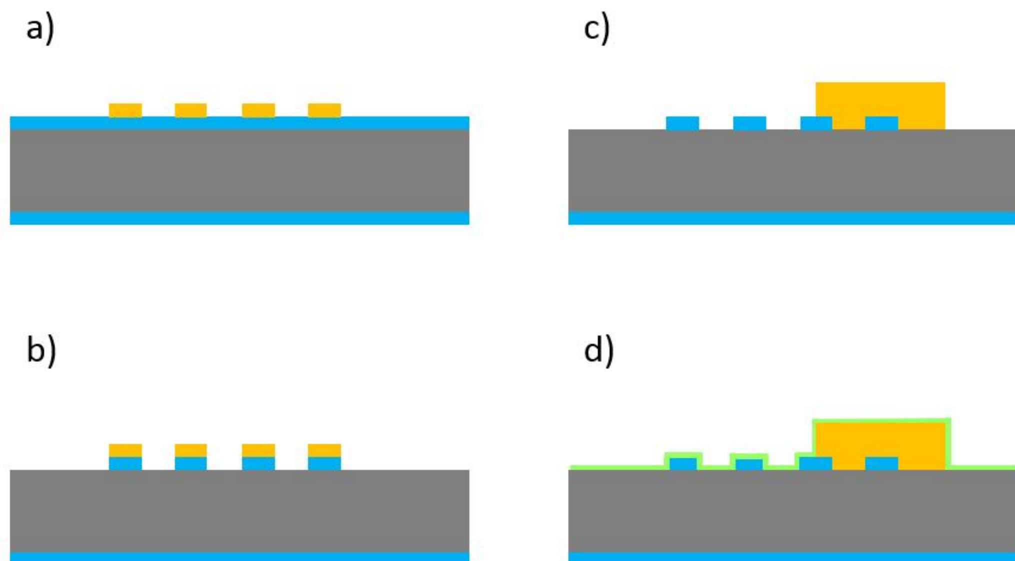

Figure 2.9: Process for creating two-layer masters. The process first starts with an SiO_2-coated silicon substrate. Photoresist is lithographically patterned on the substrate (a), which is then etched into the SiO_2 (b), with the silicon layer serving as an etch-stop. SU-8 is spun and lithographically aligned and patterned on top of the patterned SiO_2 features (c). Parylene or fluoropolymer may be optionally patterned on top (d).

During the SU-8 patterning of two-layer masters, it is critical not to overbake the SU-8 during both the pre- and post-exposure steps. The asperities of patterned high resolution ceramic features can make it difficult to remove SU-8 when all the solvent is removed. Small amounts of SU-8 can be removed with a combination of soaking in Remover PG (a stripping agent of mostly n-methyl-2-pyrrolidone) and oxygen plasma.

SU-8, like many negative photoresists, has a tendency to form a sidewall with a negative incline. This can make it difficult to remove the PMP from the master, or to remove the template from the patterned features. Oxygen plasma can be used to round off the top of SU-8 features to make it easier to remove the masters. Four minutes of 200W O_2 plasma at 20sccm of gas flow etched off about 100nm of SU-8. The templates cast off of these masters made significantly better features.

Dummy-Peg Fabrication

SiO_2 etch stops are a good method for keeping a uniform etch depth, but in some situations, the roughness and trenching in SiO_2 features may be unworkable. An alternative approach for eliminating ARDE is to fabricate dummy pegs with an identical channel width of surrounding features. This locally keeps the trench width constant, which keeps the etching depth uniform around high-resolution features.

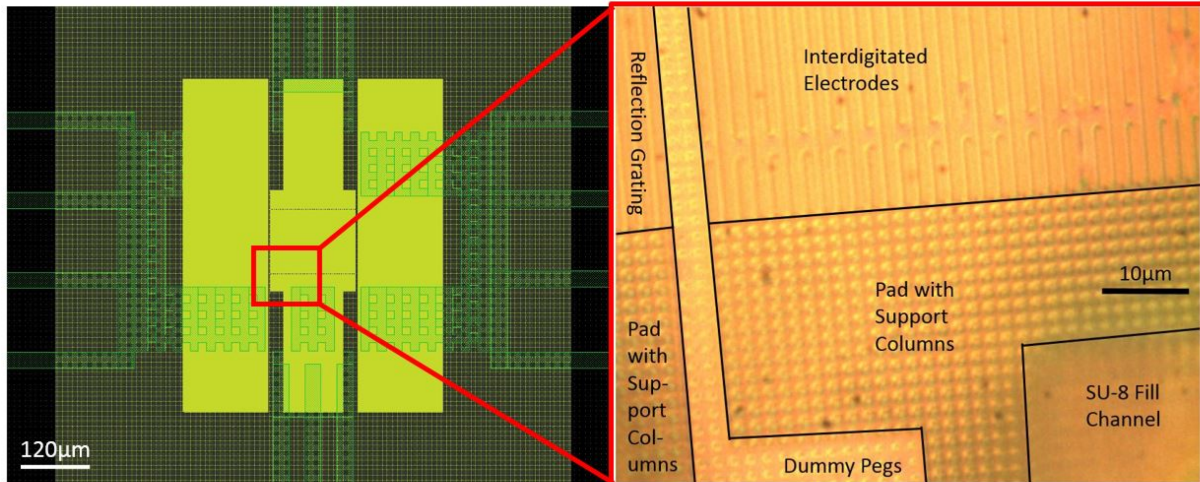

Figure 2.10: Layout of a one-port resonator using a two-layer mask (left). Yellow shows features that are etched into SiO_2, while light green shows SU-8 fill channels. Dark yellow shows SiO_2 features, while light yellow shows the locations of dummy pegs. The right image shows a close-up optical photograph of the location outlined in red on the left.

Two-layer features were designed with dummy pegs surrounding the resonators on all sides, extending half the distance of the resonator features in all directions. Since ARDE etches narrow trenches less than surrounding features, this gives a wide area around the

resonator for the template features experiencing ARDE to be stretched to make contact with the substrate. This keeps a tight seal around the template near important features.

2.3 Template Fabrication Techniques

An AMPT template is cast on a master, removed, and then used to generate a nanoparticle pattern on a new substrate with the same profile as the master. It is, in a sense, the most critical component of the AMPT process. Though it is not complex to fabricate as the masters, the template fabrication affects the speed of filling and the fidelity of a patterned feature. This section discusses template materials and the fabrication methods, focusing on poly(4-methyl-2-pentyne) or PMP.

Template Materials

AMPT templates must be vapor-permeable and non-porous. They must be cast conformally onto a master, and removed without causing damage. The template must be pliable enough to be fully conformal to the substrate during patterning, but it must be rigid enough to withstand the pressure of the patterning process. Finally, a template must be able to withstand a wide range of chemicals to be used for inks or cleaning. This section will discuss four potential polymers, whose stiffness and permeability characteristics are compared in Figure 2.11.

Evaporating solvent creates a pressure gradient along the length of the fill channel. The negative pressure at the closed end of the fill channels is the driving force that pulls nanoparticle ink into the AMPT features. A byproduct of this pressure is the potential of template deformation. High negative pressures can cause the walls of fill channels to bow inward. A stiff material resists bowing better than a flexible material does. Leading materials are compared in terms of stiffness in Figure 2.11. Experimental results show, PDMS is an effective template material only for features larger than 10μm [64]. Below that, PMP or some other stiffer polymer is necessary.

Gas permeability and solubility are key to patterning channels quickly and completely. Figure 2.11 shows examples of permeability for several materials over a range of common benchmark gases. These gases give insight into permeability, but do not tell the whole story. Some polymers, such as PMP and PDMS transport condensable gases and organic solvents faster than they transport smaller gases. The effect of the solvent properties on transport are complex, but largely depends on the critical volume of the solvent. In the case of PDMS and PMP, permeability increases with critical volume, while the permeability of Teflon AF decreases with critical volume.

The trend of increasing permeability with increased critical volume is a mixed blessing. The solvents used in AMPT ink are liquids at room temperature, and therefore have extremely high critical volumes. This means that the transport rate in polymers such as

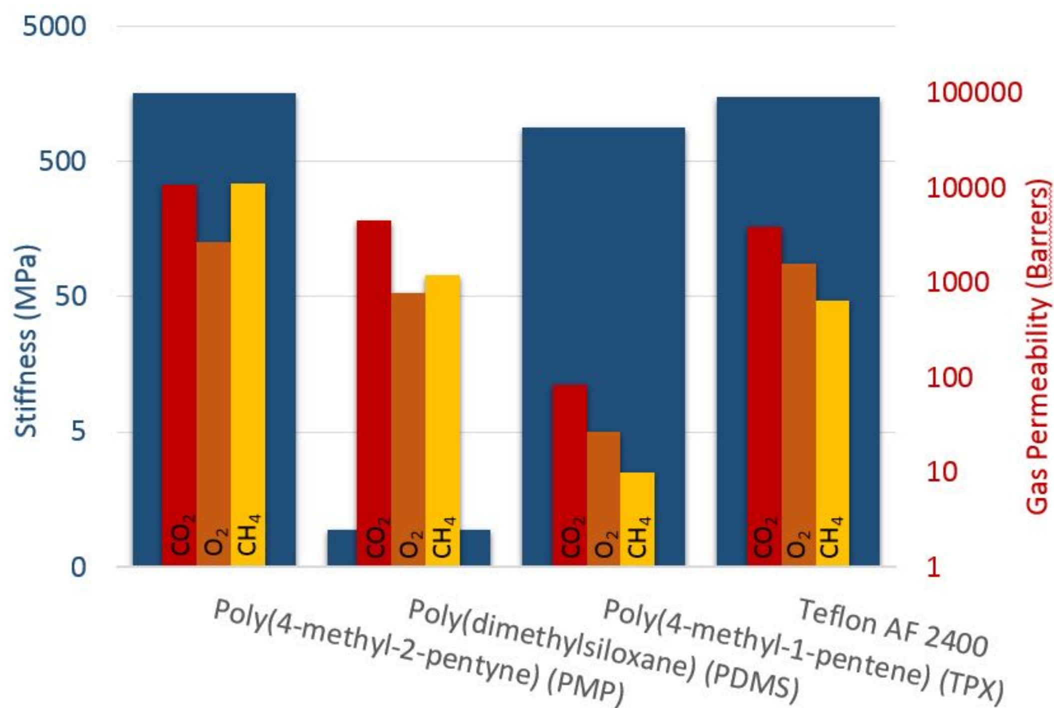

Figure 2.11: Comparison of template material options in terms of their permeability to a range of gases and their stiffness

PDMS and PMP is especially high. However, increased permeability comes at a cost. High permeability in condensable polymers is caused by the increased saturation concentration of the solvent in the polymer material. As a result, these materials have a tendency to swell in the presence of some solvents.

A more comprehensive discussion of the mechanisms of transport in PMP can be found in Chapter 3.

Poly-(4-Methyl-2-Pentyne) (PMP)

Poly(4-methyl-2-pentyne) or PMP is a rigid, glassy, disubstituted acetylene-based polymer. It is the stiffest of the available polymers, and is highly permeable. These factors have made PMP the leading candidate for AMPT templates. PMP is also extremely solvent resistant. It dissolves in only methyl-cyclohexane, cyclohexane, and carbon tetrachloride [77]. PMP is a thermoset plastic, but at about 200°C, it begins to pyrrolize. This temperature may be increased over 300°C in a nitrogen environment.

PMP is not available for purchase, and is difficult to fabricate. Polymerization requires a nitrogen environment, and several purification steps. The fabrication process for PMP is discussed in Appendix B.

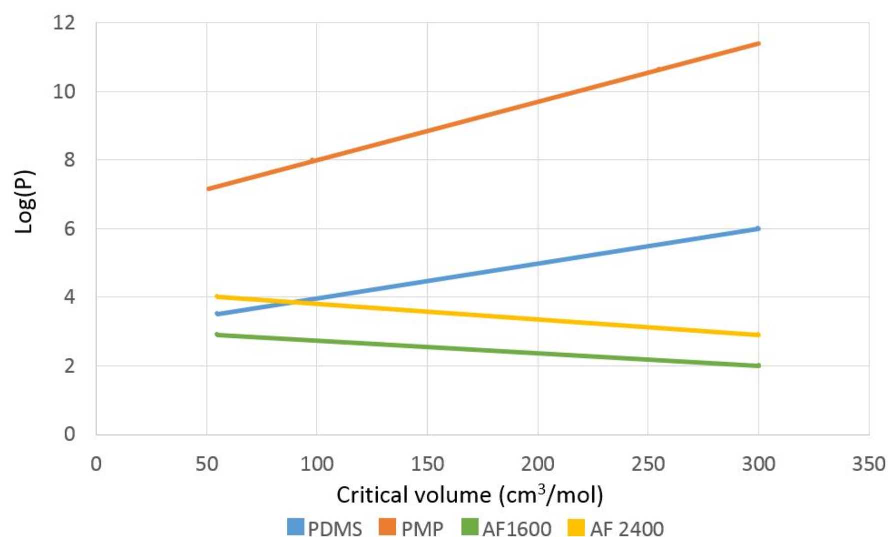

Figure 2.12: Plot showing the correlations of the logarithm of permeability to the critical volume of the solvent for different template materials. Both grades of Teflon AF decrease in permeability as the solvent critical volume increases[76]. The permeability increases solvent critical volume with PMP[77] and PDMS[78]. Data for TPX was not available.

Poly-(4-Methyl-1-Pentene) (TPX)

TPX is inexpensive and commercially available. Though it is considered permeable, its permeability is 1-2 orders of magnitude less than PDMS, PMP or Teflon AF. TPX has a surface tension of 24nM/m, making it easy to demold. TPX begins to soften at about 100°C, which means that it can be fabricated by hot embossing, but this limits its applications for patterning with less volatile inks[79]. It can also be solvent cast in cyclohexane or a range of other solvents. TPX is the least solvent-resistant polymers on the list. It can withstand simple ketones and alcohols, but it softens significantly in toluene. It may dissolve in other solvents such as NMP.

Polydimethylsiloxane (PDMS)

PDMS is a glassy silicone, or a silicon-based polymer. It is commonly used in soft lithography processes as a stamp or mold. It is an attractive choice because of its wide availability, solvent resistance, and ease of fabrication. PDMS is available in a viscous resin form. When a crosslinking agent is added, PDMS begins to solidify, particularly in the presence of heat. PDMS can be difficult to remove when it is cast on silicon or glass, but two hours of vapor treatment with trichloro(1h,1h,2h,2h-perfluoro-octyl)silane.

PDMS is available in a range of grades, ranging in stiffness and permeability. All PDMS used for this dissertation was Sylgard 184. Sylgard 184 is usually mixed with a crosslinker

at a ratio of 10:1, though a ratio of 5:1 can be used to increase the degree of crosslinking and therefore the stiffness[80]. A similar material, hPDMS, includes a vinyl group that makes the PDMS even more brittle. However, hPDMS must be spin-cast on a surface, making it difficult to generate high-resolution features[81].

PDMS makes an attractive material for large templates, however its relative lack of stiffness can hurt the quality of small features[82]. Furthermore, solvents like chloroform and toluene can cause PDMS to swell to more than twice its size[78]. Even if the flexibility of PDMS makes it a bad candidate for small features, it makes PDMS the ideal backing material for any AMPT template during patterning. PDMS, when mounted to PMP or TPX, helps to keep uniform pressure over the entire template surface during patterning, while enabling solvent to escape.

Amorphous Fluoroplastic Copolymer Resin (Teflon AF)

Teflon AF is an amorphous copolymer of 2,2- bistrifluoromethyl -4,5-difluoro-1,3 -dioxole(PDD) andtetrafluoroethylene(TFE) sold by DuPont. It is sold in two grades, 1600 and 2400. The key difference between the two is the melting temperature. The glass transition temperatures are 160°C and 240°C for AF 1600 and AF 2400, respectively. The permeability of Teflon AF2400 is slightly higher than AF1600 as shown in Figure 2.12. Because the permeability of Teflon drops off with critical volume, there is reason to suspect it may be several orders of magnitude less permeable than PMP or PDMS for larger ink solvent molecules. This makes PMP and PDMS ideal candidates for mid- and large-scale patterning, respectively. However, as pattern resolution dips into the nanometer range, Teflon AF becomes more appealing as a template material.

Teflon AF does not swell in the presence of organic solvents [83]. Teflon AF is a fluoropolymer, and therefore only soluble in fluorinated solvents. These solvents include Fluorinert (FC-22, FC-17 and FC-75), Flutec (PP50, PP2 and PP6), and Galden (HT-110, HT-135, DO2, DO2 and DO5) [84][85]. This makes it possible to solvent-cast Teflon AF using the same method as PMP. Teflon AF can also be hot embossed, by heating it about 100°C past the glass transition temperature and applying 4-7MPa of pressure [84].

The fact that Teflon AF does not swell has already made it a popular option for patterning materials at resolutions below 100nm using traditional micromolding [83]. Swelling can change the thickness and shape of the template, At low resolutions particularly, this seems to distort patterned features. This makes Teflon AF a compelling material choice for future template designs.

PMP Template Processing

The quality of AMPT pattering with PMP depends critically on the quality of the PMP, and the quality of casting on the master. This section discusses best practices for PMP processing.

Synthesis and Purification

PMP synthesis was done following a modified version of the protocol discussed by Demko[64], and it is included in Appendix B.

PMP templates may be dissolved into cyclohexane and recycled. Prior to recycling, PMP templates should be soaked in appropriate solvents like acetone and isopropanol to remove any polymer impurities that might otherwise dissolve in the cyclohexane. This is critically important for removing residual polymer when PMP templates have been used to cast polymers.

If PMP templates have been used with nanoparticles, the templates may be cleaned by ultrasonicating them with an appropriate solvent (usually the solvent of the nanoparticle ink). The solvent of the corresponding nanoparticle ink is generally a good choice. Detergent may also be added to improve wetting. Micro-90 is particularly effective at removing both nanoparticles and adhered parylene from PMP layers.

Casting

PMP is cast in a casting ring that is sealed with metal-reinforced PDMS as shown in Figure 2.13. The casting ring is made from aluminum tubing, and is attached to the substrate by SU-8 2075, which is resistant to cyclohexane. Depending on the desired thickness of the PMP, 1-5 mL of PMP solution per cubic inch of template may be used. The PDMS slows the patterning process and keeps the partial pressure of cyclohexane high in the vicinity of the drying PMP. The temperature of the drying template may be increased as high as 50°C, in order to speed up the drying process.

Delamination

PMP templates must be carefully delaminated from the master in a way that does not break or deform any features. Templates can be damaged if they are stretched, swollen or torn. Examples of features deformed during delamination are shown in Figure 2.14.

The most effective way to remove PMP templates is to first use a tweezers to carefully peel back the edges of the template. Isopropanol can then be added so that it covers the entire template. Once the isopropanol has fully permeated the PMP, the template may be slowly pulled off the substrate. This process is most effective when the casting ring is submerged in an ultrasonicating bath. If the template has been cast too quickly, residual stress can build up in the PMP. If the PMP has too much residual stress, the template will delaminate from the substrate in the presence of isopropanol without the need for peeling.

2.4 Ink Properties and Patterning Conditions

A major goal of this work was to fabricate devices using commercially available nanoparticle inks. Nanoparticle inks have decreased in cost and increased in availability as printed

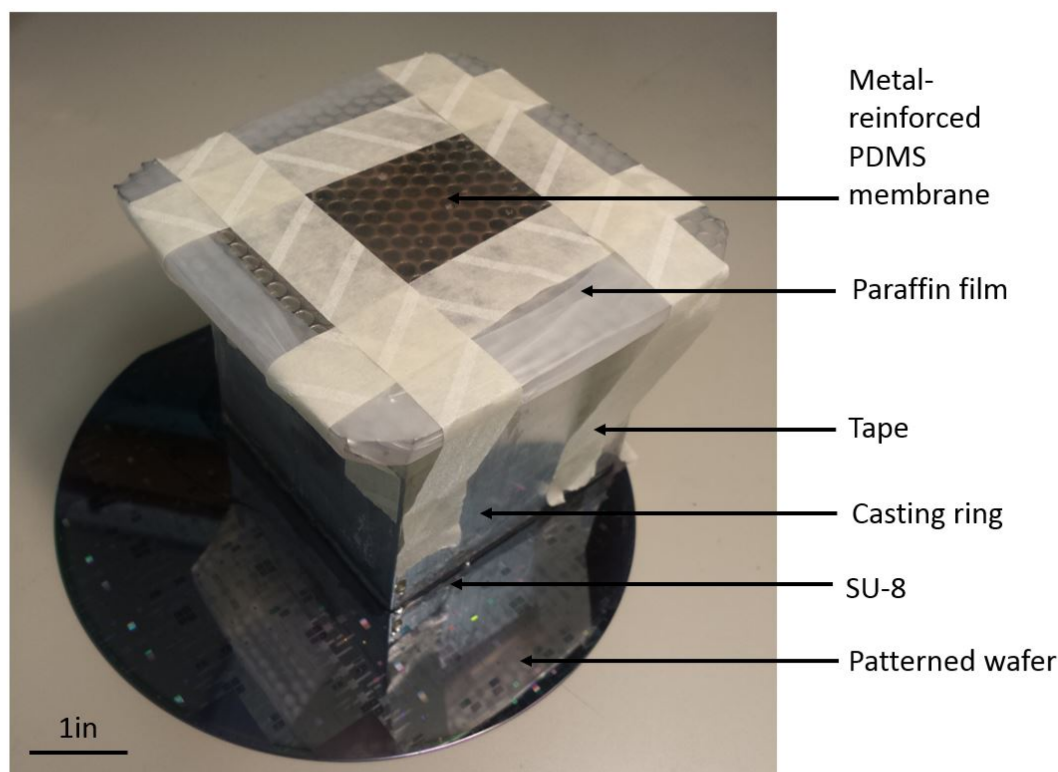

Figure 2.13: The PMP casting setup, with an aluminum casting ring attached to the substrate with SU-8. A metal-reinforced PDMS layer is mounted on top of the ring and sealed with paraffin film

electronics have entered the industrial sphere. Dilute nanoparticle inks can reach about 20% nanoparticle concentration by mass before agglomeration becomes a risk. Both silver and copper nanoparticle were used in this research.

Inviscid inks are generally manufactured for inkjet printing. Inkjet printers generate extremely small droplets of ink, so inkjet ink solvent is designed to evaporate slowly. Popular options include glycols (ethylene glycol, propylene glycol, and triethylene glycol monoethyl ether), and liquid higher alkanes (dodecane and tetradecane). Since the AMPT process is driven by vapor evaporation, stock inkjet inks pattern too slowly. Ethylene glycol patterns can take hours to form a single pattern. More volatile solvents pattern faster. Solvents with boiling points around 80° are especially desirable, as their evaporation rate can be easily changed with moderate increases from room temperature.

Inks must also be inviscid. Viscous inks can cause a large pressure gradient to form along the length of a flow channel. Ink viscosity should stay below 2cP[86] to prevent templates from distortion.

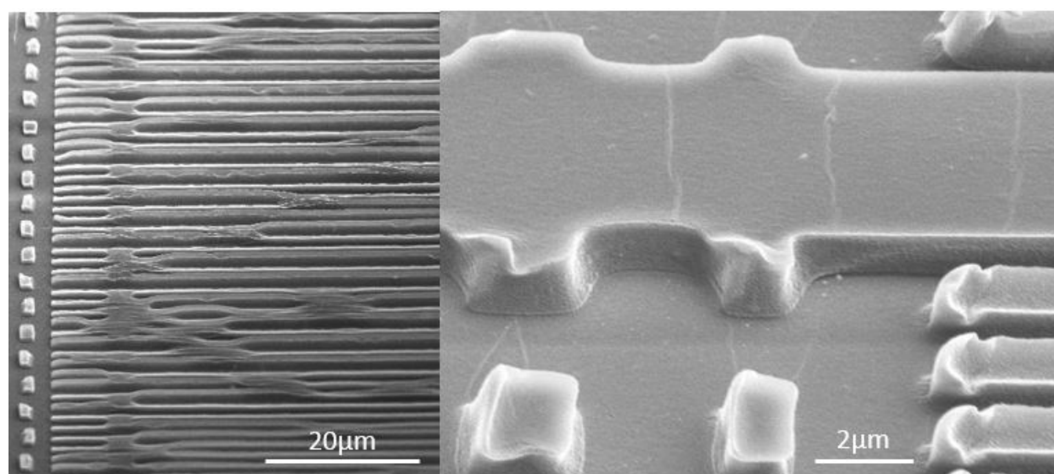

Figure 2.14: Examples of bad delamination on a PMP template showing distortion, flanging, and stiction due to swelling.

Ink Properties

Commercially available silver and copper nanoparticle inks were obtained from Advanced Nano Products Co. LTD, (Buyong-myeon, South Korea) and Intrinsiq Materials Ltd (Hampshire, UK), respectively.

Solvent	Material	Vapor Pressure @20°C	Viscosity	Boiling Point
Ethylene Glycol	Copper	12.1 Pa	16.1 mPa·s	197°C
Diacetone Alcohol		96.8 Pa	2.79 mPa·s	166°C
1-Butanol		435.2 Pa	2.54 mPa·s	177°C
α-Terpeniol		1400 Pa	67 mPa·s	217°C
Ethyl Acetate		9831 Pa	0.423 mPa·s	77°C
Ethanol	Silver	5925 Pa	1.07 mPa·s	78°C

Figure 2.15: List of copper and silver nanoparticle inks procured for AMPT patterning.

Inks are most effectively patterned when their vapor pressure is between 0.3 and 0.5atm. At this vapor pressure, pattering is accelerated, but ink solvent can be replaced before it dries. Vapor transfer through PMP increases at low temperatures, so volatile ink patterns better.

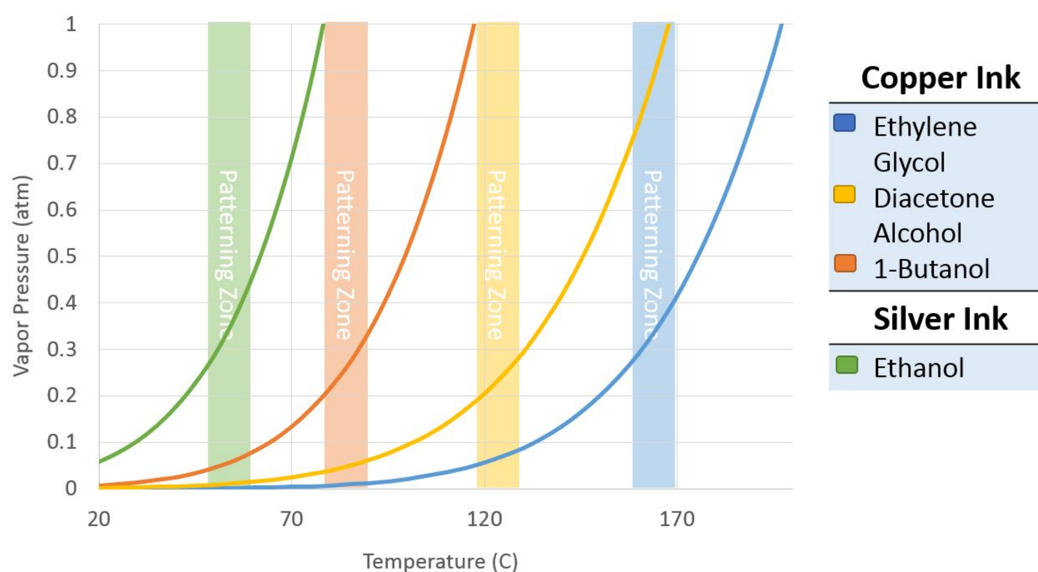

Figure 2.16: Comparison of ink solvents tested for the patterning of silver and copper nanoparticles. Plots show the vapor pressure with respect to temperature as described by the Antoine equation. Experimental results show that patterning occurs best in the "patterning zone," as indicated in the image.

Pressure and Template Backing

The AMPT process can be done at low pressures because clean solvent on the substrate is absorbed into the template, bringing the surfaces into conformal contact. However, printing at higher pressures can increase patterning efficiency by eliminating solvent leakage at the template-substrate interface. Pressures of 250kPa have been most effective, though even higher pressures may work better.

Template Delamination From Features

The final step of the AMPT process is removing template after the features have been patterned. Patterned nanoparticles can adhere to the template rather than the substrate, especially if the template walls are rough or the aspect ratio is high.

There are two approaches to limit template adhesion. The first is to smooth sidewalls by applying a parylene (Section 2.2) or fluoropolymer layer (Section 2.2). The second is to sinter the nanoparticles while they are still in their template. This is discussed in more detail in the next section.

Sintering

All nanoparticle particles must be sintered in order to gain full conductivity. Sintering may be accomplished with heat or with a Nd:YAG fiber laser. Silver nanoparticles can be sintered above 200°C [18] in either nitrogen (to keep the template intact) or air (to pyrolize the template). Sintering time depends on temperature. Features created in this thesis were sintered for 30 minutes at 260°C. Copper nanoparticles need to be sintered at a higher temperature, 350°C, because the ligands for copper are more strongly attached to the particle. Copper is prone to oxidise, so all heat sintering must be done in nitrogen.

Laser sintering is a potentially faster approach. Copper can be sintered in a laser, but the copper nanoparticle inks purchased from Intrinsiq were difficult to properly sinter without ablating (launching off the substrate). Because copper nanoparticles must be protected by a thick ligand layer, they have a high tendency for ablation. Dry copper particles frequently launched off the substrate during laser sintering as their ligands were ablated. Silver particles were successfully laser-sintered, though thermal sintering was preferred. A discussion of silver laser sintering parameters is included in the discussion of LIDART in Section 5.8.

Features may be sintered while they are still in their template so that they do not delaminate when the template is removed. Sintering should preferably be done at under 250°C and in a nitrogen environment in order to prevent the PMP from pyrolizing or melting. If PMP is exposed to higher temperatures, it can adhere to the substrate. Templates that are not damaged during the sintering process can be removed with the aid of an organic solvent such as isopropanol or acetone. If PMP is exposed to oxygen at temperatures above 170°C, it turns brittle and red. Pyrolized templates can be removed with acetone after they have been completely ashed.

Chapter 3

AMPT Flow and Modeling Techniques

This chapter considers theoretical underpinnings and modeling techniques for the AMPT process. The goal of this work is two-fold: to construct a model of the transport mechanism for ink through the template material and ink channel, and to develop tools that can be used to improve template designs. As part of this work, some potential AMPT template design rules are proposed. Future researchers considering the AMPT process can and should use these tools to build better template designs.

3.1 Introduction

Previous work on AMPT, as discussed in Section 1.3, established the theoretical basis for the filling of long thin channels assuming a constant viscosity and flux rate through the walls. Because of the limited modeling available, prior application of AMPT used layouts that did not deviate much from the model of long, thin channels. Simple interdigitated electrodes had been successfully patterned with multiple materials [64] and as electrodes for both UV and gas sensors[65][87]. As the AMPT process transitions from experimental fabrication process to a potential technique for functional devices and sensors, simple interdigitated electrodes must be combined with features of varying aspect ratios and scale, such as contact pads.

AMPT process modeling can be used to predict the risk of premature drying, and the rate of filling templates based on their geometries. Premature drying is the primary focus of the work in this chapter. It occurs when a channel in a template dries out too quickly, and stops the flow of nanoparticle inks to other parts of the template. As discussed in Chapter 4.1, premature drying was a major issue in the fabrication of SAW resonators during the AMPT process. Creating a new template with features on the scale of 200nm-1μm can cost thousands of dollars and take months of fabrication time. The time and cost of template fabrication prohibits iterative experimental template design. By comparison, a simulation can give nearly instant feedback to a template designer.

The second purpose of modeling is to predict the rate of template filling, and to optimise templates for faster filling. AMPT is a microfludic process, and the patterning speed is limited by the rate of evaporation through the template. If the process is to be expanded to a roll-to-roll system, a method for modeling fill rates of new template designs is needed to predict patterning time and the rate of solvent deposition. When linked with experimental data for a given solvent the work presented in this chapter can be used to model the fill rate. The model presented in this chapter has been broken into multiple components to minimise computational intensity so that fluid flow through large templates may be evaluated.

Theoretical Underpinnings of Ink Flow

The AMPT process consists of two linked processes: the fluidic convection of nanoparticles and the diffusion of ink solvent through the template polymer. These two topics will first be discussed individually, then linked together.

Microfluidic Flow in Mold Channels

The AMPT process is fluidic in nature, so in order to fully understand the process, the basic fluid dynamics of a microchannel must be considered.

All fluid flow is modeled by the Navier-Stokes equation [88]

$$\rho \frac{\partial \vec{\mathbf{u}}}{\partial t} + \rho \vec{\mathbf{u}} \cdot \nabla \vec{\mathbf{u}} = -\nabla p + \eta \nabla^2 \vec{\mathbf{u}} \tag{3.1}$$

where $\vec{\mathbf{u}}$ is the three-dimensional velocity of the fluid, ρ is the fluid density, p is the fluid pressure, and η is the fluid viscosity. This version of the equation assumes an incompressible fluid of uniform properties. The complete Navier-Stokes equation is unsolvable. Fortunately, in the instance of microfluidics, the equation my be simplified to unidirectional creeping flow, or Stokes flow [88].

If the fluid in question is assumed to be steady state, the first term of Equation 3.1 can be removed. If the flow is assumed to be laminar, the second term may be removed.

$$\frac{dp}{dz} = \eta \nabla^2 \vec{\mathbf{u}} \tag{3.2}$$

Laminar flow exists only at low Reynolds numbers, $Re << 1$, where the Reynolds number is given by [88]

$$Re = \frac{\rho u D_H}{\eta} \tag{3.3}$$

where D_h is the hydraulic radius, which is expressed as [88]

$$D_H = \frac{4A}{P} = \frac{2wh}{w+h} \tag{3.4}$$

where A is the channel cross-sectional area, P is the channel perimeter, w is the width of a rectangular channel, and h is the height of the channel.

Stokes flow is a good assumption for the AMPT process. For the case of ethanol flowing through a $10\mu m^2$ channel at 1m/s, the Reynolds number is only Re =0.0073. Generally, AMPT fluids travel even slower than this, so Stokes flow assumption is appropriate.

Finite element analysis of AMPT flow assumes Stokes flow with no-slip boundaries along the channel walls. In the no-slip condition, the velocity of the fluid molecules directly along the channel walls is zero.

Particle Diffusion Effects

The advective packing of nanoparticles opposes often works in the opposite direction of diffusion, so if the diffusion of particles within the ink is sufficiently high, it can adversely affect the packing of nanoparticles in an AMPT template. In its simplest form, diffusion is defined by Fick's law [89]

$$J = -\mathcal{D}\frac{\partial n}{\partial x} \tag{3.5}$$

where J is the diffusion flux, or the flow per area per time, $\mathcal{D}$ is the diffusivity constant, and n is the nanoparticle concentration. It should be noted that by Fick's law, nanoparticles diffuse in order to oppose concentration gradients.

In the case of nanoparticles, the diffusivity constant can be determined through the Einstein mobility, as given by [89]

$$\mathcal{D} = \frac{k_B T}{\zeta} = \frac{k_B T}{6\pi\eta_f r_p} \tag{3.6}$$

where k_B is the Boltzmann constant, T is the fluid temperature, ζ is called the friction coefficient, which is the inverse of the mobility of the particles. The mobility is determined by the the viscosity of the fluid η_f and the radius of the particles, r_p.

The diffusion constant for nanoparticles traveling through a microchannel is increased because of axial diffusion, as shown in Figure 3.1. This is known as the Taylor-Aris dispersion. The effective diffusivity, $\mathcal{D}$ is given by [88]

$$\mathcal{D}_{eff} = \mathcal{D}\left(1 + \frac{Pe^2}{B}\right) \tag{3.7}$$

Where B is a constant that is related to the boundary and flow conditions. B is on the order of 50 for most microchannel geometries. Pe is the Péclet number, which is given by

$$Pe = \frac{advective\ transport\ rate}{diffusive\ transport\ rate} = \frac{wu}{\mathcal{D}} \tag{3.8}$$

Where w is the width of the channel, and u is the velocity in the channel.

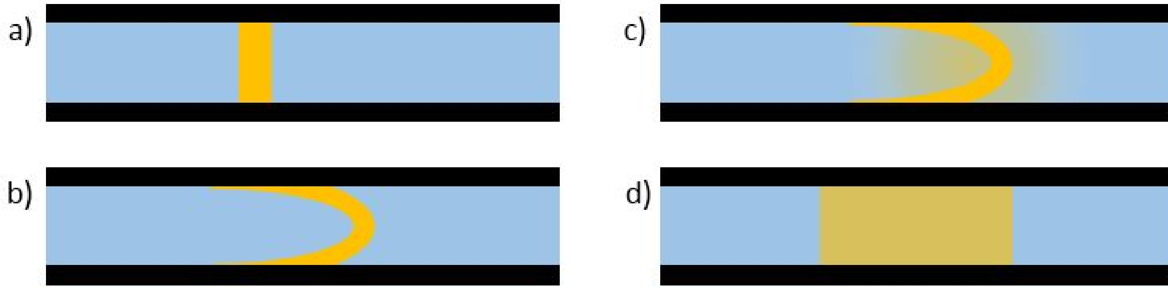

Figure 3.1: Taylor-Aris diffusion, showing (a) a concentrated bolus of ink, (b) a parabolic distortion of the bolus due to the Poiseuille flow profile (c) radial diffusion due to the distortion of the ink bolus and (d) the resulting spread-out ink profile that resembles axial diffusion.

For a channel with a characteristic diameter of 10μm, and 20nm nanoparticles in alcohol, the ratio of advection to Taylor-Aris diffusion is given by the plot in Figure 3.2

From Figure 3.2, it is clear that for the AMPT process, diffusion is less than 0.16% of the rate of advection. This is a negligible enough component that, the effects will not be considered for the rest of this analysis.

Particle Drag Effects and Limitations on Flow Assumptions

Through most of the analysis presented in this chapter, the effects of the nanoparticles within the channel is ignored. This assumption holds true given two requirements. First, the concentration of the nanoparticles must be low. This will be discussed in the next section.

The second requirement is that the nanoparticles must be small with respect to the channel walls. When a nanoparticle becomes large relative to the channel walls, it creates a larger pressure gradient along the length of the channel, which is associated with the drag caused because of the decreased film thickness between the fluid walls and the particle. This drag force may be represented in terms of the known velocity of both the fluid and the particle

$$F_{drag} = 6\pi\eta_f r_p(k_1 u_\infty - k_2 v) \tag{3.9}$$

Where η_f is the velocity of the fluid, v is the velocity of the sphere, and u_∞ is the velocity of the fluid at the same streamline as the sphere, but at an infinite distance away [91]. The coefficients, k_1 and k_2 are function so the ratio of the diameter of the sphere and to the channel, which are both expressed in terms of the fraction $\lambda = r_p/R$ (where R is the radius of a cylindrical channel) as

$$k_1 = \frac{1 - \frac{2}{3}\lambda^2 - 0.20217\lambda^5}{1 - 2.105\lambda + 2.0865\lambda^3 - 1.7068\lambda^5 + 0.72603\lambda^6} \tag{3.10}$$

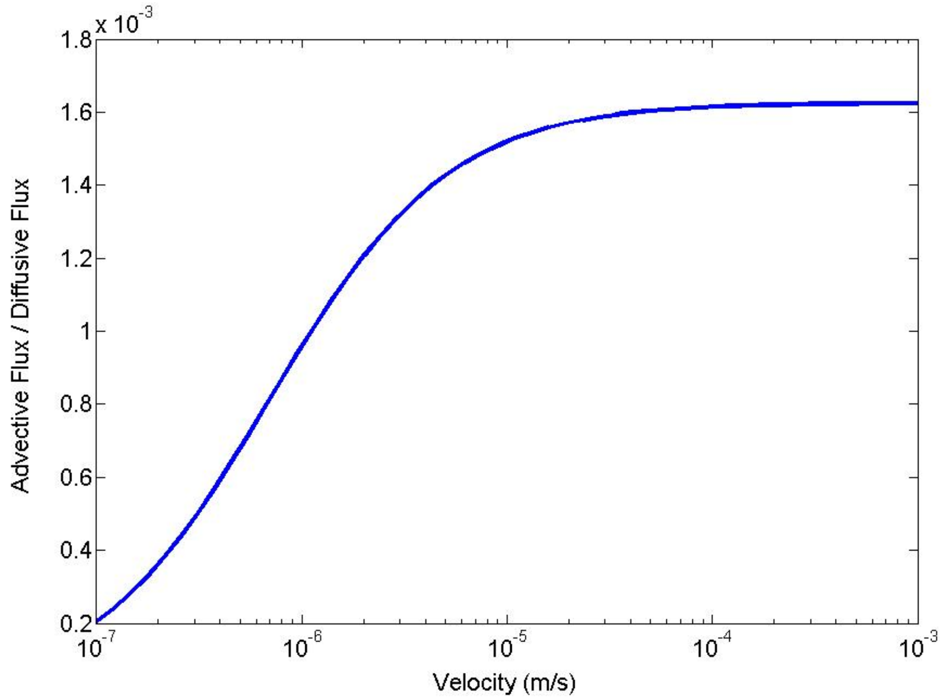

Figure 3.2: A comparison of the ratio of advective flux to diffusive flux for a 1% by volume ink with 40nm particles for a range of velocities. The particles are assumed to be going from fully dilute to close random packing (0.625 volume fraction [90]) in 1μm, which is the highest conceivable concentration gradient. Even in this extreme case, the rate of diffusion is no more than 0.16% the rate of advection

$$k_2 = \frac{1 - 0.758557\lambda^5}{1 - 2.105\lambda + 2.0865\lambda^3 - 1.7068\lambda^5 + 0.72603\lambda^6} \tag{3.11}$$

These equations are presented for a cylindrical channel of radius R, but they can be solved for a square channel of height H if the sphere diameter is scaled against the square root of the area [92] so that

$$2r_p/H = \sqrt{(\pi/4)}\lambda \tag{3.12}$$

Using the Faxen theorem for a sphere traveling through a slit, the drag force can be written as [93]

$$F = -k_2[6\pi\eta_f r_p(v - u_\infty) - \pi r_p^3 \nabla p_\infty] \tag{3.13}$$

Through the use of a geometric correction factor, the pressure gradient is linearly proportional to the channel velocity, giving [93]

$$-\nabla p_\infty = g(a)\frac{8u_\infty \eta_f}{H^2} \tag{3.14}$$

where $g(a)$ is a function of the aspect ratio ranging from 1 to a slit-shaped channel to 1.70 for a square channel.

Inserting the pressure gradient into Equation 3.9, setting the drag force equal to zero, we get the velocity of a sphere flowing through the center line of a square channel [93].

$$v_f = u_\infty \left[1 - g(a)\frac{4r_p^2}{3H^2}\right] \tag{3.15}$$

The interesting outcome of this work is that the effect of particle drag is actually quite small for most particle scales. If the particle is less than half the size of the channel height, the velocity of the particle will not drop below 85% of the channel fluid velocity. This assumption does not hold true if the particles agglomerate, but the agglomeration must quite large for a serious problem with filling to arise. These approximations hold true if multiple particles are located along the central axis of a channel, so long as the distance between particles is at least twice the particle radius [94].

Particle Concentration and Viscosity

Since the AMPT process is driven by evaporation of solvent through the template polymer, the rate of filling can be determined accurately through conservation of volume. Unlike in a pressure-driven flow, the viscosity of the fluid does not majorly affect the flow-rate through the channels. However, the viscosity should be taken into account because high viscosities can distort the shape of templates, particularly if the template is constructed from a low Young's modulus polymer such as PDMS [64].

Nanoparticle viscosity is only a relevant consideration over the range of concentrations in which the nanoparticles are evenly suspended in the ink. The saturation concentration depends on the nanoparticle and ink chemistry, but generally occurs when the nanoparticle mass fraction is between 0.2 and 0.4 of the ink. The maximum concentration can be correlated to viscosity through two constants, a and b such that [95]

$$\eta = (1 - a\phi - b)^{-2} \tag{3.16}$$

Where ϕ is the nanoparticle mass fraction and η is the viscosity of the nanoparticle ink. The maximum nanoparticle concentration can then be determined as [95]

$$\phi_m = \frac{1-b}{a} \tag{3.17}$$

It should be noted that this correlation only holds for a particular solvent-nanoparticle pair at a given nanoparticle size, solvent viscosity, and temperature[96].

The relationship between the viscosity of a nanoparticle ink and the size of the nanoparticles inside the ink is poorly understood. This is not surprising given the difficulty of creating

nanoparticles of uniform sizes, and the difficulty of varying the size of nanoparticles without changing the chemistry of the ink. At low concentration, the size of the nanoparticles has virtually no effect on the viscosity. However, as the nanoparticle concentration increases, the viscosity can increase, decrease, or remain independent of the nanoparticle size [97].

For dilute nanoparticle suspensions, it is fair to assume that the viscosity decreases with temperature. In such a case, the nanoparticles make a minimal contribution to the viscosity of suspension, so the viscosity of the solvent is a reasonable approximation for the overall viscosity. A common approximation for fluid viscosity is the Vogel equation [98].

$$\eta = exp\left(A + \frac{B}{C+T}\right) \tag{3.18}$$

The Vogel parameters for several fluids commonly used an the AMPT process are shown in Table 3.1

Table 3.1: A list of parameters for calculating the fluid viscosity based on temperature as determined by the Vogel equation [98] for solvents commonly used in the AMPT process

Solvent	**A**	**B**	**C**
Ethanol	-7.372	2770	74.68
1-Butanol	-6.257	1957	-24.97
Ethylene Glycol	-3.446	946.1	-147.0
Acetone	-3.380	553.4	-46.96

3.2 Evaporation as a Driving Force for Ink Advection

AMPT is a microfluidic patterning process by virtue of the fact that ink is advected into micro-channel by an evaporation-induced pressure gradient. Microfluidic patterning began with a similar process called Micromolding in Channels (MMIC)[99][100]. In MMIC, ink enters the mold because of capillary force. Ink is loaded from the outside of a mold with open channels, and wicked into capillary templates, where it can be concentrated through evaporation, or cross-linked with UV light[80]. The process is faster than AMPT but the geometry of MMIC structures is extremely limited. The channels must be narrow enough to keep a large capillary pressure. As a result, MMIC cannot be used to create features that cover a large area (e.g., meshes) or that “dead-end” (e.g., interdigitated fingers). These geometrical constraints in the channel construction limit the practical use of MMIC for device fabrication.

The capillary pressure is defined in Equation 3.19[101]

$$p_c = \frac{2\gamma cos\theta}{r} \tag{3.19}$$

where p_c is the capillary pressure, γ is the interfacial pressure, θ is the wetting contact angle of the liquid on the capillary surface, and r is the effective radius of the channel.

AMPT offers a major improvement over MMIC, because the driving force is less dependent on the geometry of the channels. In AMPT, the driving force for the channels is the evaporation of the solvent through the template. Unlike MMIC, it is not so simple to determine this force for a given channel geometry.

Impetus for Model Design

The mechanism for fluid flow in AMPT is the evaporation of ink into the side walls of the channels. The rate of flow in an AMPT channel is proportional to the rate of solvent flux into the walls for a given cross-section of the template. In patterns with large variations in feature size or surface area, the nanoparticle ink may dry-out in smaller features before it reaches larger features, blockages to the flow of ink (or dry-outs). A representation of channel blockage is shown in Figure 3.3. Such blockages occur in a variety of template features and can be difficult to predict due to the geometric dependency of the drying force.

One solution to variations in dry-out is to decrease the nanoparticle concentration in the ink. Low nanoparticle concentration inks are less prone to premature drying, but since more solvent must be evaporated for the same pattern, the process becomes much slower[86].

Previous work modeling the AMPT process determined analytic solutions for ink flow by assuming uniform flux of the solvent through the channel walls for long, straight[86]. A discussion of this analysis is in Chapter 1.3. The analytic model shows that nanoparticle packing begins from the far end of a long channel, but it does not give insight into template design.

This section discusses the use of finite element modeling to anticipate dry-out in order to create a template that can be patterned completely without any blockages. This work focuses on a two-part model, in which correlations between template geometry and transport through the PMP template are determined by a multi-phase finite element model. This model can be used to generate trends relating feature layout to absorption flux into the channel walls These trends used to to create finite element simulations of Stokes flow of the nanoparticle ink in complex template structures with uniform drying flux. From these models, a parameter related to dry-out, called the "flow-factor" may be calculated using post-processing. Areas identified by the model to be high-risk can then be compared to real features to verify the model's usefulness.

Mechanisms of Transport in Templates

Transport through a vapor-permeable template is dependent on a number of factors including the polymer structure, solvent, temperature, feature size, feature shape, feature density, template thickness and ink viscosity. Previous work on modeling AMPT used an arbitrary sorption rate into the channel walls[86]. Modeling spatial variation of channel flux requires an understanding of transport through the template material.

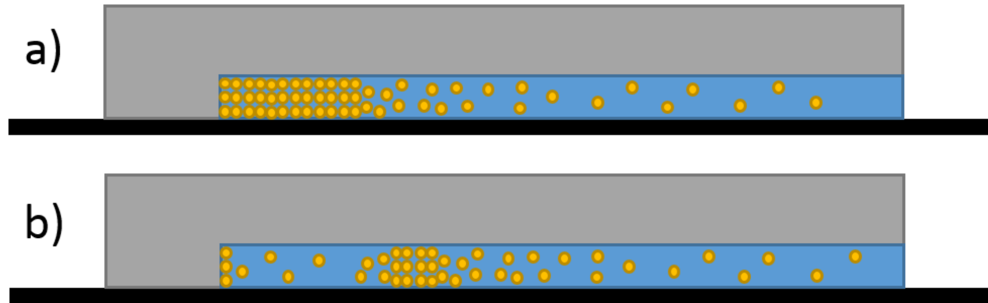

Figure 3.3: A cross section of a channel showing (a) proper molding in which nanoparticles concentrate at the far end of a channel, and gradually pack toward the open end and (b) a blockage created by premature drying part-way through the template. Concentrated nanoparticles block the passage of any more nanoparticles, creating an incompletely patterned feature. This behavior is called "dry-out".

To simplify the analysis, we only consider a system of ethanol as the solvent and PMP as the template material, neglecting the role of nanoparticle concentration. PMP is the leading material for AMPT templates due to its high permeability and stiffness[82]. Ethanol is a common solvent for silver nanoparticle ink and is known to have sorption in PMP at the ideal range (above 10% and below 100%) for AMPT patterning[77].

Solvent evaporation through a template can be considered a special case of pervaporation with only one species. Pervaporation is the process of evaporating solvent through a polymer membrane and is a common industrial technique for separating organic liquid mixtures through selectively permeable polymers[102]. In pervaporation, a membrane is kept in contact with a liquid solvent on one side, and left open to a flowing gas on the other. One of the leading approaches for describing pervaporation is a solution-diffusion model[103]. This model consists of three components, (i) the sorption of the solvent into the membrane material, (ii) the diffusion of the solvent across the membrane material, and (iii) the desorption of the solvent and evaporation into the atmosphere. These steps are shown in Figure 3.4. The concentration on the solvent-rich side of the membrane is

$$c_{i0(m)} = K_1 \cdot c_{i0} \tag{3.20}$$

where K_1 is the partition coefficient and c_{io} is the molar density in pure solvent. In steady-state with pure solvent, the concentration of the membrane at the boundary with the solvent, $c_{il(m)}$, is the saturation concentration solvent in the membrane material. The concentration on the side of the membrane facing air is

$$c_{i\ell(m)} = K_2^G \cdot p_{i\ell} \tag{3.21}$$

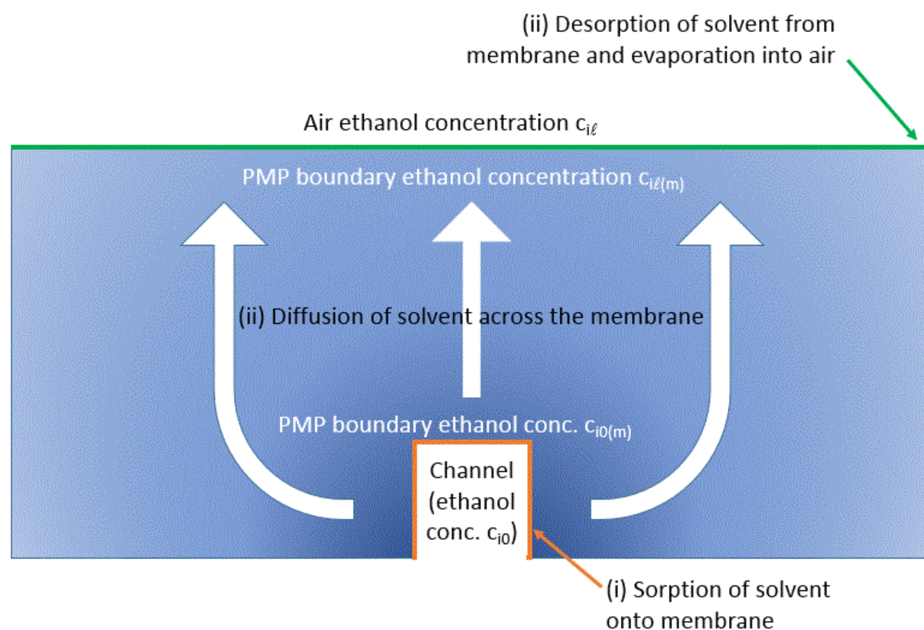

Figure 3.4: A schematic of a cross-section of a simplified PMP template with a channel in the center. Ethanol leaves the template (i) by adsorbing onto the PMP surface (ii) by diffusing through the PMP template and (iii) by desorbing from the PMP and diffusing into air

where the concentration of the solvent in the membrane at the interface is $c_{i\ell(m)}$, the partial pressure of the solvent vapor on the gaseous side of the membrane is $p_{i\ell}$, and the gas partition function that relates them is K_2^G.

If the concentration on both the channel and air interfaces with the PMP are known via the partition functions, the one-dimensional diffusivity across the membrane is defined by Fick's law

$$J = -\mathcal{D}_i \frac{dc_i}{dx} = -\mathcal{D}_i \frac{c_{i\ell(m)}}{c_{i0(m)}} \tag{3.22}$$

where J is the flux.

Transport Through Poly(4-methyl-2-pentyne)

Poly-(4-methyl-2-pentyne) (or PMP) is a glassy di-substituted acetylene-based polymer with a fractional free volume of 0.28 and a density of $0.78 g/cm^3$[77]. In a glassy polymer, solvent molecules are transported through highly-mobile free-volume elements in the polymer structure[104]. Glassy polymers with high permeability generally have stiff chains that pack poorly, creating the voids that result in a high fractional free volume[105].

The specifics of solvent transport in PMP are poorly understood. The rate of diffusion through PMP is inversely proportional to temperature and the size of the molecules, at least for molecules as large as n-butane[77]. Due to the many factors affecting transport properties in PMP, the diffusivity, permeability and maximum saturation concentration of the solvent in PMP at a given temperature must be determined experimentally. The next several sections discuss the experimental work needed to create an accurate model for PMP transport.

Diffusivity

Diffusivity is determined by the ISO 62 standard for thin films[106]. A polymer film is submerged in pure solvent and, at regular intervals the film is dried and weighed. During the initial part of the diffusion curve, the normalized mass fraction of the membrane can be expressed as

$$\frac{m_r(t)}{c_s} = \frac{2}{\ell}\sqrt{\frac{\mathcal{D}t}{\pi}} \tag{3.23}$$

where ℓ is the film thickness, $\mathcal{D}$ is the Fickian diffusion constant, and t is the time since the polymer was initially submerged. The saturation concentration c_s is equivalent to $c_{i0(m)}$ in Equation 3.20 and Equation 3.22. If the polymer that experiences negligible sorption hysteresis, the relative increase in mass of the polymer at time t is

$$m_r(t) = \frac{m(t) - m_0}{m_0} \tag{3.24}$$

A plot of this trend is seen in Figure (3.5)

Samples of PMP film were dried in a vacuum chamber for an hour, soaked in ethanol at 50°C, quickly dried on a bonded fiber wipe, and weighed on an analytic balance. The normalized mass fraction of the solvent in the PMP film was plotted against the time that the film was submerged Figure 3.5 and Equation 3.23 were used to fit the value of diffusivity for the trend. The diffusivity for ethanol in PMP was found to be $1.53 \pm 0.48 \times 10^{-6} cm^2/s$. No solvent hysteresis was observed.

Maximum Saturation Concentration

The maximum saturation concentration, m_s was determined by submerging the same film in solvent until the mass increase with respect to time was undetectable (about 5 minutes for a 110 μm PMP film). For the AMPT process, the maximum concentration of the template must not be so large as to deform the template due to swelling. If the template swells too much, it will soften and deform under the evaporation-induced pressure that drives nanoparticles through the channel[86]. Swelling can limit pattern fidelity at approximately 100% by weight. Since the rate of transport through PMP is directly proportional to the solvent saturation, the saturation should be above 10% by weight. Saturation concentration of ethanol in PMP is 38.5% or 17000 mol/m^3.

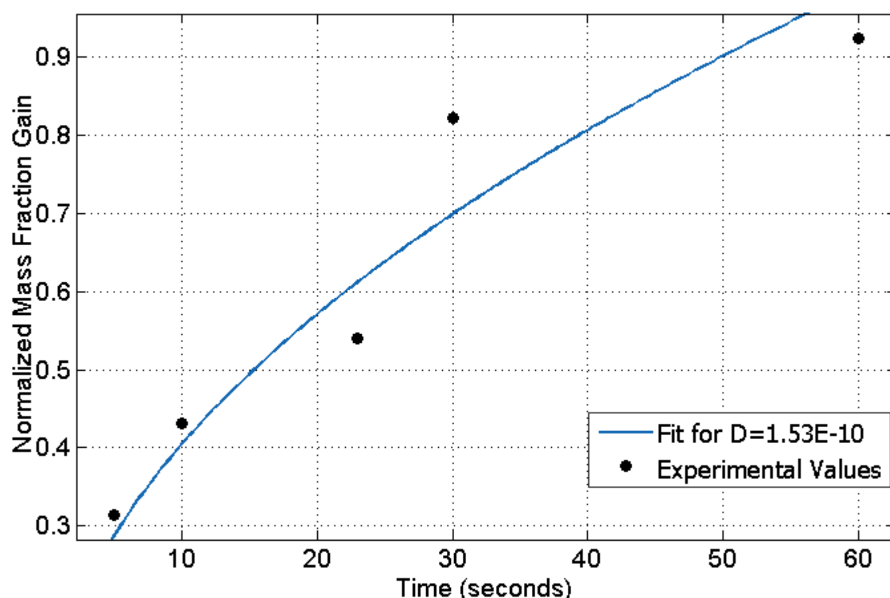

Figure 3.5: The measured and fit normalized mass fraction over time. Equation 3.23 is fit to the measurements to estimate the value of the diffusion constant $\mathcal{D}$

Permeability

Though permeability is not necessary for this model, it is a commonly compared figure of merit for membrane materials. If diffusivity is known, permeability may be used to determine the sorption parameter at a given uniform vapor pressure as shown below [107]

$$J = P \cdot (\frac{p_{i0} - p_{i\ell}}{\ell}) = \mathcal{D} \cdot S \cdot (\frac{p_{i0} - p_{i\ell}}{\ell}) \tag{3.25}$$

where P is the permeability and S is the sorption parameter.

Previous studies of gas permeability in PMP focused on the transport and selectivity of noncondensable gases, not extending to molecules larger than n-butane[108]. Inks for the AMPT process must be liquids at room temperature in order to pattern properly, so the transport of larger molecules is of interest to the development of AMPT. Transport in PMP increases with the size and condensability of a penetrating gas (see Figure 2.12)[109], so it is expected that nanoparticle ink solvents should permeate quickly through a PMP template.

The permeability of ethanol in PMP was experimentally found to be $1.84{\times}10^{-5} cm^3(STP) \cdot cm \cdot cm^{-2} \cdot s^{-1} \cdot cmHg^{-1}$ (185000 Barrer) by heating ethanol to 50°C in a sealed container with a PMP membrane on one side. The container was exposed to freely circulating air on the other side. The permeability of ethanol vapor is compared to that of other gases in Table 3.2.

Table 3.2: Comparison of ethanol (C_2H_6O) permeability with data from Pinnau[77]

Gas	Permeability (Barrer)
N_2	1330
O_2	2700
CH_4	2900
C_2H_6	5800
C_3H_8	4700
CO_2	10700
n-C_4H_10	40300
C_2H_6O	185000

3.3 Modeling Approach

The experimental data from the previous sections allow for the creation of a finite element model of solvent flux through a PMP template. A finite element analysis that models the effect of all these factors is too computationally intensive for template designs more geometrically complex than a channel. In an effort to minimize the computational needs of the finite element analysis, a series of correlations between geometry and flow rate are first developed so that they can be incorporated into a fluidic model. The chart for this analysis is shown in Figure (3.6).

Dialysis Model

The most complete model of flow in the AMPT process is the three-domain model shown in Figure 3.4. This model includes laminar flow and diffusion in the ink channel, diffusion in the PMP, and convection and diffusion in the air above the template. This model can be simplified through two assumptions.

The first assumption is that the template channel contains pure solvent (e.g., ethanol). This eliminates the complications of a two-phase solution, which requires both the advection and diffusion of nanoparticles. Any considerations pertaining to nanoparticle drying be determined in post-processing by considering the conservation of volume of the ink (see Section 2.12). This assumption holds true for nanoparticle sizes below half the channel size and concentrations below 20%-40%.

A typical 1μm tall template has a Reynolds number of roughly 10^{-12}, which guarantees Stokes flow regardless of ink viscosity. The pressure gradient that drives flow in an AMPT channel can deform the template if the initial ink viscosity exceeds 5 cP[86]. The initial viscosity of the ink can be correlated to nanoparticle size, nanoparticle concentration, solvent viscosity and temperature[96], so integration of viscosity change into the process model is not necessary.

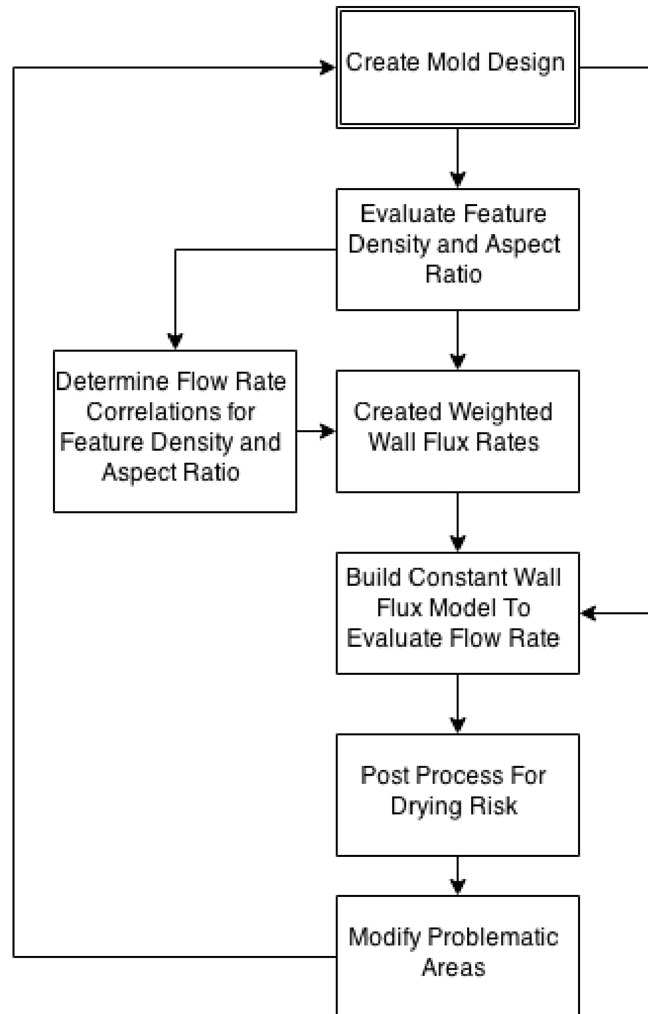

Figure 3.6: A flowchart for evaluating the pattering quality of a vapor-permeable template. The chart simplifies flow modeling by first creating correlations between the template geometry and flux through the wall. Post-processing is then applied to determine the likelihood of premature drying.

The air domain above the template can be also removed to reduce computation time of the model if the assumption that the ethanol concentration at the PMP-air interface is $c_{i\ell(m)} = 0$. The rate of diffusion for ethanol in air $(11.81 \times 10^6 m^2/s)$[110] is ten orders of magnitude higher than that of ethanol in PMP $(2.63 \times 10^{-4} m^2/s)$, so air at the interface with the PMP is effectively a sink for ethanol.

The resulting model after these simplifications consists of only two domains. The ethanol in the flow channels is modeled with laminar (Stokes) flow, as shown in Equation 3.26[111].

$$\rho \vec{u} \nabla \vec{u} = -\nabla p + \mu \nabla^2 \vec{u} \tag{3.26}$$

where ρ is the fluid density, $\vec{u}$ is the fluid velocity vector, p is the pressure, and μ is the fluid viscosity. Diffusion through the PMP is modeled by Fick's Law Equation 3.22)[112]. The two domains are coupled through their interface using Equation 3.27 and Equation 3.28 for the ethanol-filled channel and PMP template, respectively.

$$u_{boundary} = -M\frac{(K_1 \cdot c_{i0} - c_{i0(m)})}{V_{m,ethanol}} \tag{3.27}$$

$$J_{PMP} = M(K_1 \cdot c_{i0} - c_{i0(m)}) \tag{3.28}$$

In both Equation 3.27 and Equation 3.28, M is a stiff-spring velocity, which is used to express a Neumann statement about the flux across the boundary, but achieves a Dirichlet condition for the concentration on the interface. The stiff-spring velocity gives for an ethanol flux across the interface, even though both sides of the interface are at saturation concentration[113]. The exact velocity specified by M has essentially no effect on flux, and is set arbitrarily high (i.e., $10^4 m/s$, as recommended by COMSOL)[114]. The inlet to the flow channel is treated as laminar inflow with an inlet pressure of 0 atm, and the bottom surface of the channel (the substrate) is treated as a no-slip wall.

Effect of Fill Density

The experimental results discussed in the previous section inform a one-dimensional analytic diffusion model of ethanol through PMP. The geometry of a three-dimensional template can significantly change the local concentration of solvent. If two features are adjacent in a PMP template, the solvent flux from each channel contributes to the concentration of ethanol in the template. This increased ethanol concentration slows the rate of flux through the walls of both channels. Closely-spaced features are common in AMPT template design, so special consideration must be made to the effect of feature density on the flux rate through channel walls.

The geometric effects on drying rate in a channel were analyzed using COMSOL Multiphysics, with the creeping fluid flow of the ink through a channel linked to the diffusion of ethanol through a three-dimensional PMP template. The boundary conditions for these models can be seen in Figure3.7. The symmetry conditions on either side of the modeled domain means that the model describes an infinite array of channels. Average channel flow rate is determined for two different parametric variations.

The first parametric sweep considers 1:1 aspect ratio channels ($w_c = h_c$) with varying distance between fill channels w_m. When the channels are very close together, the PMP between the channels becomes nearly saturated with solvent. This lowers the flow rate between the channels and causes a sharp loss in flow rate when $w_m \leq w_c$. The trend can be seen in Figure 3.8, in which the flow rate (as a percentage of the maximum flow rate) is plotted against the fraction of the surface covered by channels.

The aspect ratio of the channels also affects the rate of drying. As solvent flux is ultimately directed through the top of the template where it can evaporate, the sidewalls of

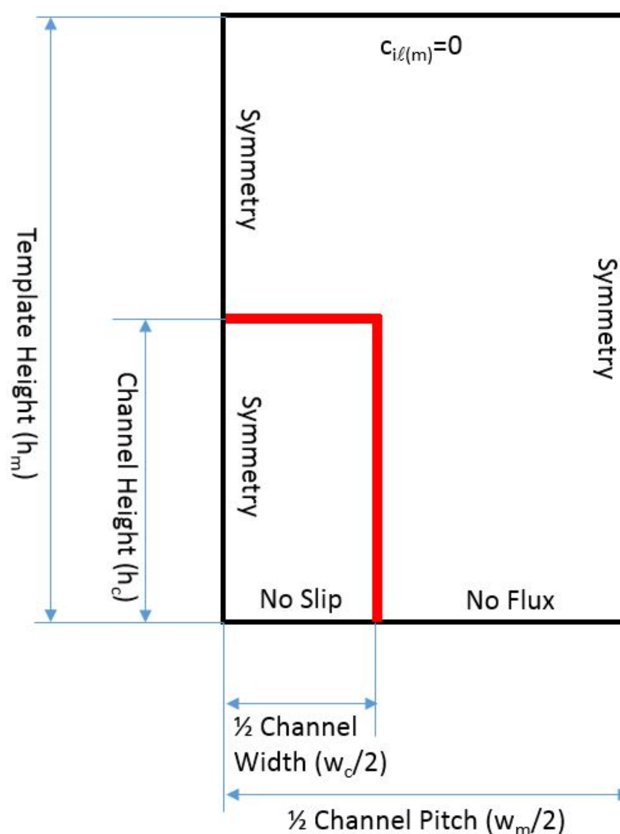

Figure 3.7: The boundary conditions for the finite element model used in the parametric pitch studies in Figure 3.8 and Figure 3.9. The height of the template is kept constant at 200 μm, which is a common thickness for PMP templates. Since $h_m >> h_c$, the ethanol velocity in the channel scales linearly with template height.

the channel sorb flow more slowly than the top of the channels since the area above the side walls becomes saturated faster. When the channels become wider than their height, the proportion of flux through the side wall decreases and causes the average flow into the walls to increase Figure 3.9.

Constant Flow Modeling

In the previous section, correlations were developed for finite element models in which fluid flow in the channels was coupled with the diffusion of solvent in the PMP templates. These results can be used to determine different flow rates for each channel wall based on the channel's geometry without the need for finite element modeling.

For this work, a the correlations shown in Figure 3.8 and Figure 3.9 are used to as formulae for the approximate flow rates into walls. An example of this modeling can be seen

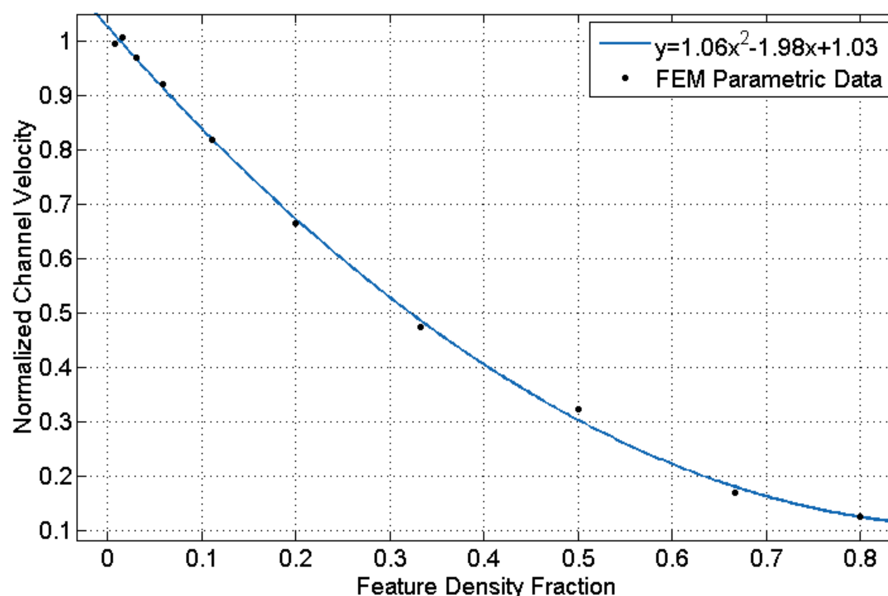

Figure 3.8: Normalized flow versus channel feature density for channels with a 1:1 aspect ratio. The velocity of ethanol through the channel decreases with the increasing density of the walls

in Figure 3.10, with each color indicating a different normal velocity into the walls of the channel.

These wall velocities are input into a creeping flow fluidic model to determine ethanol velocity throughout the template. The output for this model in COMSOL is shown in Figure 3.11.

Post Processing of Locational Drying

For this model, drying is considered in terms of a control volume within a segment of a template channel (Figure 3.12). Ink flows into and out of the control volume by means of fluidic advection. Ink solvent also leaves the control volume when it is sorbed into the PMP channel wall. The volumetric balance for the control volume is given by.

$$\dot{V}_{in} = \dot{V}_{out} + \sum J_{walls} \tag{3.29}$$

Control Volume Analysis

From Figure 3.12, the rate of drying for a single cross-sectional control volume segment of a channel is equal to the advective flow into the control volume minus the advective flow out of

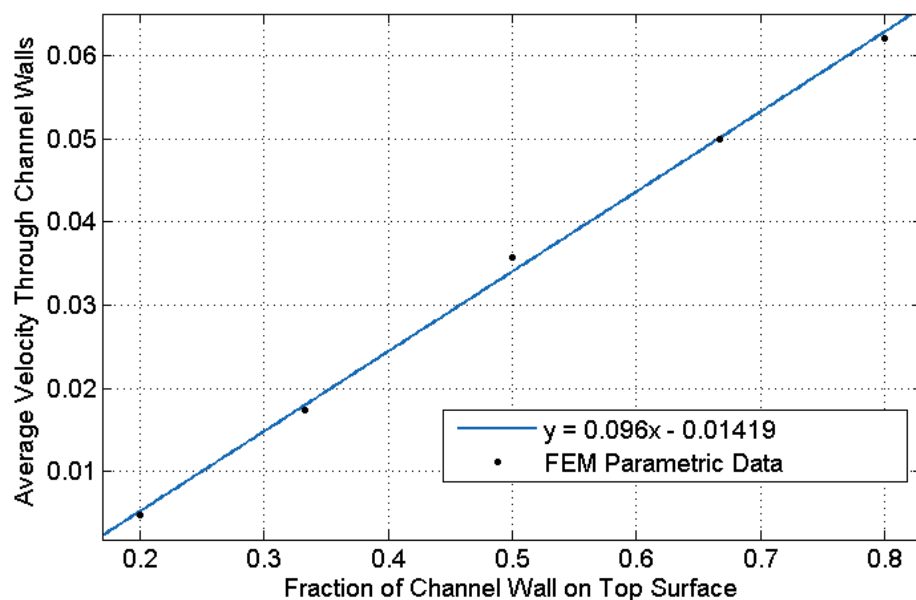

Figure 3.9: Average velocity through channel wall (absorption rate) plotted against the fraction of the channel wall that is a top surface

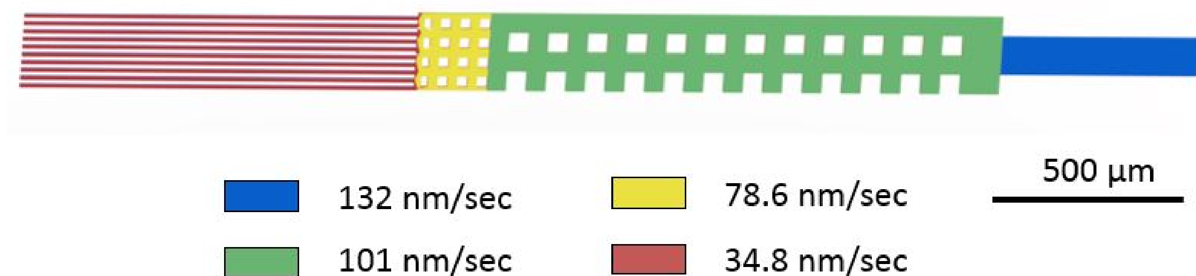

Figure 3.10: Zones of uniform flow rate determined by the correlations from Figure 3.8 and Figure 3.9. In this case, since the pitch of all the features is uniformly 1:1, correlations are determined by the varying aspect ratios of the template.

the control volume. For complex template geometries, the same control volume analysis may be applied to arbitrarily small discrete segments with some modifications. If the template is divided into an array of small control volume elements, most elements will not border a channel wall. Elements near, but not adjacent to, a wall will experience the effects of drying even though there is no direct flux into a wall bordering this element.

It is tempting to try to correlate flux leaving a control volume to vorticity, as the influence of wall sorption would induce a curl in the flow velocity. This is appropriate in straight

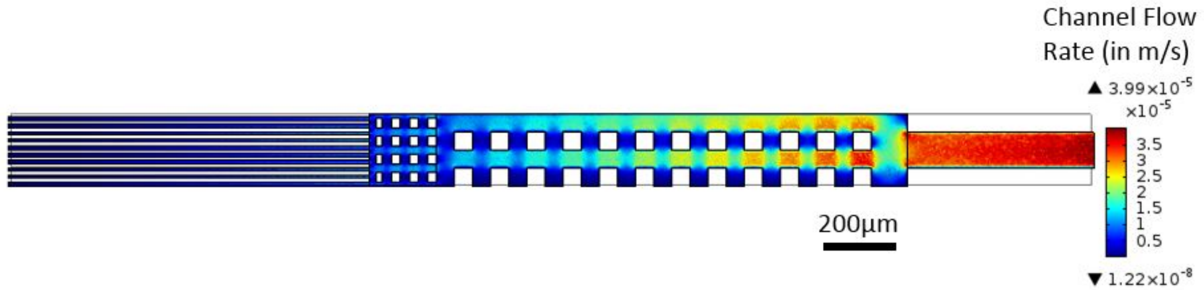

Figure 3.11: COMSOL model output showing the creeping flow velocity magnitude through the mid-plane of the model. The constant flow rates through the walls are shown in Figure (3.10

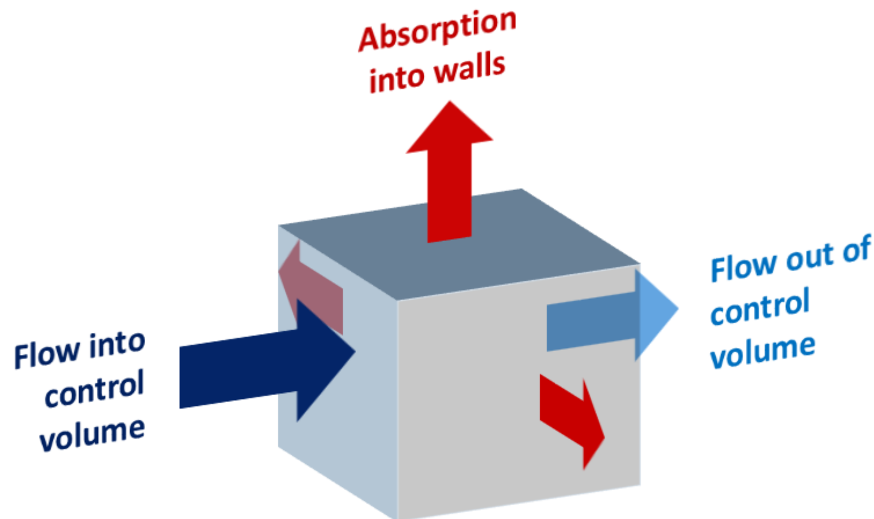

Figure 3.12: Control volume example shown in Equation 3.29

channels, but in a template with sharp turns, the angular component of the fluid velocity moving around a corner is indistinguishable from the influence of wall soprtion. Instead, a weighting factor (Equation 3.30) is introduced in post-processing of the velocity finite element model (Figure 3.11) to determine the relative effect of sorption into the walls for each control volume element.

$$W_D = \sum_{x_{min}}^{x_{max}} \sum_{y_{min}}^{y_{max}} \sum_{z_{min}}^{z_{max}} \frac{Q_{wall}(x, y, z)}{\sqrt{(x - x_0)^2 + (y - y_0)^2 + (z - z_0)^2}} \tag{3.30}$$

Equation (3.30) sums the distance from the control volume to all the walls of the channel, weighted inversely to their distance from point (x, y, z). The bounds of the summation (e.g. x_{min} and x_{max}) should be large, but not so large as to make calculation impossible. In

Figure 3.13 the factor was calculated for 8 elements in every direction. This weighting factor can then be implemented to find the fill factor for the given location. The fill factor is a qualitative indication of the likelihood that an area will properly fill without drying out prematurely. The fill factor is given by Equation 3.31

$$f_{fill} = \frac{| V_{fluid}(i,j,k) |}{1 + \frac{W_D(i,j,k)}{\overline{W_D}}} \tag{3.31}$$

where $\frac{W_D(i,j,k)}{\overline{W_D}}$ is the weighting factor of the particular point normalized to the average weighting factor for the entire layout. The fill factor can be seen in Figure 3.13. To make the image, fill factors were calculated in three dimensions using MATLAB, then averaged along the vertical dimension. This gives the user an understanding of template dynamics from overhead. Since most templates have a uniform height, this two-dimensional presentation of the fill factor is sufficient to evaluate the template shape.

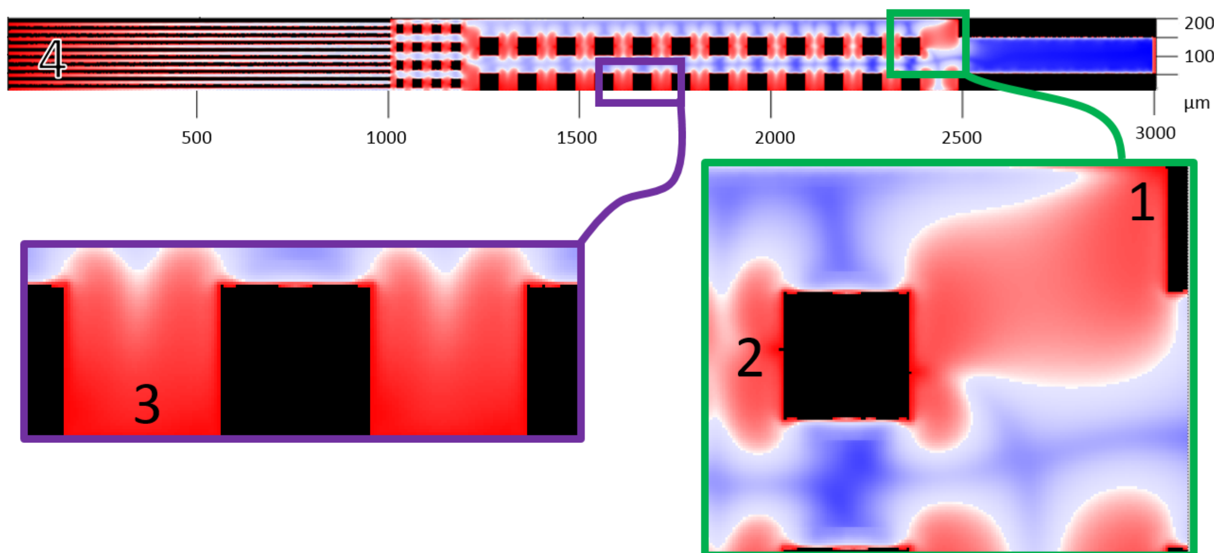

Figure 3.13: Color map of the fill factor for the sample shape shown in Figure 3.11 and Figure 3.10. The fill factor is used to determine the quality of filling. In this image, fill factors in the bottom ten percent are highlighted red. The remaining are highlighted blue. These red locations show areas of key concern, where prematurely dried nanoparticles are most likely to block flow. Four call-outs (1-4) of areas of incomplete patterning due to premature drying are compared to images of shapes printed with the AMPT process in images Figure 3.14

Validation With Experimental Results

Figure (3.13) shows the model's predictions for the areas most likely to prematurely dry in red. All channels with closed ends appear in red, though these areas are of minimal concern as they do not pose any blockage risk. The same is true of channels open on both ends to slowly drying (blue) channels, shown in location (2) of Figure (3.13).

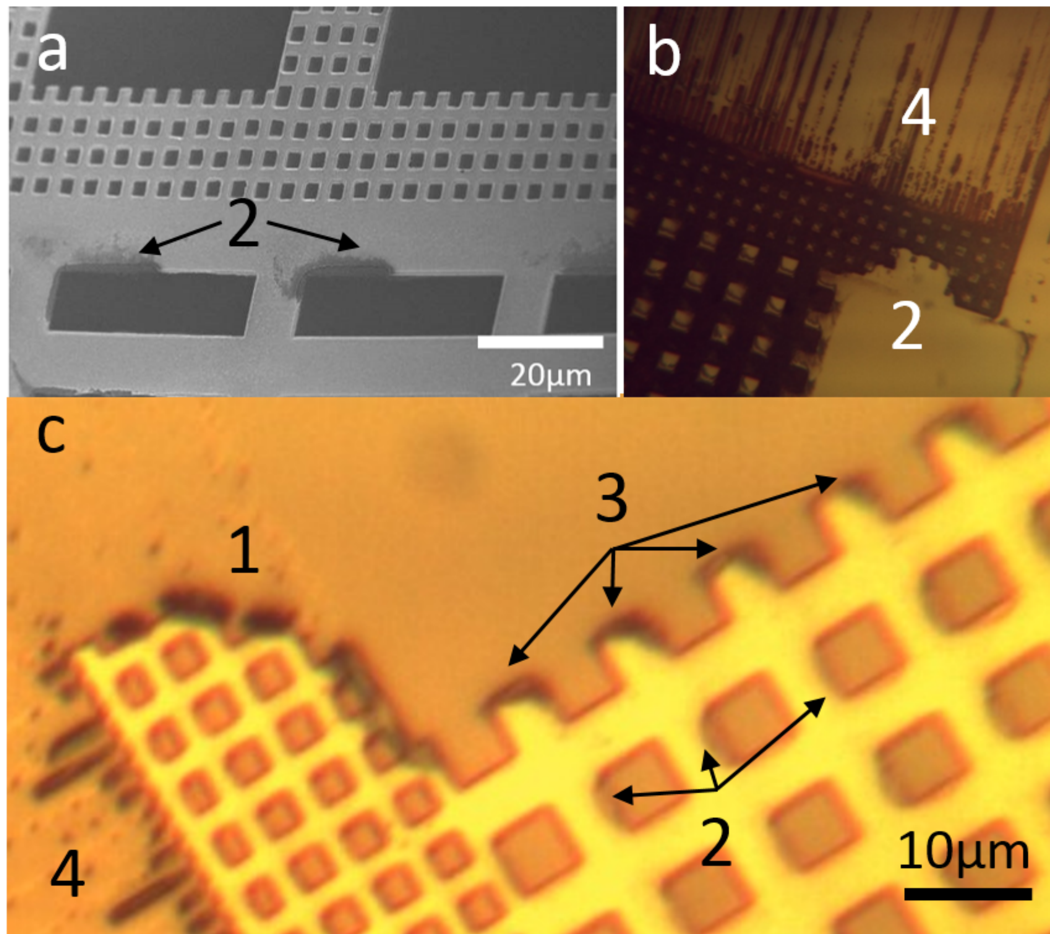

Figure 3.14: Features created using the AMPT process demonstrate problems with premature drying in the same places predicted by the fill factor template parameter. Images include (a) SEM micrograph of silver ink on silicon, optical micrograph of copper ink on lithium niobate and (c) optical micrograph of silver ink on silicon.

Though the fill factor system is qualitative, it correctly identifies features that pattern poorly in the AMPT process. Several examples can be seen in Figure 3.14. Locations that fill poorly include channels perpendicular to the primary direction of ink flow through the template (1 and 2), wide channels closed on three sides (3) and narrow channels beyond a certain length (4).

In general, the fill factor parameter shows that areas of low flow should be modified in order to increase filling quality. For instance, square pegs are commonly used to keep wide contact pads from collapsing, but they are prone to poor patterning as seen in location (2) of Figure 3.14. The poor patterning observed on the upstream side of square pegs can be improved by replacing square pegs with round pegs. The improvement is shown in Figure 3.15.

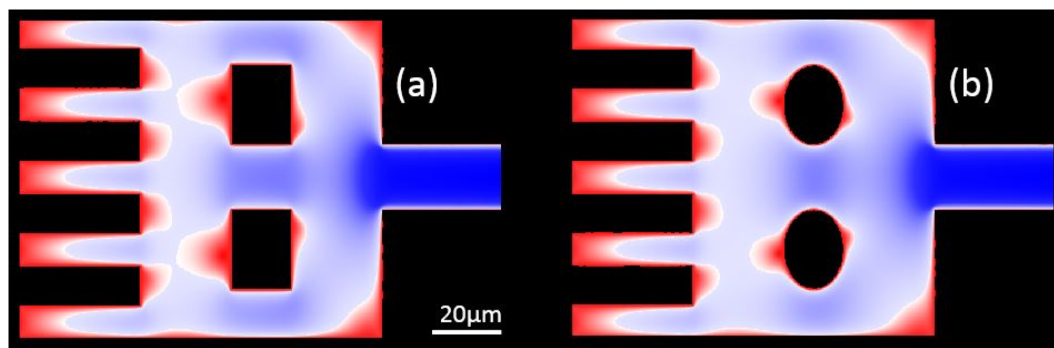

Figure 3.15: Comparison for a simplified contact pad with interdigitated fingers. Pad (a) contains square pegs that hold up the contact pad, with a large area of poor filling downstream (to the left) of the pegs. Pad (b) shows a proposed improvement to this design, evaluated using the fill factor model. The model shows better patterning on the downstream side.

3.4 Conclusions

This chapter demonstrated a model the filling of templates in the AMPT process. We presented a multi-part model designed to simplify finite element modeling for complex shapes of nanoparticle templates. Post-processing is applied to determine a flow factor that relates the fluid velocity through the channel to the absorptive flux through the walls of the vapor permeable template.

In order to construct this model, correlations between drying rate and the geometry of the patterned feature were established. As arrays of uniform features become more densely packed, the average flux through the channel walls decreases. The normalized average channel velocity scales quadratically with respect to the feature density. If arrays of channels have a uniform pitch and 50% packing density, but the aspect ratio changes, the flux through the walls increases as the channels become shorter relative to their width. The average velocity through such channels scales linearly with the fraction of channel wall surface area that is located on the top wall.

The model corresponds well to patterning limitations. Areas that pattern poorly include long, thin channels, and walls and corners on the upstream side of ink flow. Through trial

and error, templates can be optimized without fabrication. Creating a new template for AMPT can take weeks and cost thousands of dollars, so the ability to improve template design virtually is invaluable.

Chapter 4

AMPT Devices and Experimental Work

Chapters 2 and 3 discussed advancements in AMPT template fabrication, printing and modeling techniques. These improvements have all been necessary to fabricate complex, functional devices using the AMPT process. This chapter will discuss the design and results of a new AMPT-fabricated surface acoustic wave (SAW) resonator as a prof of concept for AMPT electrical device fabrication.

4.1 Surface Acoustic Wave Resonators

SAW resonators are perfect for low-cost electrical filters. Because the frequency of a SAW device depends only on the pitch of the IDTs, it is possible to print several SAW devices with different frequencies on the same substrate. This is advantageous in applications such as cell phones, when many resonators of different frequencies are needed in a low-size and low-cost package.

Current cellular phones require electrical resonators to filter frequencies around 2.4GHz [115]. For a SAW resonator on a commercially viable substrate, these frequencies can only be achieved when the electrode features approach 100nm in width. This exceeds the commercially viable limits of lift-off lithography (between 250nm and 1μm)[7]. Increasing the frequency requires either the use of higher harmonic frequencies or exotic substrates such as diamond, which are limited by issues of efficiency and cost, respectively. However, if the resolution of an inexpensive SAW resonator could be improved, they would be a viable option for cell phones and other telemetry systems once again.

AMPT is a promising approach for fabricating SAW waves. Modern cell phones use FBAR filters, which use bulk acoustic resonance through thin films to achieve frequencies that would be too high for lithographically-patterned SAW resonators. FBAR filters require precise bulk etching, and a separate patterning process for each resonator. If an AMPT resonator were to approach 2.4GHz, it would lower the fabrication cost of cell phone telemetry

because AMPT can cheaply fabricate features in the submicron range, even if the master must be fabricated by expensive methods such as electron beam lithography. The long, thin electrodes of a SAW resonator are ideal features to pattern using an AMPT process.

SAW Resonator Theory

Surface acoustic wave (SAW) resonators are transducers in which an AC electrical signal is coupled to a surface wave on a piezoelectric substrate by means of interdigited electrodes. If two interdigitated electrodes are interlaced, a signal may be coupled between the two electrically isolated electrodes at the resonance frequency. These electrode structures (shown in Figure 4.1) are commonly called interdigitated transducers or IDTs.

The frequency of a SAW device is determined by the pitch of the IDTs and the speed of sound in the substrate. The resonator's center frequency f_c is defined as

$$f_c = \frac{v}{2d} = \frac{v}{2(s+w)} \tag{4.1}$$

where v is the speed of sound along the surface of the substrate, d is the pitch of the electrodes w is the width of a single electrode, and s is the distance between the electrodes[116].

Y-Z cut lithium niobate was chosen as the substrate material for all SAW resonators in this paper. Lithium niobate is a common substrate for SAW resonators, most notably because of its high sound velocity and high electromechanical coupling coefficient (k^2). The high sound velocity enables a high frequency for a given IDT pitch size. The high electromagnetic coupling coefficient indicates a high amount of energy transferred from the electrical oscillations of the IDT, to the mechanical vibrations of the substrate, and back [117]. The electromagnetic coupling coefficient may be expressed as

$$k^2 = \frac{\text{Energy Converted}}{\text{Input Energy}} = \frac{v_0^2 - v_m^2}{v_0^2} \tag{4.2}$$

where v_0 is the surface velocity for lithium niobate in a vacuum, and v_m is the surface velocity for lithium niobate covered in a thin layer of conductive metal[117]. A material with a high electromagnetic coupling coefficient leads to a SAW resonator with narrow filter bandwidth and a low insertion loss.

Y-Z cut lithium niobate has a v_0 of 3488m/s and a v_m of 3411m/s, giving $k^2 = 4.4\%$ [118].

SAW Resonator Design

SAW resonators were fabricated in two phases. The first phase contained three different types of 1μm pitch SAW-based electrical devices. The second contained only one-port resonators ranging in size from 500nm to 1μm in pitch. Both designs have many design commonalities, as described below.

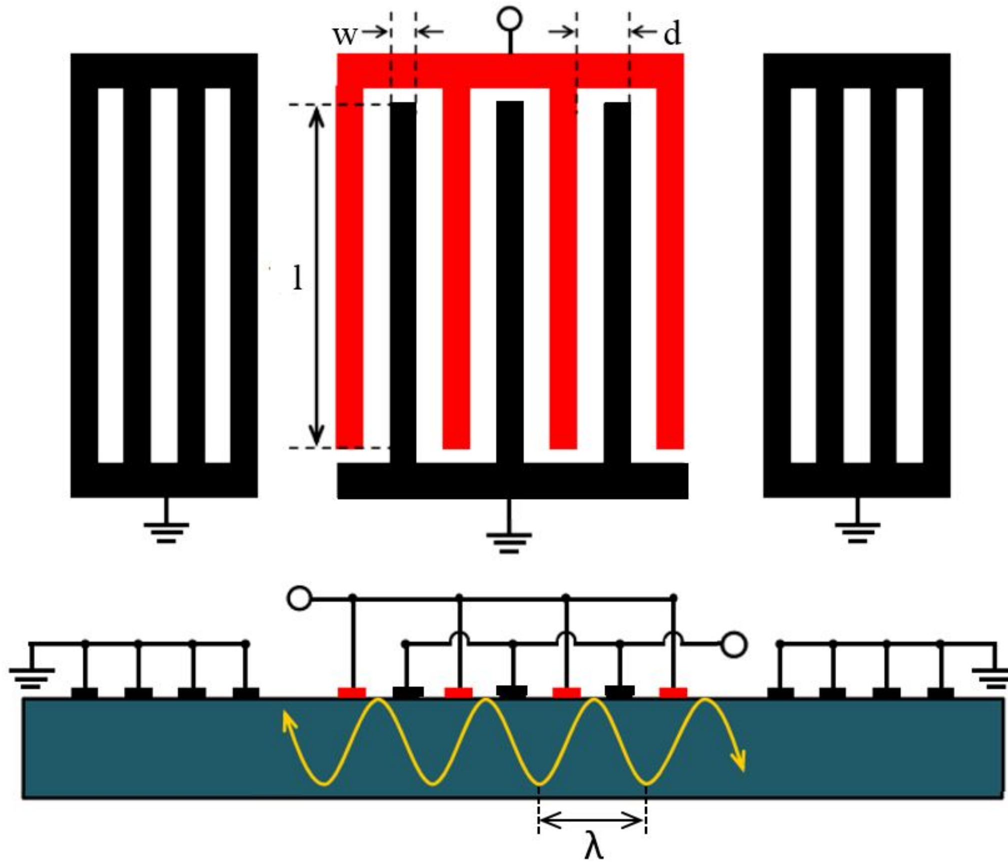

Figure 4.1: Layout of an one-port SAW resonator. An RF signal is fed into an input set of electrodes (shown in red) that are interdigitated with a grounded electrode. The electric field in the vicinity of these electrodes causes the piezoelectric substrate below to expand and contract, creating a moving surface wave. The wave is constrained by an array of reflection gratings (shown in black) along either side of the resonator. The wavelength (λ) is proportional to the pitch (d) of the IDTs.

GSG Pads

A ground-source-ground (GSG) probe is typical for RF interrogation of a resonator. Proper measurements require pads that match the probe layout. The GSG pads for the SAW design were 80μm by 120μm for the center source pad, and 203.5μm by 120μm for the ground pads on either side. The pads were spaced 50μm apart. The GSG pads contained holes spaced throughout. These holes resulted from pillars that were used in the AMPT template to keep the PMP from collapsing under the evaporation-driven pressure gradient.

Waveguide and Reflection Grating

Each resonator had an IDT and two waveguides on either side. The IDT had 80 lines. Each IDT had an alternating pattern of long 130μm lines and short 8μm lines. Long lines terminated with a 2μm gap from a short line of the opposite side. The surface wave was excited in the 120μm where the RF and ground electrodes overlap, while the wave could dissipate in the 10μm on either side. This layout suppressed higher order diffracted transverse modes from reflecting back into the IDT.

Waves were contained on either side of the IDT by reflection gratings, consisting of 80 140μm-long lines. These gratings were designed to reflect surface waves back at Bragg condition intervals, further improving the efficiency of the resonator.

Resonator Phase 1

The first phase of AMPT SAW resonators attempted to create a variety of SAW devices using a single-layer master. Wafers were fabricated using an ASML 5500/300 DUV stepper. The minimum feature size fabricated was 1μm. After lithographic patterning, features were etched using two different approaches of deep reactive ion etching. A first attempt used silicon wafers, while a second approach used a thermally grown layer of SiO_2. Both methods are discussed in Chapter 2.

These layouts had a tendency to print poorly. Several features suffered from premature drying in the patterning step, particularly on long, thin channels. Features also patterned poorly due to fill channels with low aspect ratios. These channels had a tendency to dry too quickly or collapse under pressure and block off flow.

Device Variants

The ASML 5500/300 DUV stepper masks can contain four different die layouts. This enabled experimentation with different SAW devices. Phase 1 included three different layouts.

One-Port Resonator The one-port resonator (Figure 4.2) was filled using three fill ports. With only one source pad, the resonator was designed to be used to measure admittance with respect to frequency. At the resonance frequency, the reflected signal drops in amplitude, as energy is transferred into the piezoelectric substrate. These devices were the simplest to fabricate, but the channels from the ground pads to the grounded side of the IDT frequently dried prematurely during patterning.

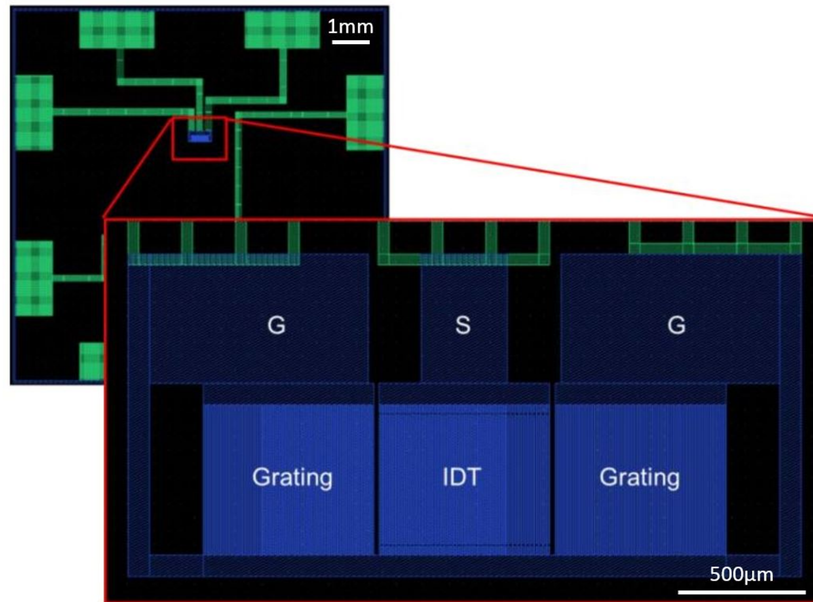

Figure 4.2: One-port SAW resonator design. This design is similar to that of the Phase 2 resonators. The resonator (light blue) uses a single GSG pad (dark blue) and requires three fill ports (green). Two of these fill ports fill the grounded reflection gratings on either side of the IDT that constraint the SAW gratings.

Two-Port Delay Line The two-port delay line (Figure 4.3) was filled using five fill ports. In standard operation, two port delay lines use one IDT for an input RF signal and one as an output signal. The input signal creates a moving wave at the resonant frequency that travels across the piezoelectric substrate and induces an RF signal of the same frequency in the output IDT. The signal is shifted by a phase that is proportional to the speed of sound in the material, and distance between the resonators.

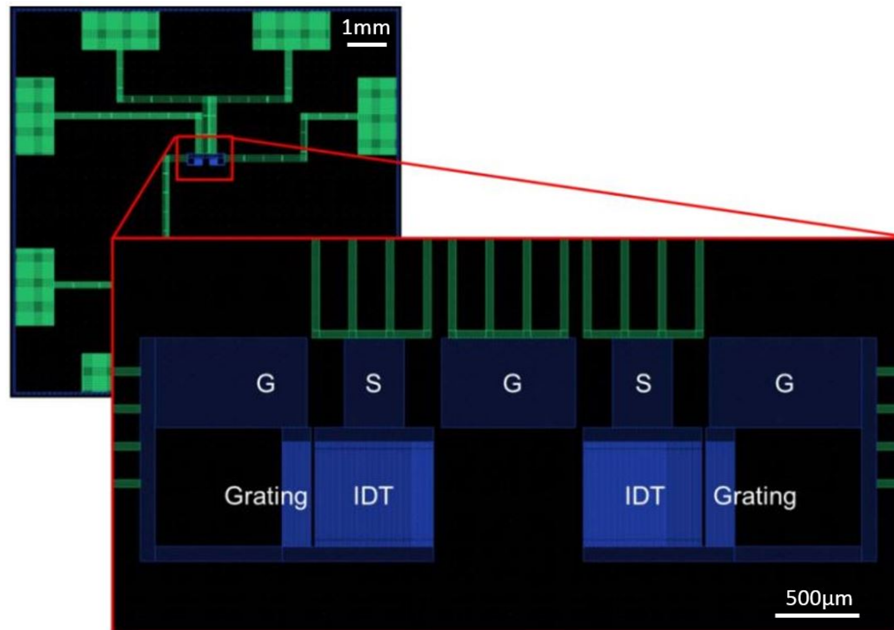

Figure 4.3: Two-port delay line design. The ladder filter uses two GSG pads, one for the input signal and one for the output signal. The design requires and requires five fill ports. The space between the IDTs determines the measured phase shift between the input and the output.

This device was designed to measure the transmission from one IDT to the other with respect to frequency. The delay line can be used as a measure of the co-alignment of the two IDTs. Even a slight difference in the angular orientation of the resonators would cause significant attenuation. Delay lines were also sensitive to slight distortions of the mask layout. The spacing between IDTs was 200μm, or 50 times the wavelength. A 2% distortion in size would create a 90° phase shift between the input and output IDTs. These devices also suffered from premature drying for the grounded side of the IDT.

Three Port Ladder Filter The 1.5 stage three-port ladder filter (Figure 4.4) was filled using five fill ports. It was the most ambitious of the attempted designs. It was designed to measure both transmission and reflection with respect to frequency. The goal of the ladder filter was to test the control of feature size control down to 10nm for an AMPT device. The bandwidth of the filter is determined by the difference in pitch between the f_s resonators and the $f_s - \Delta f$ resonators. In practice, these devices were particularly hard to fill, because the layout had three resonators connected to the same fill port by a narrow channel. The wire diagram for the ladder filter is shown in Figure 4.5.

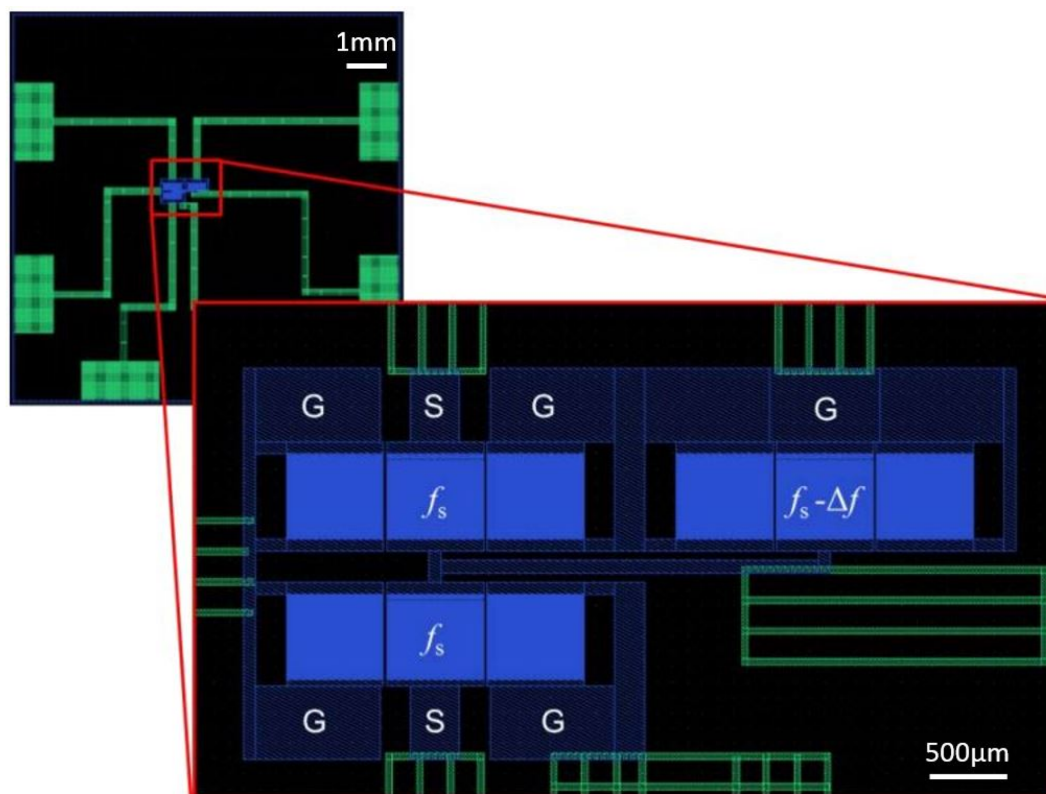

Figure 4.4: Three-port ladder filter. The filter contains three IDTs and requires six fill channels. Drying was particularly common in the line that connected the three IDTs. It was the most complex of the three Phase 1 designs. The electrical diagram for this filter is shown in Figure 4.5. The input voltage is read between the top left source and the common ground. The output voltage is read between the bottom left source and the common ground.

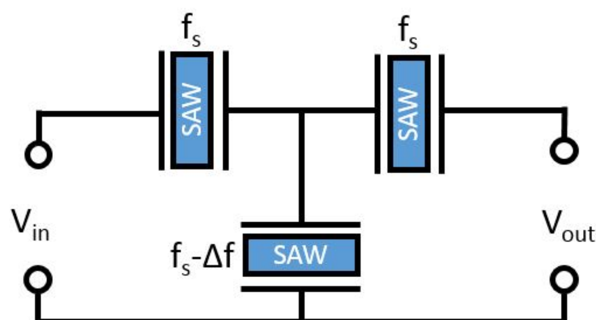

Figure 4.5: Schematic diagram for the circuit of the three-port SAW ladder filter. This diagram corresponds to the layout shown in Figure 4.4

Resonator Phase 2

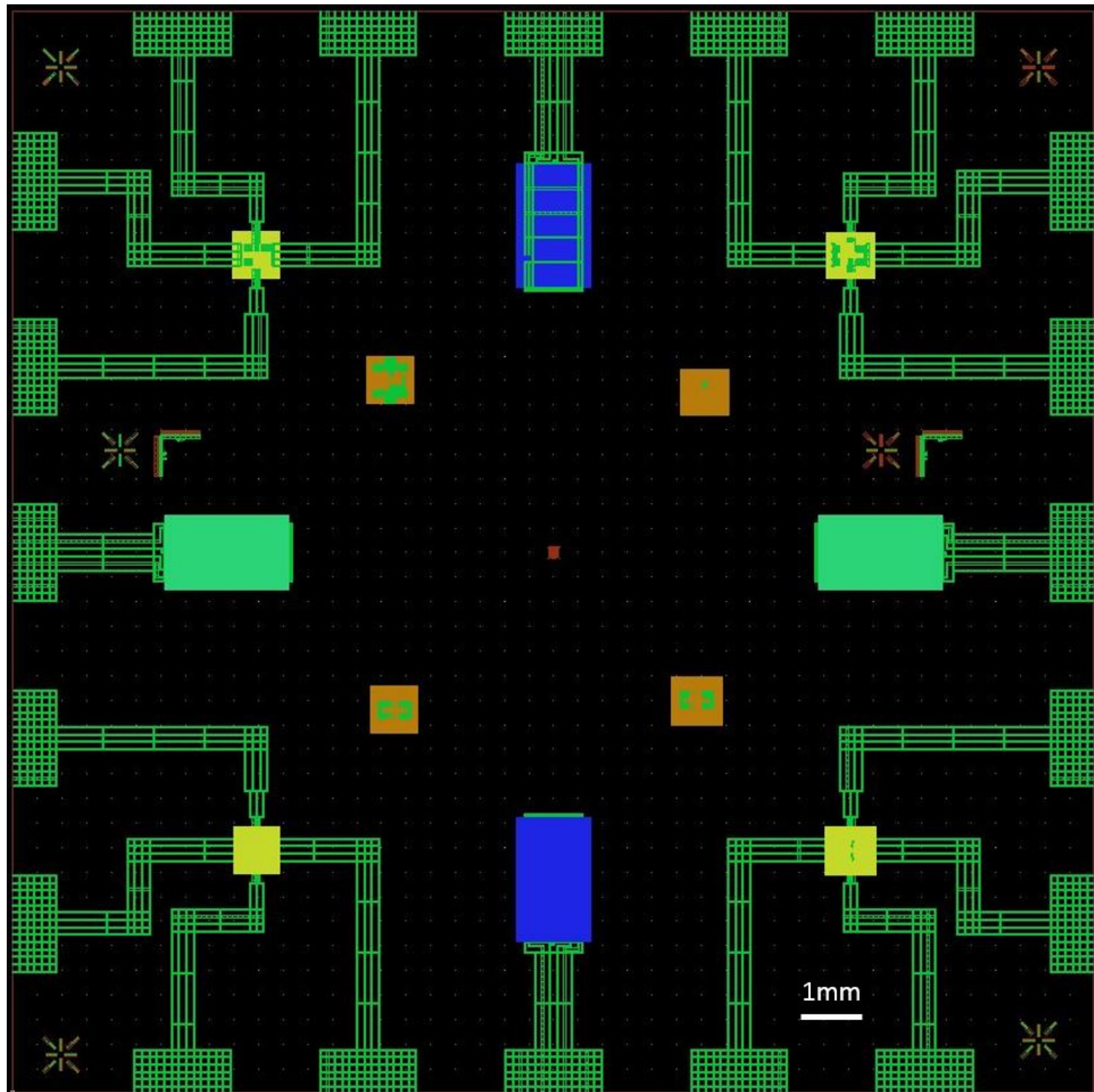

Figure 4.6: Layout for the Phase 2 mask. Green shows SU-8 features, yellow shows resonators filled by fill channels, orange shows top-loaded resonators, aqua shows test channels with a 1:1 channel-to-gap width ratio, blue shows test channels with a 1:2 channel-to-gap width ratio, and red shows SiO_2 alignment and test features.

Based on the incomplete patterning of features in Phase 1, Phase 2 sought to simplify resonator design down to one port, and to explore the possibility of SAW resonators with submicron resolution. These resonators were fabricated in conjunction with Fuji Electric, which manufactured the SiO_2 submicron layer using a NSR-2205i11D UV stepper with a

250nm resolution. Fill channels were fabricated out of SU-8 on SiO_2 channels using an EVG620 aligner with a 7in mask. Details for this fabrication process are discussed in Chapter 2.

Each mask of an NSR-2205i11D stepper creates a single 2.2cm by 2.2cm die. The increased size of these dies over those used in Phase 1 allowed the creation of many more features on a single die. Each die contained eight resonators and four sets of test arrays. Four of the resonators were designed to be filled by fill channels from the edges of the template, and four resonators toward the center of the template, that were designed to be filled through top-mounted fill ports. These top-loaded SAW resonators have not been tested, but their design is based on previous AMPT work[64]. The layout of Phase 2 resonators are shown in Figure 4.6.

The features for the Phase 2 die are listed below:

1-Port Resonators	**Test Line Structure 1x and 2x Pitch**
1μm	2μm
800nm	1.5μm
600nm	1.25μm
500nm	1μm
	800nm
	700nm
	600nm
	500nm
	400nm
	350nm

Table 4.1: Table of features in the Phase 2 die shown in Figure 4.6

Results

Silver one-port SAW electrodes, pads, and reflection gratings were patterned on a lithium niobate by AMPT. The resonators were tested using an Agilent E5071B network analyzer to measure reflectance with a GSG probe. The results were generally good, especially for the 1μm and 800nm features. Residual stress in the PMP films around the tall SU-8 features lifted the bottom of the template slightly and lead to some leakage near the SU-8 fill channel termini. Template damage caused some distortion, which had detrimental results for resonators below 800nm.

The frequencies shown in Figure 4.8 demonstrate a resonance peak for each of the resonators printed from a single AMPT template. The results show particularly good response for a 1μm pitch resonator (Q=13.4) and for a 800nm pitch resonator (Q=9.72). The smaller

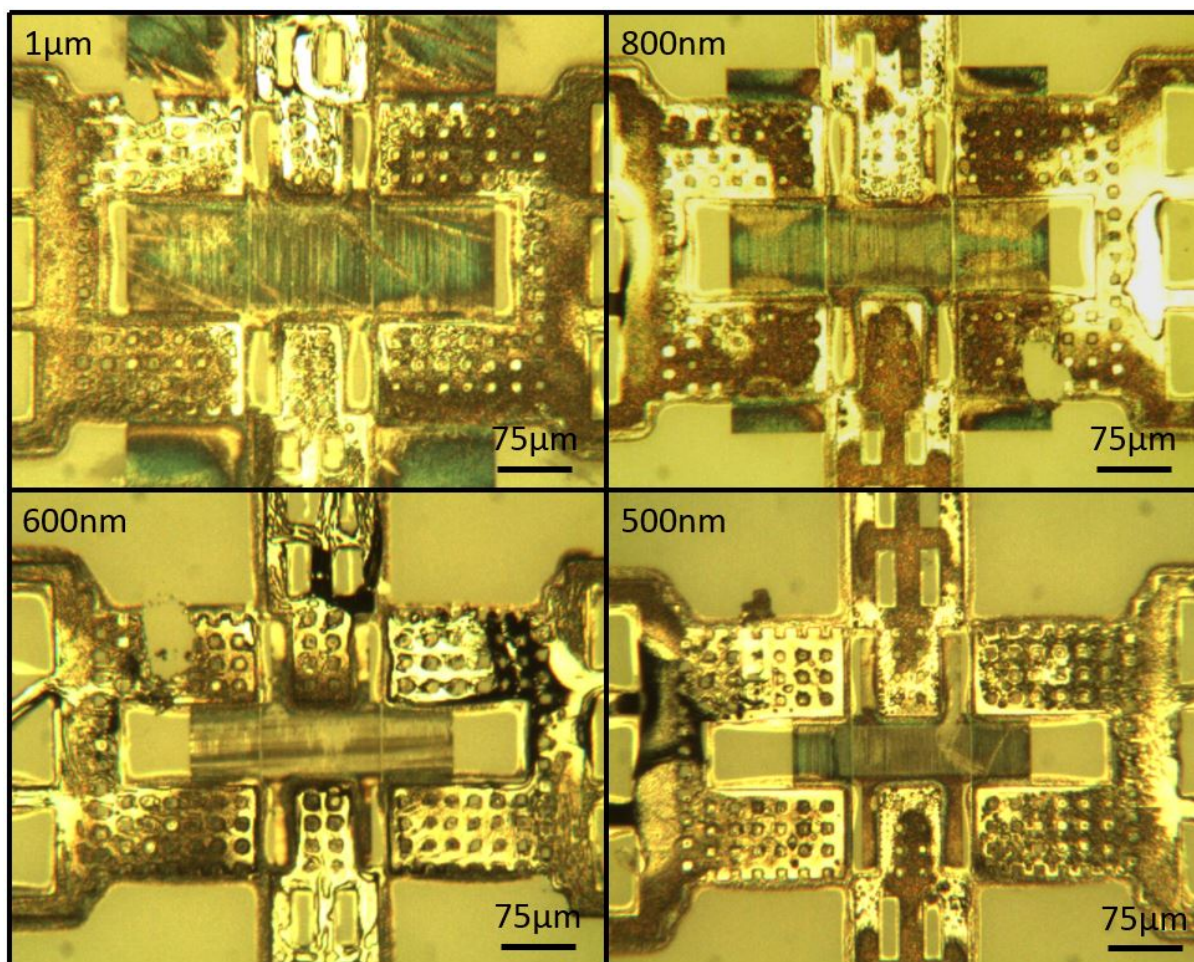

Figure 4.7: Images of AMPT-printed resonators ranging from 1μm 500nm. The results of these resonators are shown in Figure 4.8 and 4.9

resonators had lower quality factors (Q=4.51 and Q=5.91 for 600nm and 500nm resonators, respectively).

The resonant frequencies of the AMPT-patterned resonators stray somewhat from the theoretical resonance frequencies as derived in Equation 4.1. Resonance peaks deviated below predicted values for larger resonators and above predicted values for smaller resonators.

The deviations in frequencies may be due to wrinkling or warping, which can especially be seen in the 1μm and 500nm resonators. The wrinkling, along with more uniform forms of distortion may be due to some combination of template swelling and pressure-induced stretching.

Both PMP[77] and PDMS[119] swell about 10% when saturated with ethanol. However, the template is only saturated with solvent along the fill channel walls. The concentration of the ethanol drops as the distance from the fill channel increases. The exact concentration

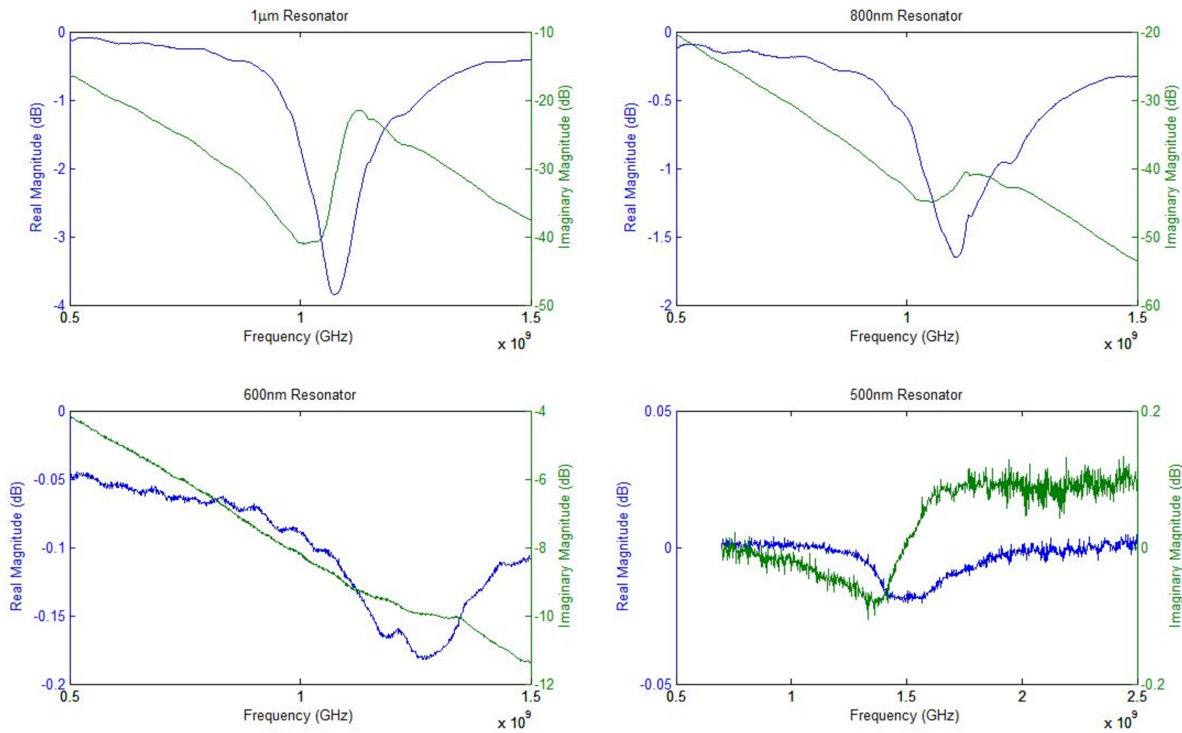

Figure 4.8: Frequency response for four silver resonators printed simultaneously from a single AMPT template on a lithium niobate substrate.

profile depends on the aspect ratio of the channels, as can be deduced from Figure 3.9. It is possible that the low aspect ratio features of the smaller IDTs swell slightly more than the high aspect ratio, larger IDTs. However, this would account for no more than a 10% deviation.

Another possibility is that distortion occurred due to the compression of the PDMS. PDMS has a Poisson ratio of almost 0.5[120], meaning that is is essentially incompressible. During patterning, the PDMS is compressed roughly 30%, resulting in a 15% elongation along its axes. This stretching may warp the layout in different places.

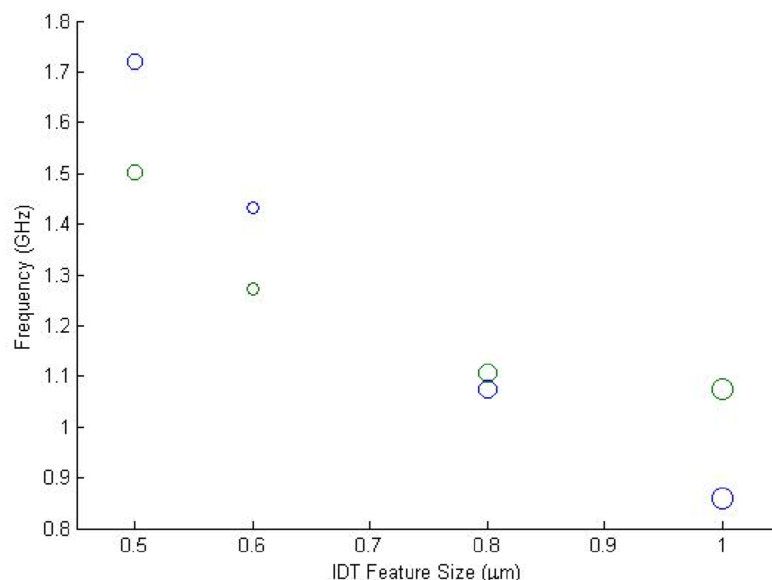

Figure 4.9: Plot of theoretical resonance frequency (blue) and experimental frequency (green) across the range of resonator features sizes. The size of the points show the relative quality factors of each printed resonator from Figure 4.8.

4.2 Semiconductor Concepts

The majority of research for an AMPT discussed in this dissertation pertains to the construction of SAW devices. SAW devices are easy to fabricate because they only require a single layer of patterned metal. These characteristics make SAW resonators well suited to the AMPT fabrication process in its current form. In order to become a truly versatile electronic printing method, AMPT must be able to pattern semiconductors as well as metals. There exist several options for patterning semiconductors with AMPT.

A first option is to use nanoparticles of a traditional semiconductor material. Zinc oxide has already been demonstrated as a patternable material for use in the AMPT process. Zinc oxide nanoparticles were deposited through a modified AMPT process to make isolated UV light sensors [65]. Zinc oxide can also be used to pattern traditional transistors if printed nanoparticles are annealed after patterning [121]. These particles can be sintered at temperatures above 600°C to form continuous pathways for current flow between isolated particles. This technique may be possible for other lower-bandgap II-VI semiconductors such as CdS, CdSe and CdTe [122].

Two-dimensional semiconductor nanoflakes have been of increasing interest in the semiconductor community as an option for solvent-processed semiconductors [123]. AMPT patterning was attempted for two nanoflake semiconductors: MoS_2, and WS_2. Unfortunately,

the behavior of solvent-cast nanoflakes depends heavily on the thickness of the nanoflake layer. As the number of nanoflake layers increases from one to four or five, nanoflake bandgaps change from direct to indirect[124]. The height of the bandgap changes as well. These changes make nanoflakes a poor choice for AMPT patterning.

A final option of printed semiconductor is the use of printed silicon. Doped silicon, already the standard for traditionally-fabricated semiconductors, is becoming a more popular printed material. The primary limitation is the dense packing of doped silicon nanoparticles necessary to create structures that carry charge. Work has already begun on this in both an academic setting [125], and from industrial ink providers such as Intrinsiq. The primary limitation of silicon is to get sufficient charge transport between particles. Through close packing, thermal annealing and laser annealing, it is possible to bring conductivity up as high as $5\Omega^{-1}\text{cm}^{-1}$ [126], though this is still an order of magnitude below the conductivity of bulk doped silicon.

P3HT

Another option for an AMPT semiconductor is the use of an organic semiconductor. Organic semiconductors have gained popularity in academic research because they can be dissolved in a variety of organic solvents and printed without determent to their electrical properties[32][36]. Organic polymers generally conduct due to their overlapping π-orbitals.

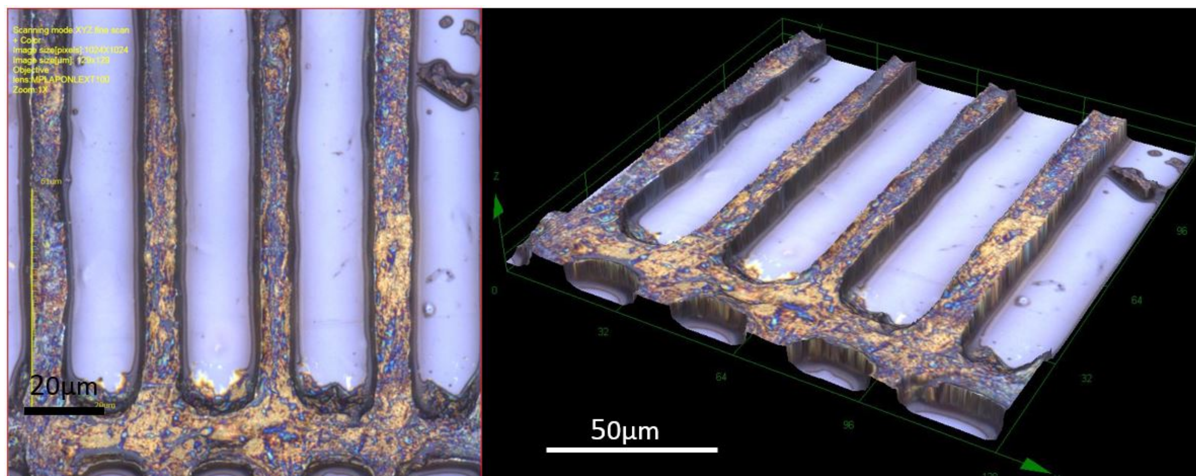

Figure 4.10: Laser-confocal image of AMPT-patterned P3HT. The distortion from the rigid sidewalls usually seen in AMPT is a result of the toluene of the P3HT solution swelling the PDMS.

The AMPT patterning of conductive polymers was first proposed by Demko[64] as an impetus for the fabrication of polymers using the technique. For this dissertation, the fabrication of conductive polymer patterns was attempted. Patterns were printed using 1% P3HT

in toluene solution. P3HT is a polymerized thiophene commonly used in printed electronics research[127]. P3HT is generally insulating, but the introduction of a dopant, such as iodine or bromine injects electrons or holes into the π orbitals[128]. Depending on the percentage of charged units along the polymer chain, the bandgap can be changed from 2.2 to 1.85[129].

For the purposes of patterning, P3HT was patterned in PDMS templates with 10μm channel width. The printed features can be seen in Figure 4.10. Results showed the feasibility of P3HT patterning, though quality was limited because the toluene used as a priming solvent and ink solvent swelled the template to the point that maintaining uniform pressure between the template and the substrate was impossible. Better results could be obtained by changing the solvent to one that swells less (e.g. tetrahydrofuran) and/or changing the template material to Teflon AF.

Nanodiamond Semiconductors

Diamond is an unusual choice for a semiconductor. Diamond has an extremely high band gap of 5.5eV[130]. However, recent years have brought increasing research in surface-conducting hydrogenated diamond surfaces. If enough hydrogen is chemisorbed to the surface, the diamond surface begins to exchange electrons with atmospheric water vapor. Atmospheric ions deplete surface electrons through the redox relationship [131].

$$2H_3O^+ + 2e^- \rightleftharpoons H_2 + 2H_2O \tag{4.3}$$

This electron transfer can generate a hole accumulation layer up to 30nm below the surface layer of the diamond [131]. Surface-doped diamond research has generally focused on diamond thin films, however, diamond nanoparticles can also become surface doped because of their high surface area-to-volume ratio. Figure 4.11 shows the current-voltage characteristics of a hydrazine-doped transistor. Detonation diamond nanoparticles, 2-10nm in diameter in HCl solution[132] were drop-cast onto a die with a source, a gate and a drain. The diamond structures were then exposed to hydrazine vapor for 30 minutes, doping the surface of the particles with hydrogen.

The nanodiamond transistors were short-lived. After roughly 30 minutes in atmosphere, their effects began to degrade significantly. However, hydrogen doping with a longer lifespan could be done using ultra-high vacuum annealing [131] or plasma treatment. Since the nanodiamonds are easily patterned through the AMPT process, this approach shows great progress towards a hydrogen-doped nanodiamond transistor.

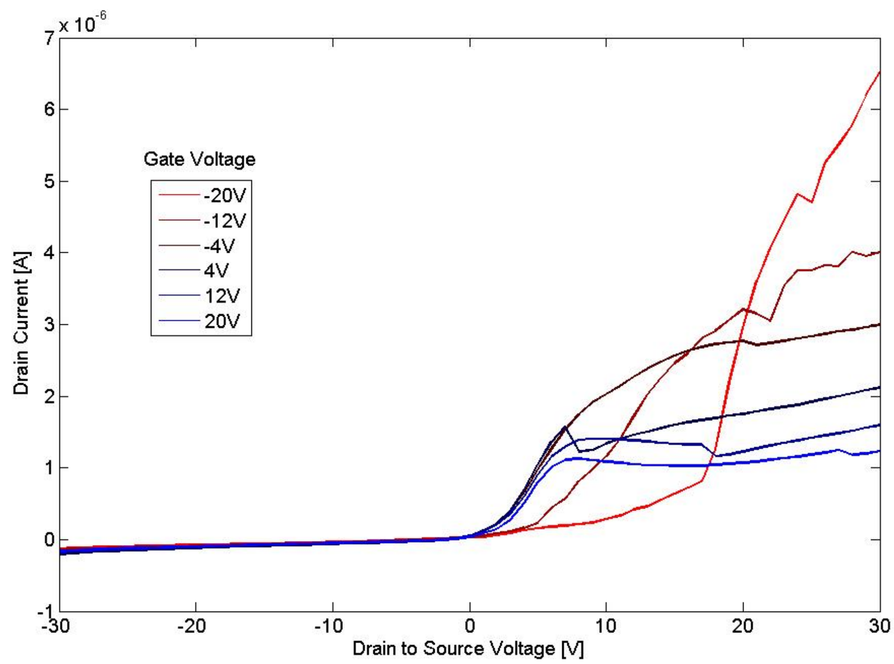

Figure 4.11: Current-voltage characteristics for a drop-cast diamond transistor

Chapter 5

Laser-Induced Direct Ablative Rapid Transport

Up to this point, this dissertation has focused on the AMPT process: a microfluidic process for closely-packing nanoparticles into vapor permeable templates for high-resolution, high-fidelity patterns. As demonstrated, the AMPT process has many benefits, but as a microfluidic process, its applications are limited in terms of both patterning throughput and the range of viable layouts. Laser-induced direct ablative rapid transport, or LIDART, was created in an attempt to expand the space of templated nanopatterning to non-microfludic processes. The result is a promising method for high-speed patterning of sintered metal nanoparticles onto flexible substrates.

5.1 The Need for Faster Fabrication and Isolated Features

The key to any templated patterning method capable of patterning isolated features quickly is a template that can be loaded from the top without the need for fill ports. This is how both lift-off and screen-printing work. In both cases, the ink is loaded through the top of the template and transferred directly onto the substrate. In lift off, the template is eventually dissolved, while in silkscreen, a flexible template is used that can be removed while the nanoparticle paste is still wet.

In a dry-patterned method along the lines of silkscreen, gravure, or liftoff, ink would loaded into the top of a template, then dried, sintered, and transferred onto the substrate. The crux of such an approach has been how to transfer dry patterns from the template onto the substrate.

LIDART uses a laser to transfer dry patterns. This makes it similar to the laser patterning methods like those discussed in Chapter 1. The laser transfer methods in Chapter 1 use the shape of a laser beam to define the shape of a patterned feature. In contrast, LIDART uses a template to define the shape of the nanoparticles before sintering and transferring with a

scanning laser beam. The nanoparticles are patterned by means of surface energy differences in the template.

5.2 Selective Surface Energy Patterning Theory

In selective surface energy patterning, a meniscus of liquid is dragged over a patterned surface, so that the liquid wets some areas of the surface but not others. Surface energy patterning depends on the difference in contact angle between the hydrophilic surface and the hydrophobic surface.

The wetting of surfaces in selective surface energy patterning is described in terms of contact angle. The contact angle is the angle between the air/liquid and solid/liquid interface of a small droplet resting on a surface, as shown in Figure 5.1. Contact angles are generally measured for water. Surfaces with a water contact angle of greater than 90° are considered hydrophobic, while surfaces with a contact angle less than that are hydrophilic. High energy surfaces such as metals and ceramics are generally hydrophilic, while low energy surfaces like polymers have higher contact angles. Fluoropolymers are generally hydrophobic[133]. Though the LIDART process does not use water as a solvent, the contact angle of any solvent can be estimated using the solvents relative polarity[134] shown in Table 5.2.

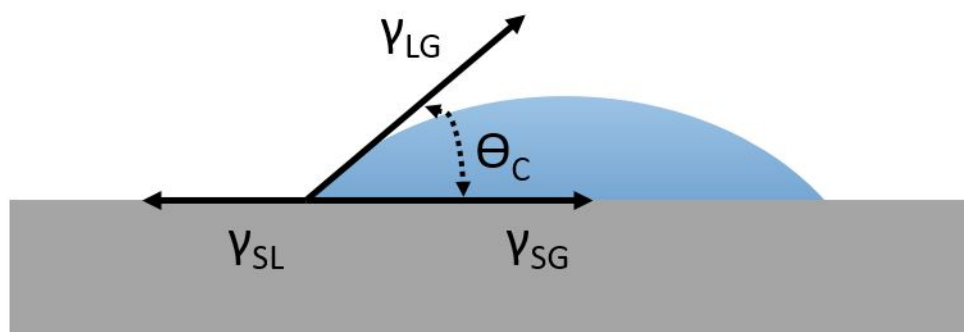

Figure 5.1: Diagram of the contact angle as a ratio as a balance of surface energies.

The contact angle on a smooth surface can be expressed as a balance of surface energies corresponding to interfacial surfaces

$$\gamma_{SG} + \gamma_{SL} + \gamma_{LG} cos(\Theta_C) \tag{5.1}$$

where γ_{sl}, γ_{sg}, γ_{lg}, is the surface energy of the solid/liquid, solid/gas and liquid/gas surfaces, respectively. The Young-Dupré equation creates a wetting parameter, S, which

determines the extent of spreading on a surface. The equation is based on the condition that complete wetting of a surface occurs when

$$\gamma_{SG} > \gamma_{SL} + \gamma_{LG} \tag{5.2}$$

which, combined with Equation 5.1 gives an expression for wetting such that

$$S = \gamma_{LG}(cos(\Theta) - 1) \tag{5.3}$$

where γ_{LG} is the surface tension listed in Table 5.2. Since a large portion of surface tension is caused by polarity, good inks for LIDART are usually polar solvents.

The roughness of a surface can change the contact angle of a material. There are three potential wetting states that a droplet can have on a rough surface shown in Figure 5.2 [135]. The first is the Cassie air trapping state, in which the droplet is suspended on the tops of micro-scale asperities. This added air/water interface increases the effective contact angle of the droplet. The modified contact angle, Θ^* becomes

$$cos(\Theta^*) = -1 + f_s(cos\Theta + 1) \tag{5.4}$$

where f_s the fraction of the surface on which the droplet touches the surface. The Cassie air trapping state makes it impossible to pattern features for the LIDART process, since ink can roll over hydrophilic wells. The Wenzel state, when the ink penetrates into the wells, becomes energetically favorable when the roughness becomes sufficiently high, or when

$$r_f > \frac{cos\Theta^*_{Cassie}}{cos\Theta} \tag{5.5}$$

This result shows a counter-intuitive limit for LIDART; if the feature size of the template becomes too small, or the CYTOP surface becomes too hydrophobic, it becomes possible for drops to be suspended above the hydrophilic glass wells. Once the droplet has penetrated the well, or entered the Wenzel state, it is relatively easy to reach the Cassie impregnating state by breaking the liquid meniscus that connects the impregnated well to the rest of the droplet. This is achieved through the use of a doctor blade at a low capillary number.

5.3 Overview of LIDART Process

The LIDART process uses laser-transport to move patterned material from the template and onto a substrate. The process is described in Figure 5.3. Nitrocellulose solution and nanoparticle ink are sequentially loaded into a template through the use of a doctor blade. The doctor blade is a metal bar held in close contact with the template (about 100μm off the surface), that drags a meniscus of ink or nitrocellulose along with it.

In the LIDART process, the laser performs three major functions

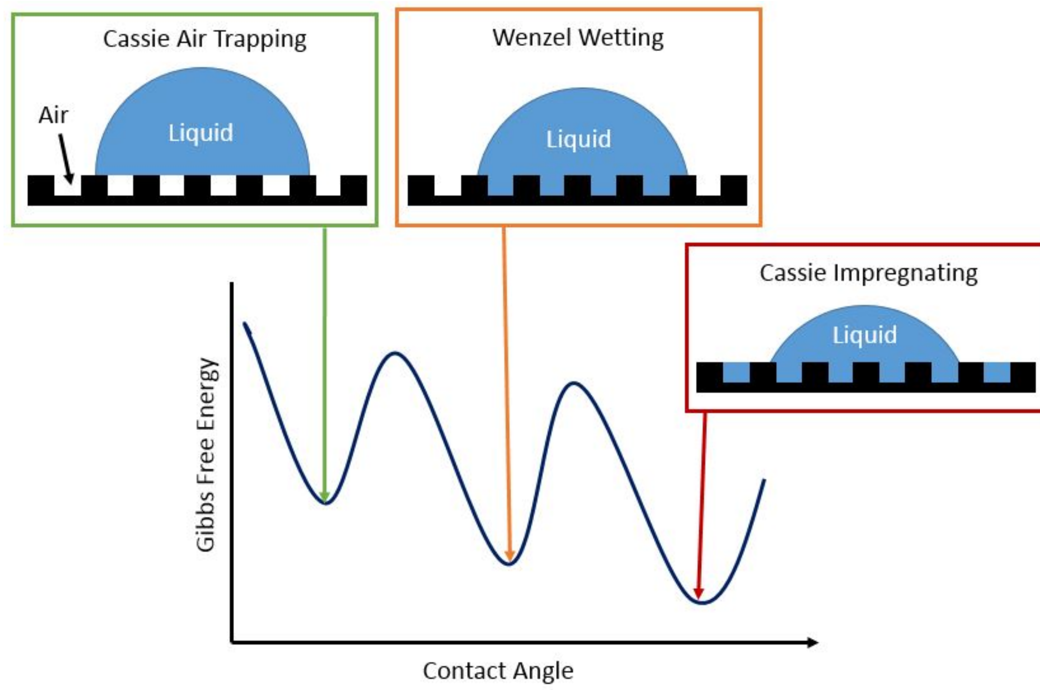

Figure 5.2: Diagram of the relative free energies for three different wetting domains. In the Cassie air trapping domain, a droplet is suspended over the surface of the template, making it impossible to pattern a feature. This can occur if the CYTOP is too hydrophobic or the feature is too small. From the Wenzel state, the Cassie impregnating state can be reached by stretching a drop with a doctor blade to break the meniscus. As shown in the energy plots, both the Cassie air trapping and the Wenzel state are metastable[135], though it is difficult to transition from Wenzel wetting to Cassie air trapping without electro-wetting or increasing atmospheric pressure. For this reason, templates must be designed to avoid the Cassie air trapping domain.

1. The laser sinters the nanoparticles by using a low-power continuous-wave beam. This allows the nanoparticle features to hold together during the transfer process from the template, onto the substrate.

2. A high-power pulse heats the metal until the nitrocellulose ignites, transferring the nanoparticles onto the substrate.

3. The second laser pulse also heats the metal features in order to improve adhesion, either temporarily melting the features, the substrate, or both.

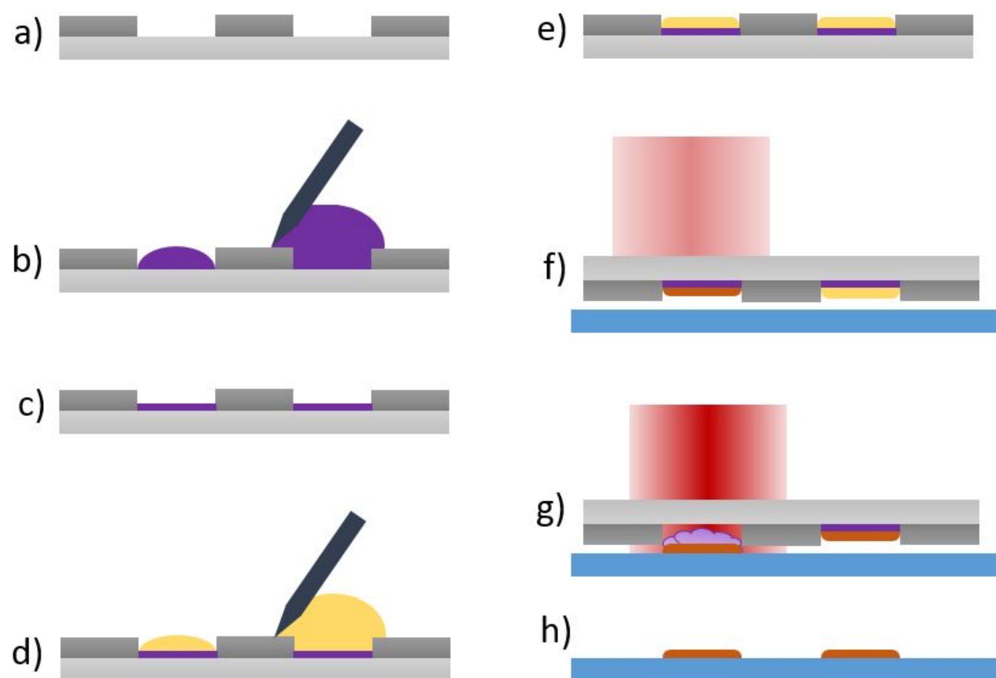

Figure 5.3: The LIDART patterning process. (a) A template of patterned, transparent, hydrophobic CYTOP fluoropolymer on a hydrophilic glass substrate is fabricated or cleaned. (b) Nitrocellulose solution is loaded into the template using a doctor blade. (c) The nitrocellulose solution is slowly dried, leaving a solid layer of nitrocellulose. (d) Nanoparticle ink is loaded into the template using a doctor blade. (e) The nanoparticle solution is dried, and brought into contact with a flexible substrate. (f) A low-power, continuous-wave laser is used to sinter the nanoparticle solution through the nitrocellulose without igniting the nitrocellulose. (g) A pulsed laser is used to heat the sintered metal until it ignites the nitrocellulose. (h) The template is removed, leaving sintered metal patterns on the substrate.

5.4 Template Fabrication

Templated patterning of nanoparticle ink is the key to the success of LIDART. The LIDART template must meet three key criteria. The first is that the template must contain hydrophobic and hydrophilic surfaces with as large a difference in contact angle between them as possible. Larger contact angles give higher resolution patterning of polar inks. A second key criterion is that a template must be transparent enough to a near-IR (1064nm) Nd:YAG laser that it does not become damaged during raster patterning. Finally, since the template size drives the feature size, the template must have a resolution of the smallest desired feature. To be compatative with the laser fabrication methods in Chapter 1, features must be smaller than 10μm. This section discusses the methods of achieving these

requirements.

CYTOP and Materials Selection

Glass is an obvious choice for a LIDART substrate because it is 93% optically clear in the near-IR range, and relatively inexpensive. Borosilicate glass has a particularly low thermal expansion constant, making it less susceptible to thermal shock. Finally, the contact angle of borosilicate glass is only 32°.

There are a variety of thin, patternable, hydrophobic, clear polymers that could be used as nitrocellulose layers, including SU-8, parylene C, and CYTOP. They are compared in Table 5.1.

Polymer	Contact Angle	NIR Transparency	Patterning Method
SU-8	81°[136]	95%[137]	Lithography
Parylene-C	87°[69]	70%[138]	Plasma Etching Lift-off
CYTOP	112°[139]	96%[139]	Plasma Etching Lift-off Hot Embossing

Table 5.1: Comparison of useful properties for a LIDART template materials. Lithography is the easiest and highest resolution patterning method. Plasma etching and hot embossing are two of the most complex patterning methods.

Based on Table 5.1, CYTOP fluoropolymer is the best choice for a hydrophobic material, even though it is more difficult to pattern than SU-8. In experimental testing, CYTOP holds up up significantly better to a high-power raster Nd:YAG laser pulse than SU-8.

CYTOP Patterning Techniques

CYTOP cannot be patterned directly through lithography, but it can be patterned through several methods, including plasma etching [140] [141], hot-embossing [142] [143], and lift-off [141] [144]. The simplest two of these methods, hot-embossing and lift-off, were tested.

Hot-Embossing

The resolution of hot embossing is primarily limited by the resolution of the master. Hot-embossing is more complex than lift-off, but it has been shown to make 1μm features (see Figure 5.7, bottom left). The process, which is shown on the left side of Figure 5.4 is as follows:

1. In the hot emboss process, (1a) 3mL of 5% CYTOP 809M is deposited on a clean borosilicate glass wafer, which is spun at 500rpm for 10 seconds followed by 900rpm for 20 seconds.

2. The wafer is soft baked at 75C for 5 minutes, then it is baked in a vacuum oven at 150C for 50 minutes in order to remove any solvent.

3. The CYTOP side of the wafer is placed face-down on a pre-patterned master. A flat PDMS block about 1.5" thick is placed on top of the glass wafer, and the whole setup is placed in a carver press.

4. The temperature is raised up to about 120°C, and the pressure is increased to about 2 tons for a 4-inch wafer (1b) and left to imprint for about 30 minutes.

5. The temperature is dropped to 45°C before the pressure is eased on the press.

6. The wafer is removed from the master (1c), but still has a film of CYTOP over printed features. This is removed using 300W O2 RIE with 60sccm of O2. The etching is done in 90 second increments until all the O2 is removed.

7. The wafer is baked at $170°C$ to anneal the CYTOP.

Lift-Off

An alternative process is shown on the right side of Figure 5.4. This method uses lift-off to pattern a thin layer of CYTOP.

1. A borosilicate wafer is cleaned, flooded hexamethyldisilazane (HMDS), then spun dry.

2. About 6mL of SPR 220-7 photoresist is deposited on the wafer, which is then spun at 1500rpm for 30 seconds.

3. The wafer is baked at 115°C for 90 seconds, leaving a roughly 10μm layer of resist on the wafer (2a).

4. The wafer is lithographically patterned with an exposure energy of 350MJ/cm^2.

5. The wafer is set aside for 30 minutes.

6. The wafer is baked for 90 seconds at 115°C.

7. The wafer is developed in MF-319 for about 20 mintues, until the exposed areas are fully removed (2b).

8. 5% CYTOP 809M is deposited on the wafer, which is spun at 500rpm for 10 seconds followed by 900rpm for 20 seconds (2c).

9. The wafer is baked at 150°C for 5 minutes.

10. The wafer is soaked in acetone until all of the features patterned on photoresist are removed (2d).

11. The wafer is baked at 170°C to anneal the CYTOP.

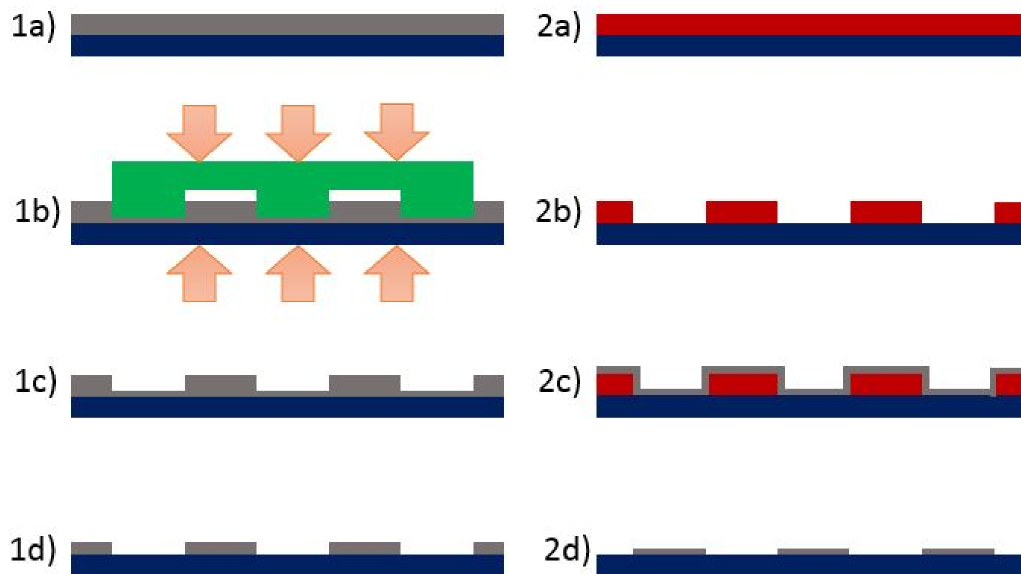

Figure 5.4: Overview of the hot-emboss process (left) and the lift-off process (right) for CYTOP patterning. The major steps of embossing are (1a) a wafer coated with CYTOP, (1b) embossing the CYTOP under heat and pressure, (1c) removing the wafer from the press and (1d) a finished wafer with the residual CYTOP layer removed by RIE. The major lift-off steps are (2a) a wafer with a layer of SPR 220-7 photoresist spun on and (2b) developed. CYTOP is then spun on (2c) and all remaining photoresist is developed (2d). In the image, glass is shown in blue, CYTOP is shown in gray, and SPR 220-7 is shown in red.

5.5 Propulsive Layer

Ablative materials have been used by a number of researches of laser transfer, as discussed in Section 1.2. An ablative layer allows greater flexibility in the material to be transported by the laser.

Several materials have been proposed for laser transfer propulsion. A good ablative material thermally decomposes to generate a large amount of gas. Of particular interest are nitrogen-based precursors (molecules containing asido, nitro, and triazole groups) that

produce N_2 gas when exposed to heat. Past laser ablative processes have used materials such as glycidyl azide polymer (GAP), poly[bis(azidomethyl)]oxetane (poly-BAMO) and polyvinylnitrate (PVN) [45]. Their structures are shown in Figure 5.5. A good ablative material must contain about 10% thermally available nitrogen by weight. Such a material must also be stable enough for safe handling, but propulsive in the temperature range that the laser can reach. Since the propellant layer is bordered by sintered nanoparticles on one side, and a the LIDART template on the other side, the material must require no oxygen for combustion.

Finally, in the case of the LIDART process, a laser-ablative material must be soluble in a polar solvent, but insoluble in alcohols, which are the most common nanoparticle ink solvent used for LIDART.

An alternative to an propulsive layer is the possibility of a delamination layer, that allows for the nanoparticle layer to break contact with template, but does not propel the nanoparticle layer with gas. Such a layer can temporarily melt, or break down by means of anaerobic pyrolysis, allowing the metal to adhere to the substrate. For the purposes of investigation in this research, LIDART was tested using caffeine and table sugar (examples of small molecules), cellulose acetate (an example of a polymer undergoing pyrolysis) and polyethylene glycol with an average molar weight of about 6000 (a water-soluble polymer with a high thermal mass but low melting temperature). Ultimately, none of these materials were effective at delaminating sintered nanoparticle structures.

Controlled substances such as poly-BAMO, GAP, and PVN were ruled out as options for LIDART propellant by virtue of their availability. AIBN, cast in both ethanol and acetone, did not easily delaminate nanoparticles. Nitrocellulose was ruled to be the most effective propellant layer.

Nitrocellulose Properties and Synthesis

Nitrocellulose has a number of properties that make it a good propellant layer. It is soluble in ketones, but only minimally soluble in alcohols. This allows it to remain intact during the nanoparticle coating step if the nanoparticle ink uses an alcohol solvent. Nitrocellulose is also transparent in the visible and near-IR spectrum. This allows the laser to pass through the nitrocellulose layer to sinter nanoparticles.

Nitrocellulose is notably easy to make, and its nitrogen content can be tailored during the synthesis process. All nitrocellulose for this work was synthesized by nitrating cotton fibers. Cotton consists of nearly-pure cellulose. If cellulose is soaked in sulphuric acid and nitric acid, the hydroxyl groups of the cellulose (located where the nitrate groups are found in the bottom right of Figure 5.5) are removed in a dehydration reaction

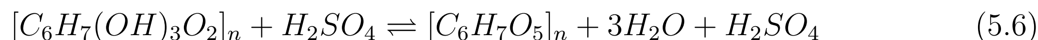

$$[C_6H_7(OH)_3O_2]_n + H_2SO_4 \rightleftharpoons [C_6H_7O_5]_n + 3H_2O + H_2SO_4 \quad (5.6)$$

The sulphuric acid also protonates the nitric acid, producing nitronium ions in the following reaction

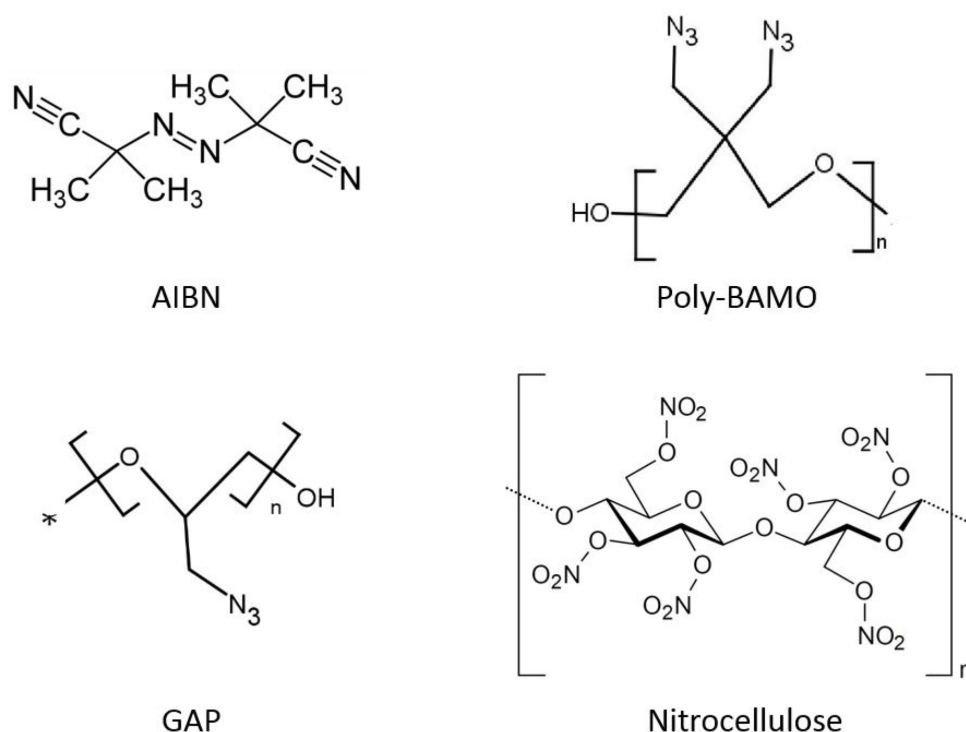

Figure 5.5: Popular nitrogen-rich polymers considered for LIDART, including (clockwise from top-left) azobisisobutyronitrile (AIBN), poly[bis(azidomethyl)]oxetane (poly-BAMO), nitrocellulose, and glycidyl azide polymer (GAP).

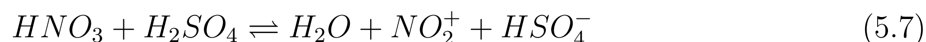

$$HNO_3 + H_2SO_4 \rightleftharpoons H_2O + NO_2^+ + HSO_4^- \tag{5.7}$$

These nitronium ions react with the dehydrated cellulose, creating nitrocellulose

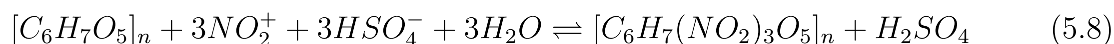

$$[C_6H_7O_5]_n + 3NO_2^+ + 3HSO_4^- + 3H_2O \rightleftharpoons [C_6H_7(NO_2)_3O_5]_n + H_2SO_4 \tag{5.8}$$

The above equations describe the synthesis of cellulose hexanitrate, an extremely explosive variant of nitrocellulose, in which all of the hydroxyl groups are nitrated (13.35% nitrogen by mass). Though cellulose hexanitrate is an effective rocket fuel, and generates a great deal of nitrogen, it is very unstable and must be kept in solution for safe keeping. The procedure for cellulose hexanitrate is in Appendix C.

After synthesis, nitrocellulose looks nearly identical to cotton. However, unlike cotton, nitrocellulose can be dissolved in ketones. Any insoluble impurities in the cotton can be filtered out of the nitrocellulose solution.

Nitrocellulose Ink Formulation

Nitrocellulose is soluble in both ketones and ethers. In order to pattern nitrocellulose on a surface-energy patterned substrate, the nitrocellulose must be dissolved in a polar solvent. Simple ketones are the best nitrocellulose solvents because they are relatively polar.

When properly solvent-cast, nitrocellulose creates a smooth, clear finish. However, creating a smooth nitrocellulose layer requires the slow evaporation of solvent. Acetone evaporates too quickly, causing the nitrocellulose to "blush", or turn cloudy due to microscopic bubbles. The evaporation rate can be slowed by using a heavier ketone. However, the polarity of the solvent drops off as the size of the ketone increases. The optimal compromise between polarity and volatility was found to be methyl isobutyl ketone (MIBK), which allowed for the casting of smooth nitrocellulose films without blushing. The saturation concentration of nitrocellulose in MIBK is roughly 5%.

5.6 Template Inking

The benefit of the LIDART process is the speed of cleaning and patterning templates. This speed is accomplished through the use of surface-energy patterning, in which the wettability difference between template surfaces is used to direct the wetting of polar inks away from CYTOP surfaces and into exposed glass wells. The quality of surface-energy patterning is controlled by three features: the polarity of the ink, the difference in contact angle between the CYTOP and exposed glass on the template, and the speed and height of a doctor blade used to push the ink across the template. This section will focus on the last of these components.

Ink Criteria

Surface energy-driven patterning occurs when a polar ink with a low capillary number is drawn slowly over a patterned surface. The capillary number of the ink is determined by the equation

$$Ca = \frac{\eta\nu}{\gamma} \tag{5.9}$$

which indicates that an ink must have a low viscosity (η), a slow blade coating speed (ν) and a high surface tension. Leading ink solvent candidates are given in Table 5.2.

Table 5.2 also includes the relative polarity, which is proportional to the driving force in surface energy patterning. Ideal inks must have a low capillary number and high polarity. Based on these results, 1-butanol was selected as the solvent for copper ink. Though dimethyl sulfoxide (DMSO) and acetone look like ideal solvents for nitrocellulose, they cause the nitrocellulose to blush upon drying, and were ruled out. Nitrocellulose solution can contain up to 50% alcohol, which could have raised the polarity of the nitrocellulose solution.

Solvent	Colloid/Solute	Rel. Polarity	Viscosity	Surface Tension
Ethylene Glycol	Copper	0.790	16.1 mPa·s	48.4 mN/m
1-Butanol	Copper	0.586	2.54mPa·s	26.3 mN/m
Diacetone Alcohol	Copper	0.312	2.79 mPa·s	30.9 mN/m
Ethyl Acetate	Copper	0.228	0.423 mPa·s	23.6 mN/m
Ethanol	Silver	0.654	1.07 mPa·s	22.1 mN/m
Acetone	Nitrocellulose	0.355	0.306 mPa·s	25.2 mN/m
Methyl Isobutyl Ketone	Nitrocellulose	0.228	0.58 mPa·s	23.6 mN/m
Dimethyl Sulfoxide	Nitrocellulose	0.444	1.99 mPa·s	43.0 mN/m

Table 5.2: Comparison of commercially available nanoparticle inks for use in the LIDART process [145]. These affect the capillary number in Equation 5.9

Unfortunately, though both methanol and butanol were tried as additives, both appeared to cause nitrocellulose blushing.

Doctor Blade and Rig

As the ink passes over hydrophobic features, it becomes pinned, and the meniscus is stretched. If the surface area to volume ratio becomes too large, the meniscus breaks, creating an isolated feature. The doctor blade is used to drag the meniscus and keep it as thin as possible so that it breaks easily. The capillary number measures the ease of breaking the meniscus.

The doctor blade used for all LIDART patterning was a MTI micrometer adjustable film applicator (EQ-Se-KTQ-50). This blade sat on top of the substrate, and uses two micrometers to adjust the height of the blade to within 10μm. The blade was generally run between 10μm and 100μm over the substrate. Though lower blade heights filled features better, higher blade heights deposited a thicker layer of ink or nitrocellulose into the wells. This presents a trade off. Proper laser ablation requires a high blade height, a concentrated ink, or both. Conversely, proper inking requires a low blade height and a dilute ink. Further testing is needed to determine how to optimise for the inking process.

Ink filling works best when the doctor blade moves at a constant, slow velocity. Slow speeds lower the capillary number, and a constant velocity stops the blade from moving up and down along the surface. The blade is driven by a rig shown in Figure 5.6. The rig uses a slowly turning threaded rod to move the doctor blade steadily along the substrate at speeds on the order of millimeters per second.

Inked samples are seen in Figure 5.7. Features as small as 1μm have been inked (The IDTs on the left of Figure 5.7), though templates with this resolution are difficult to manufacture by hot embossing without cracking under the emboss pressure..

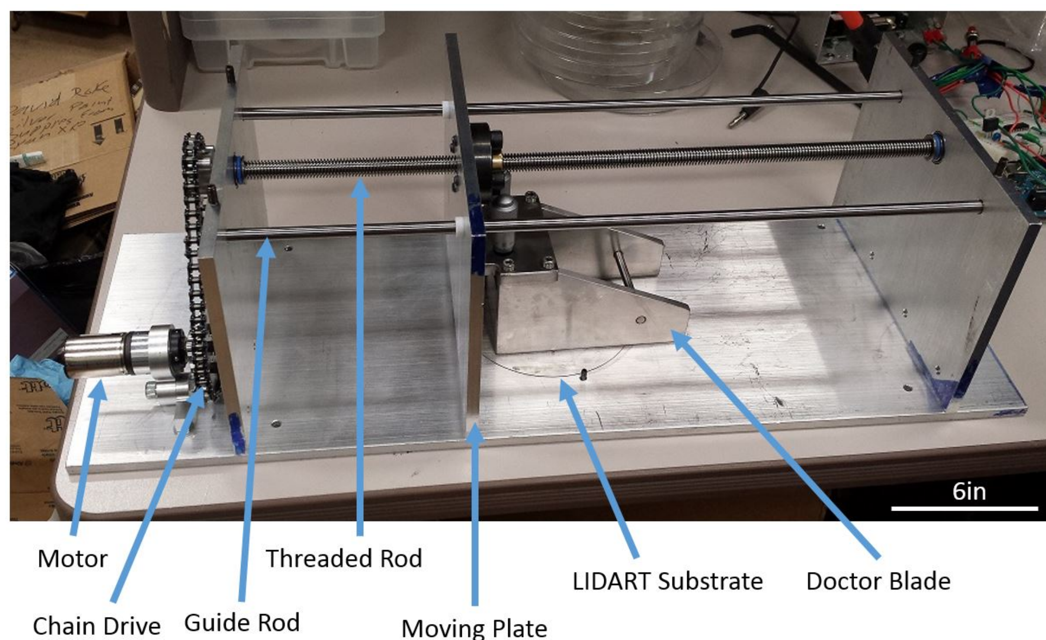

Figure 5.6: The doctor blade setup. A motor is linked by a chain to drive a threaded rod. The turning rod moves a plate, which pushes a doctor blade at a steady rate. The blade sits on top of the substrate on two skids. This keeps the blade at a constant height even if the substrate is uneven.

5.7 Flexible Substrate Selection

LIDART substrates must meet two key criteria. Firstly, they must be transparent enough to withstand laser ablation at 1064nm. Secondly, they must adhere sufficiently to the transferred sintered metal features, so that the features do not move after ablation or remain stuck to the template. Substrates are evaluated in Table 5.3

Proper adhesion requires either the melting of the metal or the substrate. If LIDART features are sintered before they are transferred, substrates with low glass transition temperatures are required. This is because the metal features are solid and have no mechanisms for adhesion by themselves.

Nanoparticles may be transferred above their melting temperature onto a substrate, at which point they can be remelted, sintered and smoothed. This approach has issues with the fidelity and conductivity of patterned features. Figure 5.8 shows examples of transferred copper nanoparticles that are sintered after transfer, and Figure 5.9 shows the fidelity limitation of transferring particles without sintering them. Transferring nanoparticles before they are sintered causes them to spray out into a collection of discrete, unconnected droplets, as shown in Figure 5.9.

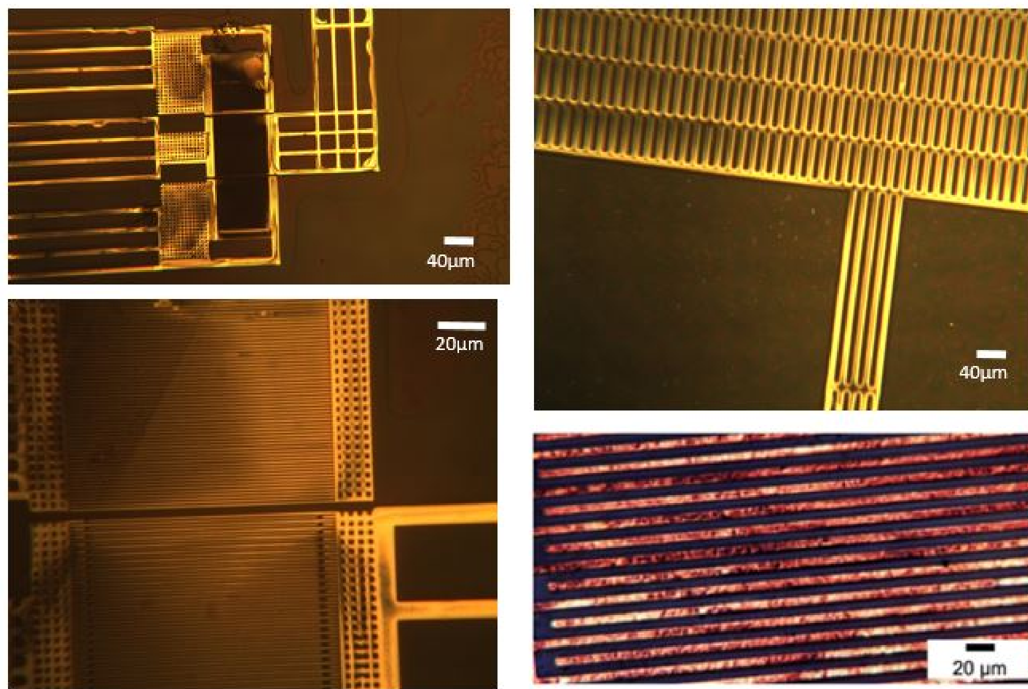

Figure 5.7: Examples of LIDART templates filled with copper (bottom-left) and silver (all other images) nanoparticles. The CYTOP on these samples were hot-embossed.

5.8 Laser Parameters

All laser processing was done with a single mode extended pulse control MOPA Nd:YAG fiber laser from SPI (EP-S 20 Watt G4). The laser was run in a raster configuration. The beam was positioned by a galvo-mirror and focused post-positioning by a 100mm f-theta lens. The focused beam size was roughly 15μm 1/e^2.

This laser has several key benefits. The galvo-mirror configuration allowed for fast scanning speeds, pattering 100mm^2 in about 5 minutes. The use of a MOPA (master oscillator power amplifier) laser means that the same laser may be run in pulsed and continuous wave modes. A higher power flash exposure system could potentially be used to speed up LIDART for high-throughput applications.

Laser parameters are presented for the sinter and transfer configurations in Table 5.4. It should be noted that the sinter step operates in a continuous wave mode, and the transfer step operates in a pulsed mode. In the pulsed laser signal is modulated by signal generator[146], while the laser pulse runs its full duration in the continuous wave mode [147]. Documentation on SPI continuous wave operation is sparse. Data in Table 5.4 is based off of data for pulsed operation. Continuous wave data is not available, but experimental results show that it has a higher average power, since it lacks modulation.

Material	Marking Test	Melting Point	Silver Adhesion
PTFE	None	327°C	Poor
Acrylic	Significant	132°C	N/A
TPX	Significant	240°C	Poor
COC	Mild	84°C	Good
Nylon	None	255°C	Poor
Laser Printer Paper	None	N/A	Fair
Polycarbonate	None	225°C	Good
Glass	None	1700°C	Fair

Table 5.3: A comparison of substrates tested for LIDART. The "marking test" is a measure of the discoloration of a material after being exposed to a 60W fiber laser. The adhesion measurement is a measure of the likelihood of silver adhering to the substrate rather than the template

Laser Parameter	Sinter	Transfer
Input Power	2W	20W
Frequency	15kHz	500kHz
Mark Speed	1000mm/s	1000mm/s
Mode	Continuous	Pulsed
Pulse Energy	0.053mJ	0.4mJ
10% Pulse Width	221ns	118ns
Typical Peak Power	1kW	10kW

Table 5.4: Laser parameters for sinter and transfer modes based on datasheets provided by SPI

Heat Transfer in Pulsed Laser Systems

In laser heating, the photons from a laser are partially absorbed by a material, exciting electrons in the material. When these electrons relax, they create lattice excitations or heat. For nanosecond or longer heat pulses, the electrons and the lattice are at thermal equilibrium at temperature, T. This is to say that the electron relaxation time is significantly shorter than the pulse duration of the laser. The transient temperature field is described by the classical heat conduction equation[148]

$$\rho C_p(T)\frac{\partial T}{\partial t} = \nabla \cdot (K(T)\nabla T) + Q_{ab}(x, y, z, t) \tag{5.10}$$

where ρ is the material density, C_p is the specific heat, K is the thermal conductivity and T is the temperature. Q_{ab} is the absorbed energy of the material.

From this equation, it is clear that longer-duration pulses allow heat to spread out along a material by means of conduction, while shorter duration pulses with the same power can

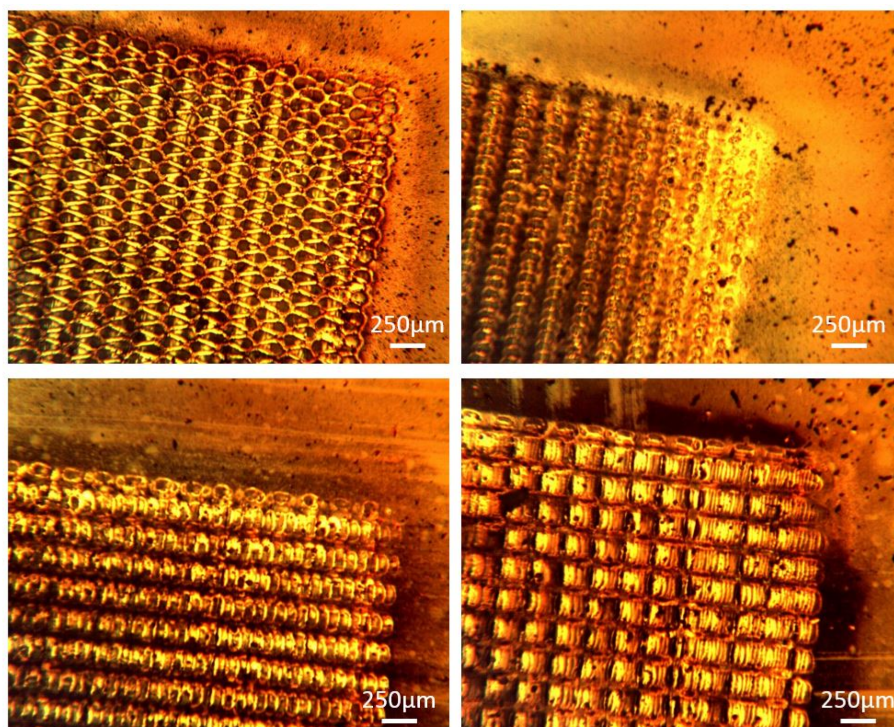

Figure 5.8: Examples of copper nanoparticles transferred onto a glass substrate. The particles are transferred at a high speed, then smoothed with a continuous wave, pulse width modulated laser. These features were not conductive, likely because of oxidation of the particles during the heated transfer step.

be used to concentrate heat briefly in a local area. This is the basis of the laser parameters used for LIDART. The slow, continuous wave lets heat spread through the nanoparticles slowly enough to sinter the nanoparticle layer without igniting the nitrocellulose layer. The high-speed pulses of the transfer step convey heat to only a small part of the nanoparticle layer, so that only the nitrocellulose in the immediate vicinity is ignited.

5.9 Results

LIDART shows promise as an inexpensive method of printing high quality components, especially on flexible substrates with low glass transition temperatures. Unlike other laser-transfer methods, the resolution of LIDART features does not depend on the quality of the laser used, and feature shape does not depend on aperture.

Conductivity was measured along thin LIDART-patterned strips. Since the LIDART process has no control over the height of the features, the unit Ω/square. The minimum resolution of LIDART features is roughly 10μm. Silver features patterned with a two step

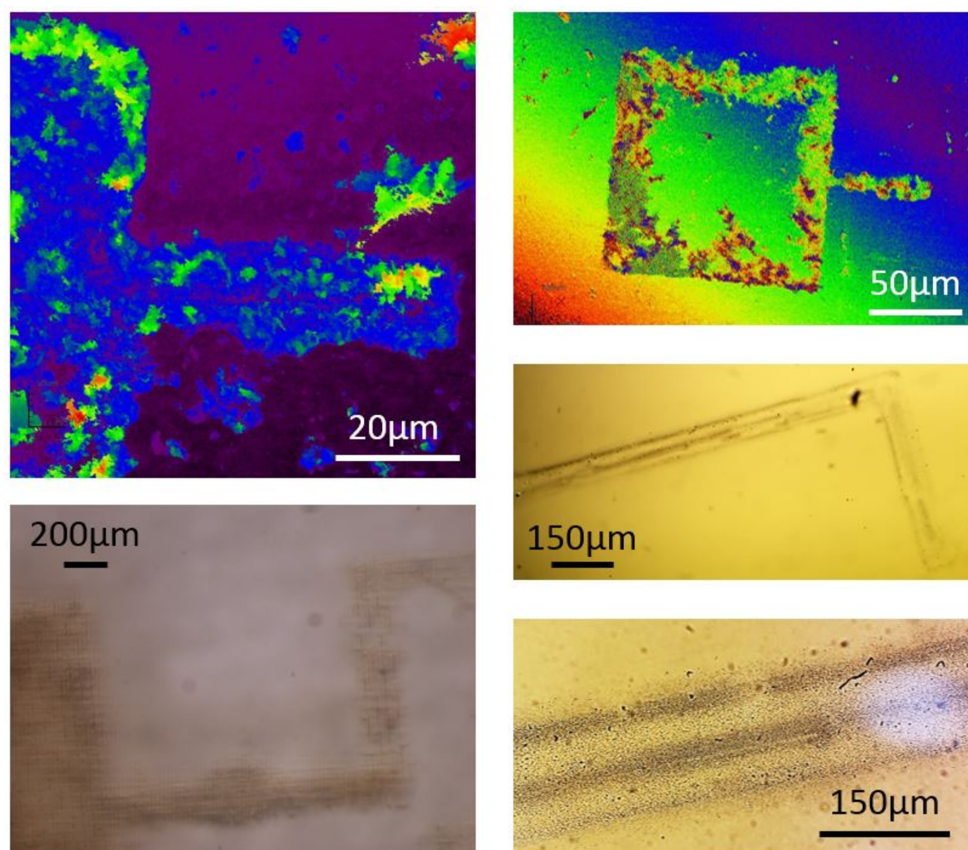

Figure 5.9: Examples of copper nanoparticles transferred without sintering onto metal (top, viewed with a confocal microscope) and glass (bottom). If the metal particles are not sintered, they spread before hitting the substrate.

sinter-transfer approach have a conductivity of 20-90Ω/square, depending on the substrate, thickness of silver and quality of transfer.

This section focuses on a few key limitations seen in LIDART that are fundamental to the process itself.

Resolution and Fidelity

Resolution in LIDART appears to be limited by the quality of template filling. A filled template must have a layer of nitrocellulose that is completely covered by a layer of metal nanoparticles. Figure 5.10 shows the ways that transfer can fail at small resolutions.

Though nanoparticles can be effectively patterned on substrates with a 1μm resolution (Figure 5.7, the nitrocellulose layer is more difficult to pattern because polymer solution viscosity increases quickly with higher polymer concentration, and because MIBK is a less polar solvent than ethanol or 1-butanol.

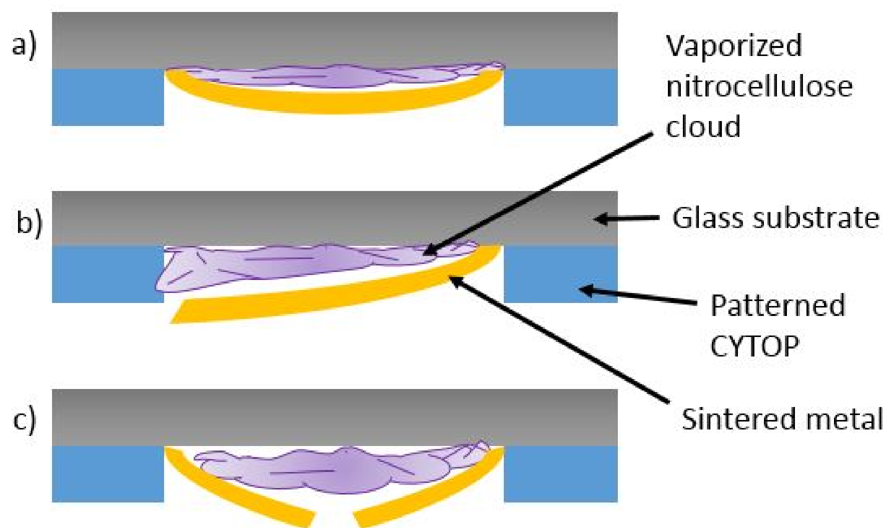

Figure 5.10: When the patterns become too small, features may not transfer due to (a) a nitrocellulose layer that is too small compared to the nanoparticle layer to cause delamination (b) an unevenly coated nitrocellulose or nanoparticle layer that stops the metal from delaminating on once side or (c) a nitrocellulose layer that is too large compared to the metal nanoparticle layer and rips the metal.

The quality of patterning appears to depend on the quality of the master. Imprinted masters were easier to ink, and had better laser transfer quality than lift-off masters. There are two possible reasons for this. One possibility is that lift-off masters had more ragged edges where the thin layer of spun-on CYTOP was sheared off. Another possibility is that the imprinted masters had thicker CYTOP layers, particularly at the edge of the exposed glass wells where imprinted CYTOP built up.

Features as small as 10μm can be patterned with approximately 20% regularity. Examples are shown in Figure 5.12 and Figure 5.11

Thermal Distortion

Thermal distortion is caused when the the thermal cycling of the laser warps the nanoparticle layer. When nanoparticles are exposed to the laser, they expand due to their rising temperature, and sinter together in this expanded state. After cooling, metal located directly under the center of the Gaussian shaped laser profile appears more stretched than metal that had been sintered by the lower-energy edge of the beam. The appearance, as seen in the left of Figure 5.11 is like a rubber band that has been stretched too far. The temporary expansion of the metal during the transfer step can also cause stress to build up in large sheets of sintered metal. This can cause the sintered metal sheet to tear, as seen on the right side of Figure 5.11

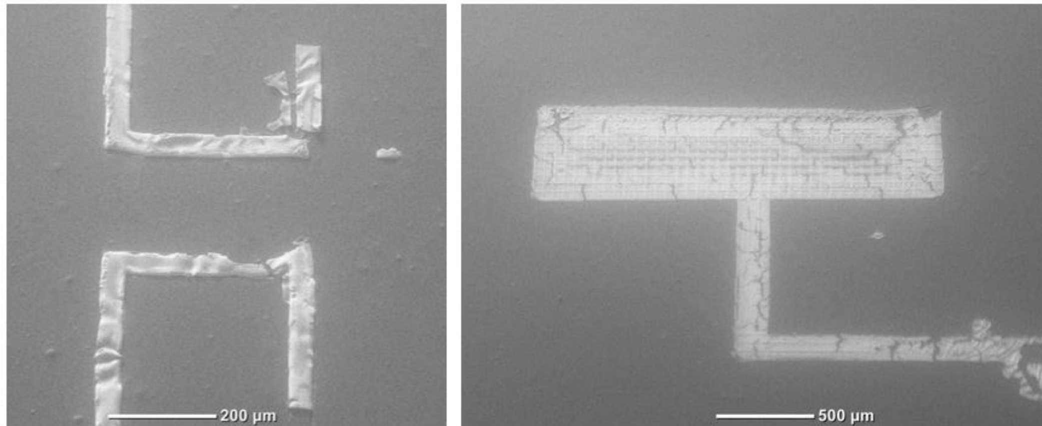

Figure 5.11: SEM images of transferred silver features on COC showing distortion due to different thermal loads. Thermal distortion can result in wrinkling (left) or tearing (right) of the metal features.

Coffee Ring Effect

The coffee ring effect, shown in Figure 1.5 and discussed in greater detail in Chapter 1, affects all drying dilute solutions. Solids are transported to the edge of a drying droplet, so that when all the solvent has evaporated, the remaining solid is thicker on the edges than in the center of the dried droplet [149]. The coffee ring effect is noticeable in the LIDART process, particularly for features approaching 10μm. An example can be seen in Figure 5.12. The coffee ring effect could potentially lessened if more concentrated, and therefore viscous ink were used [32].

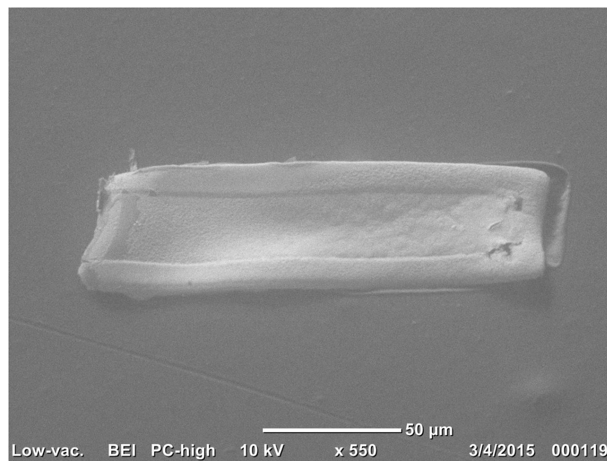

Figure 5.12: An SEM image of a transferred silver pattern onto COC. The edge of the pattern is thicker than the rest of the feature because of the coffee ring effect (see Figure 1.5 for more details.

Chapter 6

Conclusions and Future Work

This dissertation discussed improvements to dry-templated patterning of electronic components. This is the second dissertation written in on the subject of dry-templated patterning, and it marks the transition of the process from an experimental method for patterning lines, to a viable approach for creating electronic components. This chapter serves as a summary of the advances presented in this dissertation, and as a springboard from which to propose future improvements that can be made to this research.

6.1 Conclusions

This dissertation documents the transition of the AMPT process from a conceptual method of fabricating long, thin channels [64], to a process that can be used to create electronic devices. This transition included the refinement of master and template fabrication techniques (Chapter 2), the development of modeling tools to better optimise future designs (Chapter 3), the creation of SAW resonators as a demonstration for the viability of for AMPT-fabricated components (Chapter 4), and the exploration of alternative dry patterning techniques capable of improving throughput and feature design limitations (Chapter 5).

The major achievements of this work were:

- The AMPT process was expanded in terms of versatility with an emphasis on the ease of developing complex layouts
  - The process for fabricating AMPT templates was improved to create templates with uniform heights and smooth sidewalls. This enabled the simultaneous APMT patterning of shapes ranging from 30μm wide and 10μm tall, to features 350μm wide an 200μm tall.
  - A modeling approach was developed for AMPT to predict the likelihood of premature drying based on template geometry. This lets template designers evaluate templates for areas that pose a high risk of drying before creating a mask.

  – One-port surface acoustic resonators were designed and fabricated successfully using the AMPT process. Resonators with 1μm and 800nm IDTs performed well as resonators with quality factors at or above 10. 600nm and 500nm resonators were also fabricated with notable resonance peaks and quality factors below 10.

- A novel method of laser-transferring surface energy patterned nanoparticle layouts, called LIDART, was developed in order to improve the throughput and lessen patterning restrictions of AMPT. It has been demonstrated to print isolated conductive silver features with resolution of 10μm.

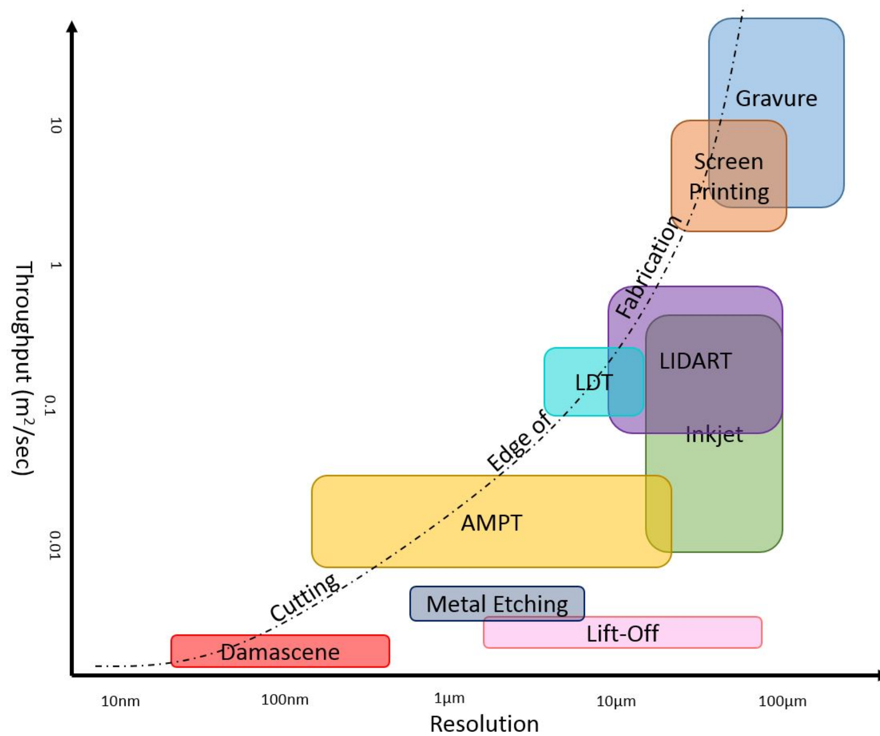

Figure 6.1: A comparison of fabrication methods for metal features. These techniques include the previous work discussed in Chapter 1, and the addition of LIDART and AMPT as discussed in this dissertation [150][151].

The two methods developed over the course of this dissertation, AMPT and LIDART, are both shown against the other fabrication methods from Chapter 1 in Figure 6.1. Figure 6.1 shows the resolution and approximate throughput of each patterning process. As seen in this plot, both AMPT and LIDART stand at the cutting edge of high-resolution, high-throughput printing.

Aspect ratio and feature layout limitations are presented in Figure 6.2. The aspect ratio of AMPT is the highest of available printing methods. The aspect ratio of LIDART is

comparable to other printing methods. Since AMPT is a microfluidic process, it is subject to significant feature limitations. All features must be connected to fill ports by way of channels, and wide features must have holes to prevent features from collapsing. This remains a disadvantage compared to gravure and screen. LIDART has relatively few limitations to feature layout, when compared to LDT, which is its direct competition in laser-tranfer patterning.

	AMPT	LIDART	Gravure	Screen Printing	LDT
Aspect Ratio	**1**	**~0.05** (Feature height defined by ink wetting and concentration)	**0.06-0.26** (Aspect ratio for wells, feature aspect ratio depends on resolution and ink concentration)	**0.05-0.08** (Feature thickness defined by screen thickness)	**0.03-0.04** (Defined by ribbon thickness)
Feature Limitations	Features must be connected to each other and to a fill channel. Wide features must include holes	The process must be improved to transfer sheets wider than the beam width without tearing	No restrictions. Feature shape is determined by well placement and fluidic properties	No restrictions	Feature layout is defined by the aperture. Features cannot be wider than the beam width

Figure 6.2: A comparison of the aspect ratio and layout limitations of the patterning methods from this dissertation (AMPT and LIDART) and commonly used printing techniques [46][48][152][153][154].

6.2 Future Work

This dissertation, in addition to that of Michael Demko, is intended to serve as a blueprint for future work on templated nanoprinting. As the process becomes increasingly refined, it is likely that this work will focus less on the details of master and template fabrication, and more on process optimization and new devices. As with any new fabrication technology, there are a plethora of potential applications for templated nanoprinting. The particular approach of future work in the field will no doubt be dictated by the interests of the researchers and available funding, resources and partnerships. This chapter will briefly cover several promising applications and research directions.

Smaller Features

The current state of two-layer masters currently show the ability to meet the needs of features as small as 400nm. As the size of features decreases, new techniques may need to be utilized to make masters with smooth sidewalls and uniform etch depths.

There remain several possible techniques to improve master fabrication. These techniques have the potential for high resolution, uniform sidewalls and unique geometric capabilities. One promising option is masked electrodeposition. This process uses photoresists or other masks to cover areas of a conductive substrate. The resist-patterned substrate is electroplated so that areas that are exposed are coated in metal and areas covered in photoresist remain untouched[155]. Electroplating is top-up, so resolution depends primarily on the lithography technique. The photoresist can be patterned through nanoimprint lithography, electron-beam lithography or ultraviolet lithography[156]. Electrodeposited sidewalls are smooth, and can be annealed to reach a smoother finish. Parylene bonds well to nickel and other metals, which can improve template delamination.

Improvements in laser machining[157] and 3D printing techniques such as two-photon lithography[158] present the possibility of truly three-dimensional AMPT masters.

6.3 Multi-Layer Patterning

SAW resonators were chosen as a demonstration device in this dissertation largely because they require only a single patterned layer of material. Though AMPT is capable of patterning more than one material at a time[64], these materials must be patterned in separate channels. Non-overlapping, single layer features significantly limit the design space for AMPT-manufactured devices. Most electrical components of interest, including batteries, transistors, diodes, inductors, and capacitors, require multiple overlapping layers. The simplest of these is to pattern a base layer using AMPT, before applying one or more additional layers with another technique.

The simplest approach to a multi-layer AMPT device is to pattern the bottom layer using AMPT, then to add additional conformal layers above. These layers can be added with solvent-casting (for thick uniform layers), vapor casting (for thin uniform layers), blade-casting on a surface-energy patterned substrate with an AMPT layer patterned on top (for patterned layers). Layers can also be added over AMPT features using a conformal patterned process like lithography or LIDART.

Printed Transistors, Batteries and Electronics

Multi-layer patterning on AMPT surfaces opens up a range of electronics that could not previously be patterned. A battery is perhaps the simplest example. High aspect ratio, interdigitated electrodes for the battery can be printed using the AMPT process. The electrodes may be patterned simultaneously from different nanoparticle materials, and sintered

into a high surface area mesh. An electrolyte may be solvent cast over the patterned material, creating a planar battery. A similar process, in which an electrolyte is replaced with a dielectric, may be used to fabricate a capacitor.

Transistors present a greater challenge, but given the need for flexible transistors, they are a necessary requirement for AMPT-fabricated digital electronic systems. The source and drain of a transistor may be easily printed by AMPT, but transistors require additional layers: at least two for a dielectric and semiconductor (both of which may be solvent- or vapor-cast) and a gate layer (which must be aligned to the source-drain layer). Since the dielectric and/or the semiconductor can be solvent-cast, they can be used to re-planarize the surface above the source-drain layer. The new planar surface would make it easier to print the final gate layer.

Roll-to-Roll Processing

In its current form, AMPT is performed on a die-by-die basis. A single AMPT template requires between 10 and 30 minutes to pattern properly. This process is too slow for an industrial application. Even if the patterning speed cannot be easily improved, throughput can be increased significantly by means of a roll-to-roll process in which a belt of templates is brought into contact with a substrate belt, and ink is added continuously. Converting AMPT to a roll-to-roll technique will require improvements in process control and template materials.

Modeling

Modeling of AMPT discussed in this work was qualitative rather than quantitative. It was designed to detect layouts that are at risk of patterning incorrectly by determining their rate of drying relative to the rate of drying for the rest of the template. By correlating models to experimental results, the models in this dissertation can be adapted to determine the absolute filling and drying time for AMPT templates.

Empirical determinations of filling time could be obtained by comparing high-resolution photographs and videos of the patterning process to a transient simulation of the drying time. Evaluating drying time would be the first step in creating a roll-to-roll AMPT process, in which ink must be fed to the individual features at the same rate as ink evaporation within the templates. The FEM work presented in this chapter, combined with more information about drying time could also be used to optimise template design for fast patterning. This would be a big benefit for a roll-to-roll AMPT setup. Improved patterning times translate to faster belt speeds and increased throughput.

The current modeling of AMPT could also be expanded to a greater range of solvents and template materials by incorporating more experimental data for the diffusion of solvents into permeable materials. The model should be easily extrapolated to any organic solvent and PDMS or TPX. The mechanism of transport modeling may have to be modified for

Teflon AF, because the solvent solubility does not play a major roll in transport through Teflon AF membranes.

High-Resolution LIDART

LIDART is currently limited to about 10μm, but this limit is not inherent to the process. Improvements to template fabrication and the inking of the propulsion layer could potentially push the resolution down to 1μm or below.

The biggest limitation to LIDART resolution now is the difficulty of fabricating high-resolution templates. Hot embossing creates uneven CYTOP topographies, and it is difficult to completely remove residual layers of CYTOP in order to expose hydrophilic glass wells. While lift-off has none of these disadvantages, it creates uneven interfaces between the CYTOP and glass. Better masters could likely be fabricated by plasma etching the CYTOP directly. Using metal masks protects the CYTOP from damage during the etching process[159].

There remains a great deal of potential improvement to the LIDART process that could be used to achieve greater reliability and smaller resolution of patterned features. Resolution depends heavily on the quality of the templates. Creating uniform high-quality templates was difficult with lift-off and hot embossing, so moving to metal-masked process for etching CYTOP would be a potential mechanism of improvement. A more polar and less viscous nitrocellulose solution might also solve some delamination issues.

Appendix A

A174 and Parylene Treatment

This procedure can be used to apply parylene over an A174 adhesion layer. The A174 is necessary for proper adhesion to silicon and silicon dioxide.

1. Dip wafer in piranha solution to remove any organic material
2. Optionally soak the wafer in 5:1 BHF solution in order to remove the residual oxide layer on the surface. BHF etch may also be calculated to remove a uniform thickness of oxide from all features as to preserve a uniform aspect ratio. The etch rate for thermally grown oxide features in 5:1 BHF is 400nm/min.
3. Combine 500mL of DI water, 500mL of isopropanol and 10mL of A174 silane into a well-cleaned beaker and allow to mix overnight.
4. Immerse the wafers in the solution for 30 minutes
5. Remove the wafers and allow them to dry upright for 30 minutes
6. Dry the wafers with a nitrogen gun and bake on a hot plate for 10 minutes at 120C.
7. Load the wafers into the parylene deposition system and run. A 100nm thick layer requires about 2.4g of dimer.

Parylene may also be annealed for increased strength. A typical annealing process consists of heating parylene to between 300°C and 350°C in a nitrogen environment, with ramp-up and ramp-down times of at least an hour[72].

Appendix B

PMP Synthesis

This procedure is taken from the dissertation of Michael Demko [64], with several modifications. The synthesis step includes additional toluene, which was added in order to able all of the PMP to gel without drying. The gel is then broken up when it is washed with ethanol to expose as much surface area as possible. This recipe also calls for purification by centrifuging. The centrifuge step removes particulate impurities and any remaining methanol. Both of these can interfere with the quality of small features.

1. Combine 0.264 g niobium pentachloride with 0.428 g triphenyl bismuth in 40 mL of toluene to form the catalyst solution.

2. Stir the catalyst solution at 90 C for 10 min.

3. Combine 2 g (2.8 mL) 4-methyl-2-pentyne in 2.8 mL of toluene to form the monomer solution.

4. Add the monomer solution dropwise to the catalyst solution, stirring constantly. The solution should gel quickly as the polymer is formed.

5. Hold the gelled polymer at 90 C for 1 hour to ensure completion of the reaction.

6. Separate the gelled polymer from any remaining liquid toluene. Wash the gelled polymer with methanol, while breaking the polymer into small pieces. Remove the polymer from the methanol, and dry the polymer under vacuum to remove all of the toluene from the gelled polymer.

7. Dissolve the polymer in 100 mL of cyclohexane. This dissolution will occur slowly, and can take in excess of 24 hours to dissolve completely. Periodic agitation will assist dissolution.

8. Precipitate the dissolved polymer in a large volume of methanol. This can be done by pipetting the dissolved polymer in 2 mL quantities into 400 mL of methanol, followed

by closing the container and violently agitating the mixture after each addition of polymer solution.

9. Filter the polymer to remove the precipitated polymer from the methanol. This can be done using a polypropylene filter with 25 m pores mounted in a vacuum filtration system.

10. Dry the removed polymer under vacuum to remove any remaining methanol, and re-dissolve in 100 mL of cyclohexane.

11. Repeat the previous three steps to re-precipitate and dissolve the polymer in cyclohexane, to ensure all of the catalyst is removed.

12. Dissolve the polymer in 100 mL of cyclohexane.

13. Centrifuge the solution at 4000rpm for 20 minutes. The clean PMP is the homogeneous solution on the top of the centrifuge tube.

14. Cast this component of the PMP onto a master.

Appendix C

Nitrocellulose

The following recipe can be used to create cellulose hexanitrate in methyl isobutyl ketone (MIBK) from loose cotton. The cellulose hexanitrate has a nitrogen content of 13.35% by mass, and is extremely explosive. The concentration of nitrogen can be lessened in order to ensure greater stability by increasing the proportion of nitric acid.

1. In an ice bath in the 250 mL beaker, carefully mix 70mL 18M sulfuric acid and 30mL 16M nitric acid.
2. Break 5 grams of cotton into small pieces.
3. Add cotton slowly to acid bath.
4. Wait one hour, replacing ice if necessary.
5. Decant acid out of the beaker, neutralizing any decanted liquid with baking soda.
6. Wash nitrocellulose with water, decanting out the remaining liquid and neutralizing it.
7. Repeat until no acid remains. If any acid is left, it can react strongly when it dries out.
8. Completely dry out nitrocellulose in a vacuum.
9. Dissolve nitrocellulose in MIBK. Take care to avoid any exposure to heat or flame, and dissolve the nitrocellulose as quickly as possible. Solutions will saturate above 5% by mass.

Appendix D

Flow Factor Software

This appendix contains the code to calculate the flow factor, as presented in Chapter 3. The prerequisite for this program is an exported table of flow velocity. The flow velocity can use a constant wall flux model as shown in Figure 3.11.

D.1 AMPT_Flow_Intro.m

```
% This file gives instructions for proper AMPT modeling
   techniques
% To begin using this file, first run a COMSOL fluid flow model
    that uses
% constant rate flux into the channel walls.  The channel must
   be oriented
% on the x-y plane, with the substrate on the plane z=0.
%
% All instructions are given for COMSOL5.0
%
% To export a file, right click on the "Export" tab in COMSOL,
   and click on
% the option that says "data".  Under the "Expressions" tab,
   select the
% 'x-coordinate', 'y-coordinate', 'z-coordinate', 'u', 'v', and
    'w'
% options.  The first three are in "Geometry>Coordinate", and
   the second
% three are in "Model>Component1>Creeping Flow>Velocity Field".
     Under the
% "Output" tab, select the filename, making sure to specify a .
   csv file.
```

```
% Evaluate in a regular grid in a spreadsheet format.  Select
   grids with
% equal intervals in all axes.  Finally, click on the "Advanced
   " tab and
% deselect the "Include Header" checkbox.  Finally, click on
   the "Export"
% button a the top of the panel.
%
% Import the file into matlab, specifying the vecotrs as 'x', '
   y', 'z',
% 'u', 'v', and 'w'.  Each of these vectors should be the same
   length.
% Then run this program, or run the programs individually.

vectors_to_matrix.m
% Takes COMSOL vectors and turns them into matrices with the
   data ploted in
% three-dimensional space

color_map.m
% Makes a color map that highlights areas that are likely to
   dry in red

compute_fill_factor.m
% Computes a fill factor that predicts the risk of drying based
    on fluid
% velocity and proximity to absorption into wall

plot_fill_factor.m
%Plots the fill factor
```

D.2 vectors_to_matrix.m

```
% vectors_to_matrix requires six vectors:
% x, y, and z are spatial vectors exported by COMSOL
% u, v, and w are the velocity field vectors exported by COMSOL
% Exports these values mapped onto a spacial matrix, u3, v3, w3
   , x3, y3,
% z3, and a the minimum, maximum, length, and interval for each
    vector

%Find all list maxima and the length of the vectors
```

```
xmin=min(x);
xmax=max(x);
ymin=min(y);
ymax=max(y);
zmin=min(z);
zmax=max(z);

xlength=find(x==xmax,1); %Find the length of the xvector

%Generate 2D arrays with x axis being x values and y axis being
    yz values
x2=zeros(xlength,(length(x)/xlength));
for i=1:(length(x)/xlength)
    x_seg=x((xlength*i-xlength+1):xlength*i);
    x2(:,i)=x_seg;
end

y2=zeros(xlength,(length(x)/xlength));
for i=1:(length(x)/xlength);
    y_seg=y((xlength*i-xlength+1):xlength*i);
    y2(:,i)=y_seg;
end

z2=zeros(xlength,(length(x)/xlength));
for i=1:(length(x)/xlength);
    z_seg=z((xlength*i-xlength+1):xlength*i);
    z2(:,i)=z_seg;
end

% Define matrices for which all NaN are replaced with 0, called
    u1,v1,w1
u1=u;
%u1(find(u1==0))=1;
u1(isnan(u1)) = 0 ;
v1=v;
%v1(find(v1==0))=1;
v1(isnan(v1)) = 0 ;
w1=u;
%w1(find(w1==0))=1;
w1(isnan(w1)) = 0 ;
```

```
%Generate 2D arrays with x axis being x values and y axis being
    yz values
u2=zeros(xlength,(length(x)/xlength));
for i=1:(length(x)/xlength);
    u_seg=u1((xlength*i-xlength+1):xlength*i);
    u2(:,i)=u_seg;
end

v2=zeros(xlength,(length(x)/xlength));
for i=1:(length(x)/xlength);
    v_seg=v1((xlength*i-xlength+1):xlength*i);
    v2(:,i)=v_seg;
end

w2=zeros(xlength,(length(x)/xlength));
for i=1:(length(x)/xlength);
    w_seg=w1((xlength*i-xlength+1):xlength*i);
    w2(:,i)=w_seg;
end

%Now it is time to construct 3D mapped matrices
%Find the y dimension length of the matrix
ylength=find(y2(1,:)==ymax,1);
%Find the z dimension length of the matrix
zlength=length(x)/(xlength*ylength);

%Generate 3D matrices
x3=zeros(xlength,ylength,zlength);
for i=1:zlength;
    x_seg=x2(:,(ylength*i-ylength+1):ylength*i);
    x3(:,:,i)=x_seg;
end

y3=zeros(xlength,ylength,zlength);
for i=1:zlength;
    y_seg=y2(:,(ylength*i-ylength+1):ylength*i);
    y3(:,:,i)=y_seg;
end

z3=zeros(xlength,ylength,zlength);
for i=1:zlength;
    z_seg=z2(:,(ylength*i-ylength+1):ylength*i);
```

```
    z3(:,:,i)=z_seg;
end

u3=zeros(xlength,ylength,zlength);
for i=1:zlength;
    u_seg=u2(:,(ylength*i-ylength+1):ylength*i);
    u3(:,:,i)=u_seg;
end

v3=zeros(xlength,ylength,zlength);
for i=1:zlength;
    v_seg=v2(:,(ylength*i-ylength+1):ylength*i);
    v3(:,:,i)=v_seg;
end

w3=zeros(xlength,ylength,zlength);
for i=1:zlength;
    w_seg=w2(:,(ylength*i-ylength+1):ylength*i);
    w3(:,:,i)=w_seg;
end

%Calculate magnitude of the velocity in three dimensional space
norm3=(u3.^2+v3.^2+w3.^2).^(1/2);

%Find intervals between the intervals in each direction
xint=x3(2,1,1)-x3(1,1,1);
yint=y3(1,2,1)-y3(1,1,1);
zint=z3(1,1,2)-z3(1,1,1);

%Construct a meshgrid for future plotting.
[X, Y, Z]=meshgrid(x(1):xint:xmax,y(1):yint:ymax,z(1):zint:zmax
   );
```

D.3 color_map.m

```
% This program generates a color map that colors the highest
   10% of drying
% risk as red, and with 10% apprearing white, and getting
   increasingly blue
% up to 100%.

maplength=1000; %The number of gradients in the map vector
```

```
map=zeros(maplength,3); %Generate a vector
frac=.1; %The fraction of values that appears red.

% Generate the red colors
for i=2:maplength*frac
    ent=i/(maplength.*frac);
    map(i,2:3)=ent;
    map(i,1)=1;
end

% Generate the blue colors
for i=maplength*frac:maplength
    ent=1-i/(maplength);
    map(i,1:2)=ent;
    map(i,3)=1;
end

colormap(map) %Enter this map vector as the color map
```

D.4 compute_fill_factor.m

```
% This program takes the flow vectors and the spatial vectors
   and computes
% a "flow factor" that can be used to calculate the risk of
   drying.  The
% flow factor takes into account both the velocity at a given
   location and
% the proximity drying walls.

% Find the integer value of the x, y, and z vector lengths.
xlength=floor(xlength);
ylength=floor(ylength);
zlength=floor(zlength);

% Find the magnitude of the flow at a given location
vel=sqrt(u3.^2+v3.^2+w3.^2);

% COMSOL has a tendency to calculate values that are
   erroniously high for
% certain locations, particularly around walls and corners.
   These can
```

```
% throw off flow-factor evaluations.  This section makes it so
   that no
% velocity is more than four times the average velocity.
   Anything over
% that value is averaged down.
vellin=vel(:); %Make all velocities one vector
velpop=vellin(find(vellin ~= 0)); %only find the populated
   values
velmax=4*mean(velpop); %Determine the maximum velocity
for i=1:xlength;
    for j=1:ylength;
        for k=1:zlength;
            if vel(i,j,k)>=velmax %if any value is larger than
               velmax
                vel(i,j,k)=velmax; %change it to velmax
            end
        end
    end
end

% Average all velocities across the z-axis.  This makes it
   easier to view
% flow factors from overhead.
vel_ave=mean(vel,3);

% This section creates a weighting matrix that is convolved
   with the flow
% absorption velocities into walls.  The matrix is the length '
   dmsize'
% in every dimension and decreases with the relationship 1/x (
   if expf=2
% and expf2=.5).
dmsize=8; % The size of the matrix
expf=2; %The factor that distances are multiplied by
expf2=.5; %The factor that the sums of the distances are
   divided by
distmatrix=zeros(dmsize*2+1, dmsize*2+1, dmsize*2+1); %Initiate
    matrix
for i=1:dmsize;
    for j=1:dmsize;
        for k=1:dmsize;
            distmatrix(dmsize+1-i,dmsize+1-j,dmsize+1-k)=...
```

```
    1/(i^expf+j^expf+k^expf)^expf2;
distmatrix(dmsize+1-i,dmsize+1-j,dmsize+1+k)=...
    1/(i^expf+j^expf+k^expf)^expf2;
distmatrix(dmsize+1-i,dmsize+1+j,dmsize+1-k)=...
    1/(i^expf+j^expf+k^expf)^expf2;
distmatrix(dmsize+1-i,dmsize+1+j,dmsize+1+k)=...
    1/(i^expf+j^expf+k^expf)^expf2;
distmatrix(dmsize+1+i,dmsize+1-j,dmsize+1-k)=...
    1/(i^expf+j^expf+k^expf)^expf2;
distmatrix(dmsize+1+i,dmsize+1-j,dmsize+1+k)=...
    1/(i^expf+j^expf+k^expf)^expf2;
distmatrix(dmsize+1+i,dmsize+1+j,dmsize+1-k)=...
    1/(i^expf+j^expf+k^expf)^expf2;
distmatrix(dmsize+1+i,dmsize+1+j,dmsize+1+k)=...
    1/(i^expf+j^expf+k^expf)^expf2;
distmatrix(dmsize+1,dmsize+1-j,dmsize+1-k)=1/(j^
   expf+k^expf)^expf2;
distmatrix(dmsize+1,dmsize+1-j,dmsize+1+k)=1/(j^
   expf+k^expf)^expf2;
distmatrix(dmsize+1,dmsize+1+j,dmsize+1-k)=1/(j^
   expf+k^expf)^expf2;
distmatrix(dmsize+1,dmsize+1+j,dmsize+1+k)=1/(j^
   expf+k^expf)^expf2;
distmatrix(dmsize+1-i,dmsize+1,dmsize+1-k)=1/(i^
   expf+k^expf)^expf2;
distmatrix(dmsize+1-i,dmsize+1,dmsize+1+k)=1/(i^
   expf+k^expf)^expf2;
distmatrix(dmsize+1+i,dmsize+1,dmsize+1-k)=1/(i^
   expf+k^expf)^expf2;
distmatrix(dmsize+1+i,dmsize+1,dmsize+1+k)=1/(i^
   expf+k^expf)^expf2;
distmatrix(dmsize+1-i,dmsize+1-j,dmsize+1)=1/(i^
   expf+j^expf)^expf2;
distmatrix(dmsize+1-i,dmsize+1+j,dmsize+1)=1/(i^
   expf+j^expf)^expf2;
distmatrix(dmsize+1+i,dmsize+1-j,dmsize+1)=1/(i^
   expf+j^expf)^expf2;
distmatrix(dmsize+1+i,dmsize+1+j,dmsize+1)=1/(i^
   expf+j^expf)^expf2;
distmatrix(dmsize+1-i,dmsize+1,dmsize+1)=(1/i^expf)
   ^expf2;
```

```
            distmatrix(dmsize+1+i,dmsize+1,dmsize+1)=(1/i^expf)
               ^expf2;
            distmatrix(dmsize+1,dmsize+1-j,dmsize+1)=(1/j^expf)
               ^expf2;
            distmatrix(dmsize+1,dmsize+1+j,dmsize+1)=(1/j^expf)
               ^expf2;
            distmatrix(dmsize+1,dmsize+1,dmsize+1-k)=(1/k^expf)
               ^expf2;
            distmatrix(dmsize+1,dmsize+1,dmsize+1+k)=(1/k^expf)
               ^expf2;

        end
    end
end


% This section finds the walls by determining the first and
   last values
% with a non-zero velocity.  It takes slices along a plane, and
    if it finds
% a wall, it adds a 1 to a spatial matrix of zeros.
% Each plane of walls is given a matrix, u3walls, v3walls, and
   w3walls.

%Find the walls in x direction
u3walls=zeros(xlength, ylength, zlength);
for i=1:ylength;
    for j=1:zlength; %Take samples alont the y-z plane
        if sum(u3(:,i,j))==0 %don't do anything if there are no
            values
        else %otherwise, find values along this segment
%Find the locations where u<=0 for this y and z value
      uflowloc=find(u3(:,i,j)~=0);
      %Find locations of first wall
      firstwall=uflowloc(1);
      %initialize list of the first wall locations in the
         channel
      %with the first element on the list of non-zero velocity
         elements
            for k=2:(length(uflowloc)); %now look after the
               first element
                if u3((uflowloc(k)-1),i,j)==0
```

```
                %check the element before the one in question.
                   Is it 0?
                %if uflowloc(k-1)+1==uflowloc(k)
                    firstwall=[firstwall uflowloc(k)];
                    %if so, add it to the list
                end
            end
            %Plot all first wall locations
            for k=1:length(firstwall)
                u3walls(firstwall(k),i,j)=1;
            end
      %Find last wall
      lastwall=uflowloc(end);
% initilize list of the last wall locations in a channel with
   the last
% vector on the list
            for k=(length(uflowloc)-1):-1:1;
                if u3((uflowloc(k)+1),i,j)==0
                    lastwall=[uflowloc(k) lastwall];
                end
            end
            %Plot all locations of the last wall
            for k=1:length(lastwall)
                u3walls(lastwall(k),i,j)=1;
            end
        end
    end
end

%Find the flow through the v walls
v3walls=zeros(xlength, ylength, zlength);
for i=1:xlength;
    for j=1:zlength;
        if sum(v3(i,:,j))==0
        else %calculate along this segment
      vflowloc=find(v3(i,:,j)~=0);
      %Find the locations where u<=0 for this y and z value
      %Find locations of first wall
      firstwall=vflowloc(1);
      %initialize list of the first wall locations in the
         channel
```

```
      %with the first element on the list of non-zero velocity
         elements
            for k=2:(length(vflowloc)); %now look after the
               first element
                if v3(i,(vflowloc(k)-1),j)==0
                    %check the element before the one in
                       question. Is it 0?
                    firstwall=[firstwall vflowloc(k)];
                    %if so, add it to the list
                end
            end

            %Plot all first wall locations
            for k=1:length(firstwall)
                v3walls(i,firstwall(k),j)=1;
            end
      %Find last wall
      lastwall=vflowloc(end);
%initilize list of the last wall locations in a channel with
   the last
% vector on the list
            for k=(length(vflowloc)-1):-1:1;
                if v3(i,(vflowloc(k)+1),j)==0
                    lastwall=[vflowloc(k) lastwall];
                end
            end
            %Plot all locations of the last wall
            for k=1:length(lastwall)
                v3walls(i,lastwall(k),j)=1;
            end

        end
    end
end




%Now we get the flux through the top of the mold (ignoring the
   bottom of
%the mold)
```

```
w3walls=zeros(xlength, ylength, zlength); %This is the 3d
   matrix
w3walls2d=zeros(xlength,ylength); %These are the 2d matrix
   slices
for i=1:xlength;
    for j=1:ylength;
        wflowloc=find(w3(i,j,:)~=0,1,'Last'); %Define top
           velocity element
        %This section just verifies that the walls turned out
           okay
        %if wflowloc>0
       if isempty(wflowloc)==0 %if there is a top velocity
          component
            w3walls2d(i,j)=wflowloc; % put it in the 2d matrix
        end
        w3walls(i,j,wflowloc)=1;
    end
end

% The velocities are determiend by multiplying the wall
   location matrices
% by the velocity matrices.  This gives the velocity at every
   wall.
u3walls_vel=u3walls.*abs(u3);
v3walls_vel=v3walls.*abs(v3);
w3walls_vel=w3walls.*abs(w3);

% The remainder of this program calculates the flowfactor score
   .
smallwall=zeros(i-dmsize:i+dmsize,j-dmsize:j+dmsize,k-dmsize:k+
   dmsize);
% This initializes a matrix of zeros that can be used to take a
    small
% subset the wall velocity matrix so that it can be calculated
   with the
% score wating matrix, "distmatrix".
wallsmat=u3walls_vel+v3walls_vel+w3walls_vel;
% This sums all of the wall velocity matrices, to give a wall
   velocity
% matrix that plots wall velocity in a 3D grid.
wallsmat_norm=wallsmat./(max(wallsmat(:)));
```

```
% This normalizes the wall velocity with respect to the maximum
    wall
% velocity
wallsmat_big=zeros(xlength+2*dmsize,ylength+2*dmsize,zlength+2*
   dmsize);
% Initializes a wall matrix that is buffered by enough zeros on
    all sides
% so that the wall matrix can be multiplied by the scoring
   matrix at any
% location wout an index problem.
wallsmat_big(dmsize+1:xlength+dmsize,dmsize+1:ylength+dmsize,
   dmsize...
    +1:zlength+dmsize)=wallsmat;
% Center the wall matrix the new wallsmat_big, so that it is
   buffered by
% zeros.
scoremat=zeros(xlength, ylength, zlength);
% Initialize a score matrix
% Now, for every value, in 3D space, if the velocity of any
   component is
% non-zero, multiply the scoring matrix centered around each
   point in space
% by the wall matrix that is buffered with zeros.
for i=1:xlength;
    for j=1:ylength;
        for k=1:zlength;
             if u3(i,j,k)~=0 || v3(i,j,k)~=0 || w3(i,j,k)~=0
                smallwall=wallsmat_big(i:i+2*dmsize,j:j+2*
                   dmsize,k:k+2*dmsize);
                % This is the subset of the wall matrix for
                   multiplication
                tempscore=distmatrix.*smallwall;
                % Multiply the distance scoring matrix by the
                   wall matrix
                locscore=sum(tempscore(:));
                % Sum up all of these values
                scoremat(i,j,k)=locscore;
                %Create a matrix of wall flux influence scure
             end
        end
    end
end
```

```
scoremat2d=mean(scoremat,3);
% Create a 2d matrix that averages the wall flux influence
   score in two
% dimensions
flowfactor=abs(vel_ave)./(1+(scoremat2d/(mean(scoremat2d(:)))))
   ;
% Find the flow factor by dividing the average velocity by 1 +
   the
% normalized flow velocity
```

D.5 plot_fill_factor.m

```
% Plots the flow factor as a surface plot on two dimensions.
   The flow
% factor predicts the risk of drying.

colormap(map) %Declare the map from 'colormap'
surf(flowfactor,'EdgeColor','None'); %Plot a surface plot of
   flow factor
view(2) %This lets you view the plot from overhead
axis equal %
```

Bibliography

[1] J.S. Kilby. *Miniaturized electronic circuits*. US Patent 3,138,743. 1964. URL: http://www.google.com/patents/US3138743.

[2] Yole Development. *Flexible Applications Based on Printed Electronics Technologies 2013*. Tech. rep. 2013.

[3] Donald Lupo et al. "OE-A Roadmap for Organic and Printed Electronics". In: *Applications of Organic and Printed Electronics, Integrated Circuits and Systems*. Ed. by E Cantatore. New York, NY: Springer, 2013. Chap. 1.

[4] James D. Plummer, Michael D. Deal, and Peter B. Griffin. *Silicon VLSI Technology: Fundamentals, Practice and Modeling*. Upper Saddle River, NJ: Prentince Hall, 2000.

[5] Wayne M. Moreau. *Semiconductor Lithography: Principles, Practices, and Materials*. New York, NY: Plenum Press, 1988.

[6] Andrew L. Goodyear et al. "High resolution inductively coupled plasma etching of 30 nm lines and spaces in tungsten and silicon". In: *Journal of Vacuum Science & Technology B: Microelectronics and Nanometer Structures* 18 (2000), p. 3471. ISSN: 0734211X. DOI: 10.1116/1.1326922.

[7] W.E. Bulst and E. Willibald. "Ultrareproducible SAW Resonator Production". In: *36th Annual Frequency Control Symposium 1982*. 1982, pp. 442–452.

[8] James L. Wilbur and George M. Whitesides. "Self-Assembly in Micro- and Nanofabrication". In: *Nanotechnology*. Ed. by Gregory L Timp. New York, NY: Springer-Verlag, 1998. Chap. 8.

[9] J W Morris. "Electromagnetic Properties". In: *A Survey of Materials Science*. Berkeley, CA, 2008. Chap. 3.

[10] John W Priest, Charles Smith, and Patrick Dubois. "Liquid Metal Jetting for Printing Metal Parts". In: *Proceedings of 8th Annual Solid Freeform Fabrication Symposium, Austin, TX.* (1997), pp. 1–9.

[11] Donald J Hayes, W R Cox, and David B Wallace. "Printing system for MEMS packaging". In: *Reliability, Testing, and Characterization of MEMS/MOEMS, October 22, 2001 - October 24* 4558 (2001), pp. 206–214. ISSN: 0277786X. DOI: 10.1117/12.443003. URL: http://dx.doi.org/10.1117/12.443003.

[12] K.F. Teng and R.W. Vest. "A microprocessor-controlled ink jet printing system for electronic circuits". In: *IEEE Transactions on Industrial Electronics* 35.3 (1988). ISSN: 0278-0046. DOI: 10.1109/41.3114.

[13] Gökhan Perçin, Thomas S. Lundgren, and Butrus T. Khuri-Yakub. "Controlled ink-jet printing and deposition of organic polymers and solid particles". In: *Applied Physics Letters* 73.1998 (1998), pp. 2375–2377. ISSN: 00036951. DOI: 10.1063/1.122465.

[14] Sawyer B. Fuller, Eric J. Wilhelm, and Joseph M. Jacobson. "Ink-jet printed nanoparticle microelectromechanical systems". In: *Journal of Microelectromechanical Systems* 11.1 (2002), pp. 54–60. ISSN: 10577157. DOI: 10.1109/84.982863.

[15] Ph. Buffat and J-P. Borel. "Size Effect on the Melting Temperature of Gold Particles". In: *Physical Review A.* 13.6 (1976).

[16] Hsien-Hsueh Lee, Kan-Sen Chou, and Kuo-Cheng Huang. "Inkjet printing of nanosized silver colloids." In: *Nanotechnology* 16 (2005), pp. 2436–2441. ISSN: 0957-4484. DOI: 10.1088/0957-4484/16/10/074.

[17] Fan Li and Jingzhe Pan. "Modeling "Nano-Effects" in Sintering". In: *Sintering*. Ed. by R.H.R Castro and K. van Benthem. Vol. 35. Berlin: Springer-Verlag, 2013. ISBN: 978-3-642-31008-9. DOI: 10.1007/978-3-642-31009-6. URL: http://link.springer.com/10.1007/978-3-642-31009-6.

[18] T Falat, B Platek, and J Felba. "Sintering process of silver nanoparticles in ink-jet printed conductive microstructures-Molecular dynamics approach". In: *EuroSimE 2012*. 2012, pp. 1–5. ISBN: 9781467315135. URL: http://ieeexplore.ieee.org/xpls/abs_all.jsp?arnumber=6191782.

[19] Joe Payer and Heesan Kim. "Tarnish process of Silver in Atmospheric Enviornments Containing Hydrogen Sulfide and Nitrogen Dioxide". In: *199th Meeting of the Electrochemical Society*. Washington DC, 2001.

[20] a De Rooij. "The Oxidation of Silver by Atomic Oxygen". In: *ESA Journal* 13 (1989), pp. 363–382. ISSN: 0379-2285.

[21] Vivek Subramanian et al. "Progress toward development of all-printed RFID tags: Materials, processes, and devices". In: *Proceedings of the IEEE* 93.7 (2005), pp. 1330–1338. ISSN: 00189219. DOI: 10.1109/JPROC.2005.850305.

[22] Markus Hösel and Frederik C. Krebs. "Large-scale roll-to-roll photonic sintering of flexo printed silver nanoparticle electrodes". In: *Journal of Materials Chemistry* 22 (2012), p. 15683. ISSN: 0959-9428. DOI: 10.1039/c2jm32977h.

[23] Hsien-Hsueh Lee, Kan-Sen Chou, and Kuo-Cheng Huang. "Inkjet printing of nanosized silver colloids." In: *Nanotechnology* 16 (2005), pp. 2436–2441. ISSN: 0957-4484. DOI: 10.1088/0957-4484/16/10/074.

[24] Lok R. Pokhrel, Brajesh Dubey, and Phillip R. Scheuerman. "Impacts of select organic ligands on the colloidal stability, dissolution dynamics, and toxicity of silver nanoparticles". In: *Environmental Science and Technology* 47 (2013), pp. 12877–12885. ISSN: 0013936X. DOI: 10.1021/es403462j.

[25] Kezia Cheng. "Copper Interconnect on GaAs pHEMT by Evaporation Process". 2009.

[26] Shlomo Magdassi, Michael Grouchko, and Alexander Kamyshny. "Copper Nanoparticles for Printed Electronics: Routes Towards Achieving Oxidation Stability". In: *Materials* 3.9 (Sept. 2010), pp. 4626–4638. ISSN: 1996-1944. DOI: 10.3390/ma3094626. URL: http://www.mdpi.com/1996-1944/3/9/4626/.

[27] Chil Seong Ah, Seung Do Hong, and Du-jeon Jang. "Preparation of Au Ag Nanorods and Characterization of Their Surface Plasmon Resonances Preparation of Au core Ag shell Nanorods and Characterization of Their Surface Plasmon". In: *The journal of Physical CHemistry B* 105.33 (2001), pp. 7871–7873. DOI: 10.1021/jp0113578.

[28] Michael Grouchko, Alexander Kamyshny, and Shlomo Magdassi. "Formation of air-stable copper-silver core-shell nanoparticles for inkjet printing". In: *Journal of Materials Chemistry* 19 (2009), p. 3057. ISSN: 0959-9428. DOI: 10.1039/b821327e.

[29] Sunho Jeong et al. "Controlling the thickness of the surface oxide layer on Cu nanoparticles for the fabrication of conductive structures by ink-jet printing". In: *Advanced Functional Materials* 18 (2008), pp. 679–686. ISSN: 1616301X. DOI: 10.1002/adfm.200700902.

[30] Youngil Lee et al. "Large-scale synthesis of copper nanoparticles by chemically controlled reduction for applications of inkjet-printed electronics." In: *Nanotechnology* 19 (2008), p. 415604. ISSN: 0957-4484. DOI: 10.1088/0957-4484/19/41/415604.

[31] Jennifer a. Lewis. "Direct ink writing of 3D functional materials". In: *Advanced Functional Materials* 16 (2006), pp. 2193–2204. ISSN: 1616301X. DOI: 10.1002/adfm.200600434.

[32] Madhusudan Singh et al. "Inkjet printing-process and its applications". In: *Advanced Materials* 22 (2010), pp. 673–685. ISSN: 09359648. DOI: 10.1002/adma.200901141.

[33] Zerodamage. *Rotogravure PrintUnit*.

[34] Ana Claudia Arias et al. "Materials and applications for large area electronics: solution-based approaches." In: *Chemical reviews* 110.1 (Jan. 2010), pp. 3–24. ISSN: 1520-6890. DOI: 10.1021/cr900150b. URL: http://www.ncbi.nlm.nih.gov/pubmed/20070114.

[35] Donovan Sung, Alejandro De La Fuente Vornbrock, and Vivek Subramanian. "Scaling and optimization of gravure-printed silver nanoparticle lines for printed electronics". In: *IEEE Transactions on Components and Packaging Technologies* 33.1 (2010), pp. 105–114. ISSN: 15213331. DOI: 10.1109/TCAPT.2009.2021464.

[36] Alejandro de la Fuente Vornbrock. "Roll Printed Electronics: Development and Scaling of Gravure Printing Techniques". PhD thesis. University of California, Berkeley, 2009.

[37] Katsuaki Suganuma. *Introduction to Printed Electronics*. New York, NY: Springer, 2014. ISBN: 9781461496243.

[38] Rungrot Kitsomboonloha et al. "Femtoliter-scale patterning by high-speed, highly scaled inverse gravure printing." In: *Langmuir : the ACS journal of surfaces and colloids* 28.48 (Dec. 2012), pp. 16711–23. ISSN: 1520-5827. DOI: `10.1021/la3037132`. URL: `http://www.ncbi.nlm.nih.gov/pubmed/23110647`.

[39] Frederik C. Krebs et al. "A complete process for production of flexible large area polymer solar cells entirely using screen printing-First public demonstration". In: *Solar Energy Materials and Solar Cells* 93 (2009), pp. 422–441. ISSN: 09270248. DOI: `10.1016/j.solmat.2008.12.001`.

[40] H. Kerp et al. "Advantages of High Aspect Ratio Screen-Printed Silver Lines Produced with Hot Melt Technology". In: *EU PVSEC*. Hamburg, 2009, pp. 21–25.

[41] Radoslav Parashkov et al. "Large area electronics using printing methods". In: *Proceedings of the IEEE* 93.7 (2005), pp. 1321–1329. ISSN: 00189219. DOI: `10.1109/JPROC.2005.850304`.

[42] Craig B. Arnold, Pere Serra, and Alberto Piqué. "Laser Direct-Write Techniques of Complex Materials". In: *MRS Buletin* 32 (2007), pp. 23–31.

[43] a Klini et al. "Laser induced forward transfer of metals by temporally shaped femtosecond laser pulses." In: *Optics express* 16.15 (July 2008), pp. 11300–9. ISSN: 1094-4087. URL: `http://www.ncbi.nlm.nih.gov/pubmed/18648449`.

[44] M. Baum et al. "Generation of transparent conductive electrodes by laser consolidation of LIFT printed ITO nanoparticle layers". In: *Applied Physics A* 111.3 (Feb. 2013), pp. 799–805. ISSN: 0947-8396. DOI: `10.1007/s00339-013-7646-y`. URL: `http://link.springer.com/10.1007/s00339-013-7646-y`.

[45] Matthias Nagel and Thomas Lippert. "Laser-Induced Forward Transfer for the Fabrication of Devices". In: *Nanomaterials: Processing and Characterization with Lasers*. Ed. by Subhash Chandra Singh et al. First. Weinheim, Germany: Wiley-VCH, 2012.

[46] Alberlto Piqué. "Digital Microfabrication by Laser Decal Transfer". In: *Journal of Laser Micro/Nanoengineering* 3.3 (Dec. 2008), pp. 163–169. ISSN: 18800688. DOI: `10.2961/jlmn.2008.03.0007`. URL: `http://www.jlps.gr.jp/jlmn/index.php?action=laser_volno\&volno=303`.

[47] Scott a. Mathews, Raymond C. Y. Auyeung, and Alberto Piqué. "Analysis and characterization of the laser decal transfer process". In: *Proc. SPIE* 8244 (Feb. 2012). Ed. by Friedrich G. Bachmann et al., 82440A. DOI: `10.1117/12.909264`. URL: `http://proceedings.spiedigitallibrary.org/proceeding.aspx?doi=10.1117/12.909264`.

[48] R. C. Y. Auyeung et al. "Laser decal transfer of freestanding microcantilevers and microbridges". In: *Applied Physics A* 97.3 (Oct. 2009), pp. 513–519. ISSN: 0947-8396. DOI: 10.1007/s00339-009-5433-6. URL: http://link.springer.com/10.1007/s00339-009-5433-6.

[49] A Piqué et al. "Laser-based Digital Microfabrication". In: *CLEO Pacific Rim*. Shanghai: IEEE, 2009, pp. 3–4. ISBN: 9781424438303.

[50] Jiwen Wang et al. "Three-dimensional printing of interconnects by laser direct-write of silver nanopastes." In: *Advanced materials (Deerfield Beach, Fla.)* 22.40 (Oct. 2010), pp. 4462–6. ISSN: 1521-4095. DOI: 10.1002/adma.201001729. URL: http://www.ncbi.nlm.nih.gov/pubmed/20818617.

[51] Alberto Piqué et al. "Laser transfer of reconfigurable patterns with a spatial light modulator". In: *SPIE Laser-based MIcro- and Nanopackaging and Assembly Vii*. Ed. by Udo Klotzbach, Yongfeng Lu, and Kunihiko Washio. Vol. 8608. SPIE, Mar. 2013, 86080K–9. DOI: 10.1117/12.2005345. URL: http://proceedings.spiedigitallibrary.org/proceeding.aspx?doi=10.1117/12.2005345.

[52] Alberto Piqué et al. "Laser Decal Transfer of Electronic Material with Thin Film Characteristics". In: *Proc. SPIE* 6879.687911 (Feb. 2008). Ed. by Andrew S. Holmes et al., pp. 687911–8. DOI: 10.1117/12.779672. URL: http://proceedings.spiedigitallibrary.org/proceeding.aspx?articleid=1327782.

[53] J. a. Barron et al. "Biological laser printing: A novel technique for creating heterogeneous 3-dimensional cell patterns". In: *Biomedical Microdevices* 6 (2004), pp. 139–147. ISSN: 13872176. DOI: 10.1023/B:BMMD.0000031751.67267.9f.

[54] a. Piqué et al. "A novel laser transfer process for direct writing of electronic and sensor materials". In: *Applied Physics A: Materials Science and Processing* 69 (1999), pp. 279–284. ISSN: 09478396. DOI: 10.1007/s003399900306.

[55] D. B. Chrisey et al. "Direct writing of conformal mesoscopic electronic devices by MAPLE DW". In: *Applied Surface Science* 168 (2000), pp. 345–352. ISSN: 01694332. DOI: 10.1016/S0169-4332(00)00824-2.

[56] a Piqué et al. "Laser processing of polymer thin films for chemical sensor applications". In: *Surface and Coatings Technology* 163-164 (2003), pp. 293–299. ISSN: 02578972. DOI: 10.1016/S0257-8972(02)00606-0.

[57] Seung H. Ko et al. "Nanomaterial enabled laser transfer for organic light emitting material direct writing". In: *Applied Physics Letters* 93.2008 (2008), pp. 91–94. ISSN: 00036951. DOI: 10.1063/1.3001803.

[58] Seung H. Ko et al. "High resolution selective multilayer laser processing by nanosecond laser ablation of metal nanoparticle films". In: *Journal of Applied Physics* 102.2007 (2007), pp. 1–9. ISSN: 00218979. DOI: 10.1063/1.2802302.

[59] Seung Hwan Ko and Costas P Grigoropoulos. “Unconventional , Laser Based OLED Material Direct Patterning and Transfer Method”. In: *Organic Light Emitting Diode - Material, Process and Devices*. Ed. by Seung Hwan Ko. InTech, 2009. Chap. 7, pp. 195–214. ISBN: 978-953-307-273-9. DOI: 10.5772/776.

[60] Seung Hwanmax Ko et al. “Nanoparticle selective laser processing for a flexible display fabrication”. In: *Japanese Journal of Applied Physics* 49 (2010), pp. 1–6. ISSN: 00214922.

[61] Jang Hyuk Kwon et al. “High-Performance Organic Light-Emitting Diode Displays”. In: *Applications of Organic and Printed Electronics, Integrated Circuits and Systems*. Ed. by Eugenio Cantatore. New York, NY: Springer-Verlag, 2013. Chap. 3, pp. 57–83. ISBN: 9781461431596.

[62] Et Al Hirano, T., Matsuo, K., Kohinata, K. *Novel laser transfer technology for manufacturing large-sized OLED displays*. Tech. rep. 2007, p. 1592.

[63] Et Al Lee, S.T., Suh, M.C., Kang, M.C. *LITI (laser induced thermal imaging) technology for high-resolution and large-sized AMOLED*. Tech. rep. 2007, p. 1588.

[64] Michael Thomas Demko. “High Resolution Additive Patterning of Nanoparticles and Polymers Enabled by Vapor Permeable Polymer Templates”. PhD thesis. 2012.

[65] Michael T. Demko et al. “High resolution patterning of nanoparticles by evaporative self-assembly enabled by in situ creation and mechanical lift-off of a polymer template”. In: *Applied Physics Letters* 99.2011 (2011), pp. 1–4. ISSN: 00036951. DOI: 10.1063/1.3671084.

[66] Microchem. *SU-8 2000 Permanent Epoxy Negative Photoresist*. Tech. rep. Newton, MA, 2000. DOI: 10.1146/annurev.matsci.28.1.153. URL: www.microchel.com.

[67] A del Campo and C Greiner. “SU-8: a photoresist for high-aspect-ratio and 3D submicron lithography”. In: *Journal of Micromechanics and Microengineering* 17.6 (June 2007), R81–R95. ISSN: 0960-1317. DOI: 10.1088/0960-1317/17/6/R01. URL: http://stacks.iop.org/0960-1317/17/i=6/a=R01?key=crossref.5f54d4397fa259758a20d0ac229f2a2c.

[68] Marvel Nanofabrication Laboratory. *Marvell Nanofabrication Laboratory Lab Manual*. Tech. rep. Berkeley, CA: University of California, 2015, p. 7.23.

[69] Christine P. Tan and Harold G. Craighead. “Surface engineering and patterning using parylene for biological applications”. In: *Materials* 3 (2010), pp. 1803–1832. ISSN: 19961944. DOI: 10.3390/ma3031803.

[70] Ray Huang and Y. C. Tai. “Parylene to silicon adhesion enhancement”. In: *15th International Conference on Solid-State Sensors, Actuators and Microsystems*. 2009, pp. 1027–1030. ISBN: 9781424441938. DOI: 10.1109/SENSOR.2009.5285963.

[71] Jay Han Chieh Chang, Bo Lu, and Yu Chong Tai. “Adhesion-enhancing surface treatments for parylene deposition”. In: *16th International Solid-State Sensors, Actuators and Microsystems Conference*. 2011, pp. 390–393. ISBN: 9781457701573. DOI: 10.1109/TRANSDUCERS.2011.5969484.

[72] Rene Patrick Von Metzen and Thomas Stieglitz. “The effects of annealing on mechanical, chemical, and physical properties and structural stability of Parylene C”. In: *Biomedical Microdevices* 15 (2013), pp. 727–735. ISSN: 13872176. DOI: 10.1007/s10544-013-9758-8.

[73] Jérôme Charmet et al. “Optimizing Parylene C adhesion for MEMS Processes: Potassium Hydroxide Wet Etching”. In: *Journal of Microelectromechanical Systems* 22.4 (2013), pp. 855–864. ISSN: 10577157. DOI: 10.1109/JMEMS.2013.2248126.

[74] M S Silverstein et al. “Plasma-Polymerized Fluoropolymer Thin FIilms For MIicroelectronic Applications”. In: *Metallization of Polymers*. 2002, pp. 61–71.

[75] S. Tajima and K. Komvopoulos. “Physicochemical properties and morphology of fluorocarbon films synthesized on crosslinked polyethylene by capacitively coupled octafluorocyclobutane plasma”. In: *Journal of Physical Chemistry C* 111 (2007), pp. 4358–4367. ISSN: 19327447. DOI: 10.1021/jp067521e.

[76] A.M. Polyakov, L.E. Starannikova, and Yu.P. Yampolskii. “Amorphous Teflons AF as organophilic pervaporation materials Transport of individual components”. In: *Journal of Membrane Science* 216 (2003), pp. 241–256. ISSN: 03767388. DOI: 10.1016/S0376-7388(03)00077-2. URL: http://linkinghub.elsevier.com/retrieve/pii/S0376738803000772.

[77] A. Morisato and I. Pinnau. “Synthesis and gas permeation properties of”. In: *Journal of Membrane Science* 121 (1996), pp. 243–250.

[78] I. Blume et al. “Vapour sorption and permeation properties of poly (dimethylsiloxane) films”. In: *Journal of Membrane Science* 61 (1991), pp. 85–97. ISSN: 03767388. DOI: 10.1016/0376-7388(91)80008-T.

[79] Mitsui Chemicals America. *Polymethyl Pentene (PMP) TPX*. Tech. rep. Tokyo: Mitsu Chemicals Inc., 2011.

[80] Elena Martínez and Josep Samitier. “Soft Lithography and Variants”. In: *Generating Micro- and Nanopattersn on Polymeric Materials*. Ed. by Arazazu del Campo and Eduard Arzt. Weinheim, Germany: Wiley-VCH, 2011, pp. 57–68. ISBN: 9783527325085.

[81] Cheng-Sheng Huang, Edwin Yue-Bun Pun, and Wei-Chih Wang. “Fabrication of an elastomeric rib waveguide Bragg grating filter”. In: *Journal of the Optical Society of America B* 26.6 (May 2009), p. 1256. ISSN: 0740-3224. DOI: 10.1364/JOSAB.26.001256. URL: http://www.opticsinfobase.org/abstract.cfm?URI=josab-26-6-1256.

[82] Michael T Demko, Jim C Cheng, and Albert P Pisano. "Rigid , Vapor-Permeable for High Resolution Patterning of Nanoparticles and Polymers". In: *ACS Nano* Xx (2012).

[83] Dahl Young Khang and Hong H. Lee. "Sub-100 nm Patterning with an Amorphous Fluoropolymer Mold". In: *Langmuir* 20.10 (2004), pp. 2445–2448. ISSN: 07437463. DOI: 10.1021/la0358668.

[84] DuPont. *DuPont Teflon AF*. Tech. rep. 2013. URL: http://www2.dupont.com/Teflon_Industrial/en_US/assets/downloads/DuPont_Teflon_AF_Product_Info_K26985_H44587.pdf.

[85] Hong Zhang, Sijia Wang, and Stephen G. Weber. "Nanocomposite Teflon AF 2400 films as tunable platforms for selective transport". In: *Analytical Chemistry* 84 (2012), pp. 9920–9927. ISSN: 00032700. DOI: 10.1021/ac3022289.

[86] Michael T Demko, Timothy P Brackbill, and Albert P Pisano. "Simultaneous patterning of nanoparticles and polymers using an evaporation driven flow in a vapor permeable template." In: *ACS journal of surfaces and colloids* 28.25 (June 2012), pp. 9857–63. ISSN: 1520-5827. DOI: 10.1021/la301587f. URL: http://www.ncbi.nlm.nih.gov/pubmed/22647075.

[87] K. L. Dorsey et al. "Functionalized Micromolded Nanoparticles Towards Gas Sensor Arrays". In: *IEEE Sensors*. Valencia, 2014.

[88] Brian J. Kirby. *Micro- and Nanoscale Fluid Mechanics*. 2010. ISBN: 9780521119030.

[89] R. Byron Bird, Warren E. Stewart, and Edwin N. Lightfoot. *Transport Phenomena*. 2nd. New York, NY: Wiley, 2007.

[90] F. A. L. Dullien. *Porous Media: Fluid Transport and Pore Sturcture*. 2nd. San Diego: Academic Press, 1992. ISBN: 0122236513.

[91] W. L. Haberman and R. M. Sayre. *Motion of rigid and fluid spheres in stationary and moving liquids inside cylindrical tubes.* Tech. rep. 1958.

[92] V. Ilic et al. "Translation and Rotation of Spheres Settling in Square and Circular Conduits: Experiments and Numerical Predictions". In: *Int. J. Multiphase Flow* 18.6 (2006), pp. 1061–1075.

[93] R. G M van der Sman. "Drag force on spheres confined on the center line of rectangular microchannels". In: *Journal of Colloid and Interface Science* 351.1 (2010), pp. 43–49. ISSN: 00219797. DOI: 10.1016/j.jcis.2010.06.057. URL: http://dx.doi.org/10.1016/j.jcis.2010.06.057.

[94] Richard Skalak. "Viscous flow in a cylindrical tube containing a line of spherical particles". In: *J. Fluid Mech* 38.1 (1969), pp. 75–96.

[95] Dean Mo Liu. "Particle packing and rheological property of highly-concentrated ceramic suspensions: Phim determination and viscosity prediction". In: *Journal of Materials Science* 35 (2000), pp. 5503–5507. ISSN: 00222461. DOI: 10.1023/A:1004885432221.

[96] V Ya. Rudyak, S V Dimov, and V V Kuznetsov. "On the dependence of the viscosity coefficient of nanofluids on particle size and temperature". In: *Technical Physics Letters* 39.9 (2013), pp. 779–782. ISSN: 1063-7850, 1090-6533. DOI: 10.1134/S1063785013090125. URL: http://link.springer.com/10.1134/S1063785013090125$\backslash$nfiles/3645/art\%3A10.1134\%2FS1063785013090125.pdf.

[97] Valery Ya Rudyak. "Viscosity of Nanofluids Why It Is Not Described by the Classical Theories". In: *Advances in Nanoparticles* 2.August (2013), pp. 266–279. ISSN: 2169-0510. DOI: 10.4236/anp.2013.23037.

[98] DDBST GMBH. *Liquid Dynamic Viscosity, Calculated by Vogel Equation*. 2015. URL: http://ddbonline.ddbst.de/VogelCalculation/VogelCalculationCGI.exe (visited on 02/22/2015).

[99] Younan Xia and George M. Whitesides. "Soft Lithography". In: *Angewandte Chemie International Edition* 37.5 (Mar. 1998), pp. 550–575. ISSN: 14337851. DOI: 10.1002/(SICI)1521-3773(19980316)37:5<550::AID-ANIE550>3.3.CO;2-7. URL: http://doi.wiley.com/10.1002/\%28SICI\%291521-3773\%2819980316\%2937\%3A5\%3C550\%3A\%3AAID-ANIE550\%3E3.3.CO\%3B2-7.

[100] Byron D Gates et al. "New approaches to nanofabrication: molding, printing, and other techniques." In: *Chemical reviews* 105.4 (Apr. 2005), pp. 1171–96. ISSN: 0009-2665. DOI: 10.1021/cr030076o. URL: http://www.ncbi.nlm.nih.gov/pubmed/15826012.

[101] G. K. Batchelor. *An Introduction to Fluid Dynamics*. Cambridge: Cambridge University Press, 1967.

[102] Soney C George and Sabu Thomas. "Transport phenomena through polymeric systems". In: *Progress in Polymer Science* 26 (2001), pp. 985–1017. ISSN: 00796700. DOI: 10.1016/S0079-6700(00)00036-8.

[103] J. G. Wijmans and R. W. Baker. "The solution-diffusion model: A review". In: *Journal of Membrane Science* 107 (1995), pp. 1–21. ISSN: 03767388. DOI: 10.1016/0376-7388(95)00102-I.

[104] Bd Freeman and Aj Hill. "Free volume and transport properties of barrier and membrane polymers". In: *ACS Symposium Series* 710 (1998), pp. 306–325. ISSN: 00976156. DOI: 10.1021/bk-1998-0710. URL: http://pubs.acs.org/doi/book/10.1021/bk-1998-0710$\backslash$nhttp://pubs.acs.org/doi/abs/10.1021/bk-1998-0710.ch021.

[105] Peter M. Budd and Neil B. McKeown. "Highly permeable polymers for gas separation membranes". In: *Polymer Chemistry* 1.1 (2010), p. 63. ISSN: 1759-9954. DOI: 10.1039/b9py00319c. URL: http://xlink.rsc.org/?DOI=b9py00319c.

[106] Bruce Duncan, Jeannie Urquhart, and Simon Roberts. *Review of measurement and modelling of permeation and diffusion in polymers*. Tech. rep. January. Middlesex, UK: National Physics Laboratory, 2005, p. 73. URL: http://resource.npl.co.uk/materials/polyproc/iag/october2005/depc_mpr_012.pdf.

[107] Eric Charles Suloff. "Sorption Behavior of an Aliphatic Series of Aldehydes in the Presence of Poly(ethylene terephthalate) Blends Containing Aldehyde Scavenging Agents". PhD thesis. 2002, pp. 29–99.

[108] Kazukiyo Nagai et al. "Effects of Physical Aging on Solubility , Diffusivity , and Permeability of Propane and n -Butane in Poly (4-methyl-2-pentyne)". In: *Journal of Polymer Science B* 24 (2004), pp. 2407–2418. DOI: 10.1002/polb.20116.

[109] A Morisato, Z He, and I Pinnau. "Mixed-Gas Permeation Properties and Physical Aging of Poly(4-methyl-2-pentyne)". In: *Polymer Membranes for Gas and Vapor Separation*. Vol. 733. 1999, pp. 56–67. ISBN: 0-8412-3605-4. DOI: doi : 10 . 1021 / bk - 1999 - 0733 . ch004 $ \backslash $ r10 . 1021 / bk - 1999 - 0733 . ch004. URL: http://dx.doi.org/10.1021/bk-1999-0733.ch004.

[110] J. Winkelmann. "Gases in Gases, Liquids and their Mixtures". In: *Landolt-Bornstein - Group IV Physical Chemistry*. Ed. by E. Lechner. 15A. Berlin: Springer, 2007, p. 912.

[111] Brian J. Kirby. *Micro- and Nanoscale Fluid Mechanics*. 2010. ISBN: 9780521119030.

[112] R. Byron Bird, Warren E. Stewart, and Edwin N. Lightfoot. *Transport Phenomena*. 2nd ed. New York, NY: John Wiley & Sons, 2007. ISBN: 9780470115398.

[113] COMSOL. *Variably Saturated Flow and Transport: Sorbing Solute*. Tech. rep. Comsol Multiphysics, 2008.

[114] COMSOL. *Separation Through Dialysis*. Tech. rep. 2012, pp. 1–18.

[115] Y Takagaki et al. "Fabrication of GHz-range surface-acoustic-wave transducers on LiNbO 3 using imprint lithography". In: *Nanotechnology* 13.1 (2002), pp. 15–17. ISSN: 0957-4484. DOI: 10.1088/0957-4484/13/1/303. URL: http://stacks.iop.org/0957-4484/13/i=1/a=303?key=crossref.1de4ce871993b49a072dd8f3140f72bb.

[116] Jr. Bell D.L.T. and R.C.M. Li. "Surface-acoustic-wave resonators". In: *Proceedings of the IEEE* 64.5 (1976). ISSN: 0018-9219. DOI: 10.1109/PROC.1976.10200.

[117] Ville Kaajakar and VTI Technologies. "Theory and Analysis of MEMS resonators". In: *IEEE International Frequency Control Symposium*. 2011, pp. 1–20.

[118] Rs Weis and Tk Gaylord. “Lithium Niobate: Summary of Physical Properties and Crystal Structure R.” In: *Applied Physics A: Materials Science & Processing* 37 (1985), pp. 191–203. ISSN: 07217250. DOI: 10.1007/BF00614817. URL: http://dx.doi.org/10.1007/BF00614817$\backslash$nhttp://link.springer.com/article/10.1007/BF00614817.

[119] Takeshi Honda et al. “Controllable polymerization of N-carboxy anhydrides in a microreaction system.” In: *Lab on a chip* 5 (2005), pp. 812–818. ISSN: 1473-0197. DOI: 10.1039/b505137a.

[120] Stéphanie Périchon Lacour et al. “Stretchable gold conductors on elastomeric substrates”. In: *Applied Physics Letters* 82.15 (2003), pp. 2404–2406. ISSN: 00036951. DOI: 10.1063/1.1565683.

[121] Sul Lee et al. “Solution-processed ZnO nanoparticle-based semiconductor oxide thin-film transistors”. In: *Superlattices and Microstructures* 44.6 (2008), pp. 761–769. ISSN: 07496036. DOI: 10.1016/j.spmi.2008.09.002. URL: http://dx.doi.org/10.1016/j.spmi.2008.09.002.

[122] R. J. Bandaranayake et al. “Structural phase behavior in II-VI semiconductor nanoparticles”. In: *Applied Physics Letters* 67.1995 (1995), p. 831. ISSN: 00036951. DOI: 10.1063/1.115458.

[123] Wan Sik Hwang et al. “Comparative study of chemically synthesized and exfoliated multilayer MoS2 field-effect transistors”. In: *Applied Physics Letters* 102.4 (2013), pp. 2013–2016. ISSN: 00036951. DOI: 10.1063/1.4789975.

[124] Won Seok Yun et al. “Thickness and strain effects on electronic structures of transition metal dichalcogenides: 2H-MX_{2} semiconductors (M = Mo, W; X = S, Se, Te)”. In: *Physical Review B* 85.3 (2012), pp. 1–5. ISSN: 1098-0121. DOI: 10.1103/PhysRevB.85.033305.

[125] M. Härting et al. “Fully printed silicon field effect transistors”. In: *Applied Physics Letters* 94.19 (2009), pp. 20–23. ISSN: 00036951. DOI: 10.1063/1.3126958.

[126] E. Drahi et al. “Impact of ink synthesis on processing of inkjet-printed silicon nanoparticle thin films: A comparison of Rapid Thermal Annealing and photonic sintering”. In: *Thin Solid Films* 574 (2015), pp. 169–176. ISSN: 00406090. DOI: 10.1016/j.tsf.2014.11.079. URL: http://linkinghub.elsevier.com/retrieve/pii/S0040609014012437.

[127] Minh Trung Dang, Lionel Hirsch, and Guillaume Wantz. “P3HT:PCBM, best seller in polymer photovoltaic research”. In: *Advanced Materials* 23.31 (2011), pp. 3597–3602. ISSN: 09359648. DOI: 10.1002/adma.201100792.

[128] John E. Northrup. “Atomic and electronic structure of polymer organic semiconductors: P3HT, PQT, and PBTTT”. In: *Physical Review B - Condensed Matter and Materials Physics* 76.24 (2007), pp. 1–6. ISSN: 10980121. DOI: 10.1103/PhysRevB.76.245202.

[129] Jean Roncali. "Synthetic Principles for Bandgap Control in Linear π-Conjugated Systems". In: *Chemical Reviews* 97.1 (1997), pp. 173–206. ISSN: 0275-1879. DOI: 10.1111/j.1754-4505.2009.00107.x. URL: http://pubs.acs.org/doi/abs/10.1021/cr950257t.

[130] Charles Kittel. *Introduction to Solid State Physics*. Ed. by Stewart Johnson. 8th. Danvers, MA: Wiley, 2005. ISBN: 047141526X.

[131] F. Maier et al. "Origin of surface conductivity in diamond". In: *Physical Review Letters* 85 (2000), pp. 3472–3475. ISSN: 00319007. DOI: 10.1103/PhysRevLett.85.3472.

[132] Omar El Tall et al. "Direct functionalization of nanodiamonds with maleimide". In: *Chemistry of Materials* 26.9 (2014), pp. 2766–2769. ISSN: 15205002. DOI: 10.1021/cm500036x.

[133] Diversified Enterprises. *Critical Surface Tension and Contact Angle with Water for Various Polymers*. 2009. URL: http://www.accudynetest.com/polytable (visited on 03/12/2015).

[134] a Carre. "Polar interactions at liquid/polymer interfaces". In: *Journal of Adhesion Science and Technology* 21.10 (2007), pp. 961–981. ISSN: 0169-4243. DOI: Doi10.1163/156856107781393875. URL: <GotoISI>://WOS:000248819600005$\backslash$nhttp://www.tandfonline.com/doi/pdf/10.1163/156856107781393875.

[135] Edward Bormashenko. "Wetting transitions on biomimetic surfaces." In: *Phil. Trans. R. Soc. A* 368.1929 (Oct. 2010), pp. 4695–711. ISSN: 1364-503X. DOI: 10.1098/rsta.2010.0121. URL: http://www.ncbi.nlm.nih.gov/pubmed/20855316.

[136] Paul Roach, Neil J Shirtcliffe, and Michael I Newton. "Progess in superhydrophobic surface development". In: *Soft Matter* 4 (2008), pp. 224–240. DOI: 10.1039/B712575P.

[137] P J Allen et al. *FY 2008 Infrared Photonics Final Report*. Tech. rep. Richland, Washington, USA: U.S. Department of Energy, 2008.

[138] Y. S. Jeong et al. "UV-visible and infrared characterization of poly(p-xylylene) films for waveguide applications and OLED encapsulation". In: *Synthetic Metals* 127 (2002), pp. 189–193. ISSN: 03796779. DOI: 10.1016/S0379-6779(01)00621-X.

[139] Asahi Glass Corporation. *CYTOP Amorphous Fluoropolymer*. Tech. rep. Tokyo: ACG Chemicals, 2009.

[140] Taizo Kobayashi et al. "Formation of superhydrophobic/superhydrophilic patterns by combination of nanostructure-imprinted perfluoropolymer and nanostructured silicon oxide for biological droplet generation". In: *Applied Physics Letters* 98.12 (2011), p. 123706. ISSN: 00036951. DOI: 10.1063/1.3570627. URL: http://link.aip.org/link/APPLAB/v98/i12/p123706/s1\&Agg=doi.

[141] Sang H. Lee et al. "Micro protein patterning using a lift-off process with fluorocarbon thin film". In: *Sensors and Actuators, B: Chemical* 99 (2004), pp. 623–632. ISSN: 09254005. DOI: 10.1016/j.snb.2003.11.040.

[142] Ville Jokinen et al. "Durable superhydrophobicity in embossed CYTOP fluoropolymer micro and nanostructures". In: *Colloids and Surfaces A: Physicochemical and Engineering Aspects* 434 (2013), pp. 207–212. ISSN: 09277757. DOI: 10.1016/j.colsurfa.2013.05.061.

[143] P Suvanto, V Jokinen, and S Franssila. "Superhydrophobic Perfluoropolymer Micro- and Nanostructures by Embossing". In: *15th International Conferece on Miniaturized Systems for Chestrand Life Sciences*. 2011, pp. 464–466. ISBN: 9780979806445.

[144] Chang S. Lee et al. "Protein patterning on silicon-based surface using background hydrophobic thin film". In: *Biosensors and Bioelectronics* 18.2 (2003), pp. 437–444. ISSN: 09565663. DOI: 10.1016/S0956-5663(02)00147-1.

[145] Christian Reichardt. *Solvents and Solvent Effects in Organic Chemistry*. 3rd. Wiley-VCH, 2003.

[146] Steve Norman and Andrew Appleyard. "Fiber Lasers Conquer the Industrial Mainstream Market". In: *Laser Teknik Journal* 3.May (2009), pp. 45–50.

[147] Andy Appleyard. *New Horizons in process capability*. Tech. rep. SPI Lasers, 2008, pp. 1–5.

[148] Costas P. Grigoropoulos. *Transport in Laser Microfabrication*. Cambridge: Cambridge University Press, 2009.

[149] Sun Choi. "Evaporation-Driven Fast Crystalization of 3D Micro- and Nano-particle Assemblies via Micro Mechanical Systems". PhD thesis. UC Berkeley, 2012.

[150] Jurgens Daniel and PARC. "Printed Electronics: Technologies, Challenges and Applications". In: *International Workshop on Flexible and Printed Electronics*. Muju Resort, Korea, 2010.

[151] Julian W. Gardner, Vijay K. Varadan, and Osama O. Awadelkarim. *Microsensors, MEMS, and Smart Devices*. 1st. West Sussex, UK: Wiley, 2001. ISBN: 047186109X.

[152] Jinsoo Noh et al. "Scalability of roll-to-roll gravure-printed electrodes on plastic foils". In: *IEEE Transactions on Electronics Packaging Manufacturing* 33.4 (2010), pp. 275–283. ISSN: 1521334X. DOI: 10.1109/TEPM.2010.2057512.

[153] Vivek Subramanian and Donovan Sung. *Gravure as an industrially viable process for printed electronics*. Tech. rep. Berkeley, CA: University of California, 2008, p. 50. URL: http://scholar.google.com/scholar?hl=en\&btnG=Search\&q=intitle:Gravure+as+an+Industrially+Viable+Process+for+Printed+Electronics\#0$\backslash$nhttp://scholar.google.com/scholar?hl=en\&btnG=Search\&q=intitle:Gravure+as+an+industrially+viable+process+for+printed+

electronics\#0$\backslash$nhttp://www.eecs.berkeley.edu/Pubs/TechRpts/2008/EECS-2008-70.html.

[154] Dean Buzby and Art Dobie. "Fine Line Screen Printing of Thick Film Pastes on Silicon Solar Cells". In: *International Microelectronics Assembly and Packaging Society*. 610. Providence, RI, 2008. ISBN: 0930815866.

[155] Babak Ziaie, Antonio Baldi, and Massood Z. Atashbar. "Introduction to Micro-/Nanofabrication". In: *Springer Handbook of Nanotechnology*. Ed. by Bharat Bhushan. Vol. A. Berlin: Springer Berlin Heidelberg, 2012. Chap. 8, pp. 191–238. DOI: 10.1016/j.lfs.2012.10.005. URL: http://www.ncbi.nlm.nih.gov/pubmed/23162715.

[156] L.J. Heyderman et al. "Nanofabrication using hot embossing lithography and electroforming". In: *Microelectronic Engineering* 57-58.2001 (2001), pp. 375–380. ISSN: 01679317. DOI: 10.1016/S0167-9317(01)00436-1.

[157] Raymond M. Karam and Richard J. Casler. *A new 3D, direct-write, sub-micron microfabrication process that achieves true optical, mechatronic and packaging integration on glass-ceramic substrates*. Tech. rep. Santa Barbara, CA: Invenios, 2003. URL: http://invenios.com/micro-fabrication-resources/micro-fabrication-articles/.

[158] Tommaso Baldacchini. "Part Three Laser Scanning Three-Dimensional Microfabrication by Two-Photon Polymerization". In: *Generating Micro- and Nanopatterns on Polymeric Materials*. Ed. by A del Campo and E Arzt. Weinheim, Germany: Wiley-VCH Verlag, 2011. Chap. 7, pp. 108–140. ISBN: 9783527325085.

[159] Taizo Kobayashi et al. "Novel combination of hydrophilic/hydrophobic surface for large wettability difference and its application to liquid manipulation." In: *Lab on a chip* 11.4 (Feb. 2011), pp. 639–44. ISSN: 1473-0189. DOI: 10.1039/c0lc00394h. URL: http://www.ncbi.nlm.nih.gov/pubmed/21127789.